



HAL
open science

Neogene basin infilling from cosmogenic nuclides (^{10}Be and ^{21}Ne) in Atacama, Chile: implications for paleoclimate and copper supergene enrichment

Caroline Sanchez, Vincent Regard, Sebastien Carretier, Rodrigo Riquelme Salazar, P. Blard, Eduardo Campos, Stéphanie Brichaud, Maarten Lupker, Gerard Herail

► To cite this version:

Caroline Sanchez, Vincent Regard, Sebastien Carretier, Rodrigo Riquelme Salazar, P. Blard, et al.. Neogene basin infilling from cosmogenic nuclides (^{10}Be and ^{21}Ne) in Atacama, Chile: implications for paleoclimate and copper supergene enrichment. *Basin Research*, 2021, 33 (5), pp.2549-2571. 10.1111/bre.12568 . hal-03438822

HAL Id: hal-03438822

<https://hal.science/hal-03438822>

Submitted on 21 Nov 2021

HAL is a multi-disciplinary open access archive for the deposit and dissemination of scientific research documents, whether they are published or not. The documents may come from teaching and research institutions in France or abroad, or from public or private research centers.

L'archive ouverte pluridisciplinaire **HAL**, est destinée au dépôt et à la diffusion de documents scientifiques de niveau recherche, publiés ou non, émanant des établissements d'enseignement et de recherche français ou étrangers, des laboratoires publics ou privés.



Distributed under a Creative Commons Attribution 4.0 International License



Neogene basin infilling from cosmogenic nuclides (^{10}Be and ^{21}Ne) in Atacama, Chile: implications for paleoclimate and copper supergene enrichment.

Journal:	<i>Basin Research</i>
Manuscript ID	Draft
Manuscript Type:	Original Article
Date Submitted by the Author:	n/a
Complete List of Authors:	Sanchez, Caroline; GET, Université de Toulouse, CNRS, IRD, UPS Regard, Vincent; GET, Université de Toulouse, CNRS, IRD, UPS Carretier, Sébastien; GET, Université de Toulouse, CNRS, IRD, UPS Riquelme Salazar, Rodrigo; Universidad Catolica del Norte, Departamento de Ciencias Geológicas Blard, Pierre-Henri; Centre de Recherches Pétrographiques et Géochimiques Campos, Eduardo; Universidad Catolica del Norte, Departamento de Ciencias Geológicas Brichau, Stéphanie; GET, Université de Toulouse, CNRS, IRD, UPS Lupker, Maarten; ETH Zürich, Geological Institute Hérail, Gérard; GET, Université de Toulouse, CNRS, IRD, UPS
Keywords:	supergene copper deposits, Economic Geology, cosmogenic nuclides, Atacama, denudation rates, intramountainous basin, sediment flux, burial dating

SCHOLARONE™
Manuscripts

- the $^{10}\text{Be}/^{21}\text{Ne}$ pair of comogenic nuclides is useful to date Miocene sediments and exotic supergene enrichment
- Erosion rates higher to 250 m/Myr have been recorded during Middle Miocene in Atacama
- Progressive decrease of erosion rates at around 10 Myr ago in Atacama
- We date an exotic copper deposit at 10-14 Myrs. Another one is younger but older than 9.5 Myr.

Neogene basin infilling from cosmogenic nuclides (^{10}Be and ^{21}Ne) in Atacama, Chile: implications for paleoclimate and copper supergene enrichment.

Short Title: Cosmognics and exotic copper deposits in Atacama

Caroline Sanchez¹, Vincent Regard^{1*}, Sébastien Carretier¹, Rodrigo Riquelme², Pierre-Henri Blard³, Eduardo Campos², Stéphanie Brichau¹, Maarten Lupker⁴, and Gérard Hérail¹

¹GET, Université de Toulouse, CNRS, IRD, UPS, (Toulouse), France. 14 avenue Edouard Belin, 31400 Toulouse, France

²Depto. Ciencias Geológicas, Universidad Católica del Norte, Avenida Angamos 0610, 8 Antofagasta, Chile.

³Centre de Recherches Péetrographiques et Géochimiques, CRPG, UMR 7358, CNRS, Université de Lorraine, Vandoeuvre-lès-Nancy, France

⁴ETH, Geological Institute, Sonneggstrasse 5, 8092 Zurich, Switzerland

[⊗] These authors contributed equally.

* corresponding author: vincent.regard@get.omp.eu tel: +33 5 61 33 26 45

Acknowledgements

This work **received** support (both field and laboratory expenses) from **the IRD**. The PhD of CS was funded by UCN (Antofagasta) and CONICYT. **We would like to acknowledge Fondecyt project no. 1121049**. Other significant support was provided by COPEDIM and University Paul Sabatier. We acknowledge AMSA for pit access and sampling facilities. We are grateful to Régis Braucher and Laetitia Leanni for constructive discussions.

Abstract

Increasing evidence suggests that supergene exotic copper deposits were emplaced during periods of geomorphic quiescence and pulses of humidity in arid environments. We tested this idea in the Centinela Mining District in the Atacama Desert (northern Chile). We collected 14 sand samples at

29 depth (up to 110 m) in two open-pit mines (Central Tesoro and Mirador) exposing Miocene sediment,
30 and located in the El Tesoro Basin, which hosts two exotic copper-rich layers. We inverted the ^{10}Be and
31 ^{21}Ne concentrations by using a two-box model (IMIS, Inversion of Multi Isotopes in a Sedimentary
32 basin) composed of an eroding source of sediment and a depositional sedimentary basin, and by
33 selecting denudation and sedimentation rate histories that can explain our data. The ages found
34 demonstrate that the two exotic layers were deposited during a narrow period between <14 Ma (10
35 Ma younger than previously thought) and 9.5 Ma, when an ignimbrite covered the sedimentary
36 sequence. The dated lower exotic copper layer was deposited during or just before a sharp decrease
37 in the sedimentation rates (from >100 to 0.5-5 m/Ma), which is consistent with published
38 sedimentological and carbonate isotopic data in this district. This confirms the idea that exotic deposits
39 form during a quiescence of the geomorphic activity. Nevertheless, our model suggests that the back-
40 ground denudation rate providing sediment to these basins between ~14 Ma and ~9.5 Ma was
41 surprisingly high (>250 m/Ma) for such an arid environment. These denudation rates can be explained
42 by a relatively rapid back-scarp retreat providing most of the sediment to these basins and possibly a
43 wetter climate compared to the present. Then, during the period 10-7 Ma, the denudation rates
44 decreased to >50 m/Ma. This decrease may correspond to a progressive slope decrease of the hills
45 around, or to a progressive aridification, or a combination of both phenomena.

46 **Keywords:** supergene copper deposits; Atacama; cosmogenic nuclides; denudation rates; burial
47 dating; intramountainous basin

48

49 **1 Introduction**

50 The Atacama Desert in northern Chile and southernmost Peru hosts the biggest concentration of
51 world-class porphyry copper deposits on Earth (Sillitoe, 2010). Nearly all of these deposits show
52 features related to supergene processes that produce an increase in hypogene copper grades on top
53 of porphyry copper systems through reduction-oxidation reactions occurring during weathering

54 phases (e.g., Sillitoe 2010). The leached copper can reprecipitate above the water table as oxidized
55 minerals such as Chrysocolla and Atacamite or it can also be concentrated below the paleowater table
56 as secondary sulfides (e.g. chalcocite, covelite). Fluids containing leached copper may eventually
57 migrate laterally and transport copper up to several kilometers away from the weathered source of
58 metal, until the copper precipitates form exotic (away from the metal source) copper deposits (e.g.,
59 Münchmeyer 1996). Although the precise balance between precipitation, uplift and denudation rate
60 for the generation of these deposits has not been quantified yet, the formation of oxidized minerals
61 supergene (i.e., mineralized close to the Earth's surface) is usually considered to have occurred during
62 pulses of humidity in a context of an arid climate during the Neogene in the Atacama (e.g., Arancibia,
63 et al., 2006; Reich et al., 2009; Palacios et al., 2011b; Reich and Vasconcelos, 2015b; Fernández-Mort
64 et al., 2017b; Riquelme et al., 2018; Sanchez et al., 2018). Thus, the precipitation of oxidized minerals
65 is not only of particular interest to trace exploitable deposits, but also to reconstruct past climates.
66 Even though multi-approach studies tend to agree with the long-term aridity of the Atacama Desert,
67 the timing of the hyperaridity onset is still matter of debate (see Figure 1 for a review and references).
68 Nevertheless, the effect of rainfall is ambiguous. An increase in rainfall favors lixiviation and the lateral
69 transport of fluids from which oxidized minerals will precipitate. Meanwhile, higher surface runoff
70 favors erosion and thus removes the oxidized layer. Consequently, denudation of the porphyry copper
71 system is a key process to understanding the formation of supergene copper deposits (Alpers and
72 Brimhall 1988; Braxton et al. 2009). In this contribution, we show how the denudation rates of the
73 source area may impact the formation of exotic copper.

74 In the Centinela Mining District (Antofagasta region, Chile, Figure 2), recent sedimentological and
75 thermochronological studies have demonstrated that supergene copper mineralization related to
76 porphyry copper systems formed during pedimentation periods in the Miocene, corresponding to the
77 waning of the Domeyko range with mean denudation rates in the order of 100 m/Ma (Riquelme et al.
78 2018; Sanchez et al. 2018). In this district, Fernández-Mort et al. (2017) evidenced the role of

79 sedimentary environments in controlling exotic copper mineralization: copper minerals infilling the
80 sediment porosity in beds truncated by erosion indicate that exotic mineralization is syngenetic to
81 sedimentation and occurs near the surface under high evaporation rates, as expressed by C and O
82 isotopy. Fernández-Mort et al. (2017) showed that some exotic copper deposits form in ephemeral
83 distal lakes mainly by evaporation, while exotic copper deposited later mainly corresponds to the
84 erosion of pieces of previously formed exotic copper deposits and their downstream deposition in
85 sedimentary traps. Previous studies have suggested that low denudation and sedimentation rates are
86 needed for the deposition of exotic copper deposits. On the contrary, there has been no quantitative
87 estimate of the porphyry copper denudation rate and sedimentation rate in sedimentary traps during
88 the formation of exotic copper deposits.

89 Recent developments in cosmogenic nuclide analytical techniques for sediment have provided new
90 methods for estimating their paleo-denudation rates or burial ages (e.g., Balco and Shuster 2009;
91 Charreau et al. 2011; Sartégou et al. 2018), with applications to the Atacama Desert (Davis et al. 2014;
92 Madella et al. 2018). Here, we develop an approach based on two cosmogenic isotopes, ^{10}Be
93 (radioactive, half-life 1.39 Ma) and ^{21}Ne (stable). We collected 14 sand samples in a Neogene
94 sedimentary sequence exposed in two mine pits found in the Centinela Mining District (Figure 2): the
95 Tesoro Central pit, hosting two exotic copper deposits, and the Mirador pit, where supergene
96 mineralization and the related porphyry copper system outcrop. We developed a new two-box model
97 (called IMIS, Inversion of Multi Isotopes in a Sedimentary basin), with one box for the eroding source
98 of sediment and the other for the basin where they deposit. For various denudation and sedimentation
99 rates (either fixed or random) in these two boxes, the model predicts the ^{10}Be and ^{21}Ne concentrations
100 through time in the sedimentary sequence. Using a Monte Carlo approach, we minimize the difference
101 between predicted and measured concentrations to infer the best-fit scenario of denudation and
102 sedimentation and to establish a modeled age for the sediment sequence. This approach reveals subtle
103 variations through time and constrains the age of the studied exotic copper deposit. From these

104 results, we also discuss the age and the sedimentary response to the Late Miocene aridification of the
105 Atacama region.

106 **2 Geological background and sampling**

107 **2.1 Geological background**

108 The Centinela Mining District is located at approximately 23°S, in the Precordillera
109 physiographic unit of the Andean forearc (see location in Figure 1). It is bordered by the Central
110 Depression to the west and by the Atacama Salar to the east. In the district, several copper mines are
111 currently exploited: the Tesoro Central, Tesoro NE, Esperanza, Telegrafo, Mirador and Encuentro with
112 few exploration projects still under development (Tomlinson and Blanco 1997; Mpodozis and Cornejo
113 2012).

114 In the Precordillera, the Paleozoic-Triassic basement and the sedimentary cover (Jurassic
115 marine to Upper Cretaceous continental volcano-sedimentary rocks) host intrusives, related to the
116 Late Cretaceous to Eocene magmatic arc (Marinovic and García 1999; Mpodozis and Cornejo 2012).
117 These rocks have been faulted during the Eocene tectonic phase by the Domeyko Fault System
118 (Mpodozis et al. 1993; Amilibia et al. 2008; Mpodozis and Cornejo 2012). At the regional scale, the
119 activity of the fault system resulted in the creation of intra-mountainous basins such as the Centinela
120 Basin (Mora et al. 2004; Riquelme et al. 2018). This tectonic episode was synchronous to the
121 emplacement of the Eocene metallogenic belt. In the Centinela Basin, porphyry copper systems were
122 emplaced synchronously to the movement of faults related to the Domeyko Fault System, such as the
123 Tesoro Central, Tesoro NE, Llano, Centinela, and Esperanza faults (see Figure 2). **Late (< 10 Ma) fault**
124 **activity has resulted in the uplift of the western block where the central Tesoro mining pit is located,**
125 **with respect to the eastern block where the Mirador mining pit is located (Mpodozis and Cornejo**
126 **2012).**

127 Supergene copper mineralization over substratum rocks and exotic copper mineralization
128 hosted by gravel deposits can be found in the Centinela Basin (Fernández-Mort et al. 2017). The age
129 of the exotic copper mineralization is unclear due to the lack of datable material within the mineralized
130 sequence. Detailed sedimentary studies **have** identified four main gravel groups (Mora et al. 2004;
131 Riquelme et al. 2018). **The Esperanza and Atravesado gravels are younger than ~45 Ma and ~40 Ma**
132 **respectively (constrained by detrital zircon ages within the sedimentary sequence, Riquelme et al.**
133 **2018). The topmost sequence consists of the Tesoro and Arrieros gravels (Figure 2), in which a 9.5 Ma-**
134 **old ash layer is intercalated (De Silva, 1989, (Riquelme et al., 2018).**

135 In the Atacama Desert, several types of supergene minerals have been dated **by $^{40}\text{Ar}/^{39}\text{Ar}$ and K/Ar and**
136 **recently, for the first time, chrysocolla minerals were also dated from the Chuquicamata mine using**
137 **U-Pb; all together, these minerals yield ages mostly ranging from 25 to 9 Ma as well as a few ages as**
138 **young as the Pleistocene (Arancibia et al., 2006). A similar age range (25-12 Ma) has been found in the**
139 Centinela District using $^{40}\text{Ar}/^{39}\text{Ar}$ and K/Ar methods on supergene minerals (Sillitoe and McKee 1996;
140 Perelló 2010; Tapia et al. 2012; Riquelme et al. 2018). In the Tesoro NE mine (eastern pit), a single
141 exotic supergene mineral age obtained in a copper-rich layer was estimated at ~21 Ma. **It has been**
142 **proposed that the layer bearing this age is a** stratigraphic equivalent of the exotic copper layer
143 observed in the Teroso Central mining pit (Tapia et al. 2012; see location in Figure 2 and Figure 4).
144 These two mining pits (Tesoro Central and Tesoro NE pits) are structurally separated by the Tesoro
145 Fault (see **Error! Reference source not found.** et al., 2018).

146 **2.2 Geomorphic background: denudation rates and paleoclimate**

147 Long-term denudation rates in the Centinela District have been determined by low-
148 temperature thermochronology on Paleocene intrusives and Eocene porphyry copper deposits
149 (Sanchez et al. 2018). These data suggest that most of the exhumation had occurred before 30 Ma,
150 and **that the denudation rates have** dropped drastically since then (Maksaev and Zentilli 1999; Sanchez
151 et al. 2018). The supergene mineral ages in the area are younger than the main exhumation phase

152 (Arancibia et al., 2006; Sanchez et al., 2018) confirming that supergene copper mineralization occurs
153 in flat landscapes characterized by low relief and low denudation rates (Mortimer 1973; Alpers and
154 Brimhall 1988; Clark et al. 1990; Mote et al. 2001; Quang et al. 2005; Sanchez et al. 2018).

155 Several studies have estimated erosion (denudation) rates at the regional scale. In the Atacama
156 Desert in northern Chile (18-30°S), for example, the current denudation rates measured by river
157 sediment loads range from 0.1 to 10 m/Ma with a notable exception on the Lluta River (~43 m/Ma,
158 Carretier et al. 2018). At the millennium scale range, cosmogenic nuclides record catchment-scale
159 denudation rates up to ~60 m/Ma (Kober et al. 2009; Cortés-Aranda J. et al. 2012; Carretier et al. 2013;
160 see Figure 3).

161 At a local outcrop scale, cosmogenic nuclides have recorded *maximum* denudation rates values
162 in the range 0.01-50 m/Ma, with a median value lower than 1 m/Ma (Dunai, Lopez, and Juez-Larre
163 2005; Nishiizumi et al. 2005; Kober et al. 2007; Evenstar et al. 2009; Gattacceca et al. 2011; Cortés-
164 Aranda J. et al. 2012; Owen et al. 2011; Placzek et al. 2014; Martinod et al. 2016; Ritter, Stuart, et al.
165 2018; Amundson et al. 2012). The currently observed low denudation rates may have lasted for
166 millions of years, without significant change in elevation (Blard et al., 2019). Gypsisoil development
167 may provide evidence of ~10 Ma of hyper-aridity and landform stability (rainfall < 40 mm/yr, Rech et
168 al. 2006): this geomorphological stability is further confirmed by the regional observation of the Artola
169 ignimbrite dated at $\sim 9.52 \pm 0.02$ Ma covering most of the landscape surface, affected by minor
170 reworking after deposition (Riquelme et al. 2018).

171 On the contrary, there are few records of the paleo-denudation rate. Based on the cosmogenic
172 ^{10}Be data, from north of our studied area, Madella et al. (2018) determined paleo-denudation rates
173 ranging from 0.5 to 15 m/Ma for the period 10.3-12.8 Ma ago. On the basis of estimations of porphyry
174 copper weathering rates, Arancibia et al. (2006) estimated that the denudation was less than 16–35
175 m/Ma from the Oligocene to Late Miocene. Finally, Alpers and Brimhall (1988) determined that erosion
176 rates on the order of 100m/Ma enabled the exhumation of the La Escondida porphyry copper

177 sometime between 33.7 and 18 Ma. These authors postulate that erosion dramatically decreased to
178 less than 10m/Ma after ~15 Ma due to the onset of hyperaridity.

179 **2.3 Sampling**

180 A total of 14 samples were collected in the Centinela District, distributed in two different mine
181 pits (nine samples from the Tesoro Central pit and five from the Mirador pit, see the location in Figure
182 4).

183 These two mines present different types of secondary copper mineralization. In the Mirador
184 mine, the porphyry copper and related supergene mineralization is visible at the bottom of the pit. In
185 the case of the Tesoro Central mine, the copper mineralization is within a gravel sedimentary sequence
186 and corresponds to an exotic type copper deposit (described in Fernandez-Mort et al., 2017) (see
187 Figure 4 and Figure 5). In the Tesoro Central pit, samples were collected at depths between 65 and 135
188 meters, with a denser sampling around the copper-rich exotic layer (see details in Figure 4 and Figure
189 5). In the Mirador pit, sampling was performed between 10 and 65 meters deep (see Figure 4 and
190 Figure 5), above and below the 9.5 Ma-old Artola ignimbrite. On each sampling point, nearly 500 g of
191 fine-to-coarse sediment was collected.

192

193 **3 Methods based on cosmogenic nuclides**

194 **3.1 Basic systematics**

195 In-situ cosmogenic nuclides are produced within the Earth's surface material through nuclear reactions
196 (mostly spallation but also muonic capture) caused by cosmic rays. Spallation processes occur within a
197 couple of meters below the Earth's surface (e.g., Lal 1991; Gosse and Phillips 2001). The concentration
198 of *in situ*-produced nuclides (i.e., produced within the crystal lattice) reflects the time the mineral spent
199 in the production zone (c.a. from the surface to a few meters below the surface). This is controlled by

200 the date of exposure initiation, the local **denudation rate and the local production rate** (e.g., Bierman
 201 and Steig 1996; Brown et al. 1995). Moreover, it has been shown that due to fluvial processes, it is
 202 possible to determine **that the concentrations of cosmogenic nuclides in detrital sediments have**
 203 **reached steady-state and can be used to determine** the catchment-wide spatial average denudation
 204 rate (Brown et al., 1995; Granger, Kirchner, and Finkel 1996). **In addition, as some of the cosmogenic**
 205 **nuclides are radioactive (e.g. ^{26}Al , ^{10}Be), a decay term must be considered, but it does not depend on**
 206 **the surface processes.**

207 Apart from the 'simple exposure' scenario resolved by a single nuclide, two cosmogenic nuclides can
 208 be analyzed together to calculate the rock burial duration after having been exposed to cosmic rays at
 209 the Earth's surface (Granger and Muzikar, 2001). This technique relies on the fact that two cosmogenic
 210 nuclides are similarly produced **at the Earth's surface, when the production ratio is known. When the**
 211 **host minerals are buried, their concentration in the various cosmogenic nuclides decay differently,**
 212 **therefore the ratio between them evolves.** This is most often achieved using the $^{26}\text{Al}/^{10}\text{Be}$ pair of
 213 cosmogenic nuclides (Balco and Shuster 2009). The burial time t_b is given by Equation 1, where N_A and
 214 N_B are nuclide concentrations at time t , P_A and P_B are the respective production rates, λ_A and λ_B are the
 215 respective decay constants (value of 0 for stable nuclides) and f is the scaling factor at the exposure
 216 location (Blard et al., 2019).

$$217 \quad \frac{P_A}{N_A} e^{-\lambda_A t_b} - \frac{P_B}{N_B} e^{-\lambda_B t_b} = \frac{\lambda_A - \lambda_B}{f} \quad (\text{equation 1})$$

218 For a detrital basin such as the one studied here, the single clast cosmogenic nuclide concentration
 219 reflects a two-step-history (Figure 6).

220 **First, the pre-burial (initial) ratio of the paired nuclides ($R_{AB}(0)$) depends on the production rates and**
 221 **on the duration of the sediment residence in the source. $R_{AB}(0)$ is acquired either during steady-state**
 222 **denudation rates (ϵ in Figure 6) or following a more complex exposure history in the uplands with**
 223 **successive temporary storage along hillslopes and along the river system (Lal 1991; Balco and Shuster**
 224 **2009). Although transport durations of several tens of thousands years have been recently evidenced**

225 for large pebbles in a modern Atacama river (Carretier et al., 2019), the subsequent transport duration
226 from the catchment to the sedimentary basin is generally not long enough for a significant
227 concentration to build up. This pre-burial step, usually called “inheritance”, is fundamental as it
228 produces the cosmogenic nuclide content of newly-deposited sediments, which are used to decipher
229 the history. In the case where some of the sediments underwent various cycles of exposure and burial,
230 stable ^{21}Ne record the pre-burial history in a more dramatic manner than radioactive ^{10}Be . The
231 homogeneity of the results discussed in the following makes the possibility of a complex pre-exposure
232 improbable, except for two samples with high $^{21}\text{Ne}/^{10}\text{Be}$ ratios (e.g., samples ET-04 and MIR-11, Table
233 4). Finally, deposition within the sedimentary basin (at a rate S_r , Figure 6) leads to the second step of
234 cosmogenic nuclide build-up, and this latter step is more important for low sedimentation rates. In the
235 definition of t_b , it is assumed that the amount of cosmogenic nuclides produced during this step is
236 negligible. This assumption may be wrong during the Centinela Basin infilling: in this case, t_b instead
237 corresponds to a minimal estimation for the deposition time.

238 **3.2 In situ cosmogenic ^{10}Be and ^{21}Ne sample processing and measurements**

239 Samples were prepared using the standard procedures (see supplementary information). Once
240 pure quartz was obtained, the samples were split in two aliquots. The first one was used for ^{10}Be
241 analysis, at GET and ASTER (except MIR-10, see **Error! Reference source not found.**).

242 The second quartz aliquot was used to measure the cosmogenic ^{21}Ne concentration at the
243 CRPG Nancy noble gas lab (Table 3). During sample preparation, the grain morphology was checked.
244 Some particular grain shapes were observed. For instance, quartz minerals present bipyramidal shapes
245 (Figure 7) in sample MIR13-01, just above the 9.5 Ma-old ignimbrite (De Silva 1989; Riquelme et al.
246 2018). This crystal automorph shape suggests that it has a volcanic origin and was not transported over
247 a long distance. MIR13-01 quartz minerals are likely to come from upstream erosion of the 9.5 Ma-old
248 ignimbrite.

249 3.3 Simple burial

250 Following the systematics of cosmogenic nuclides, it is possible to derive a simple burial duration
251 knowing the present-day concentrations of two nuclides with different radioactive half-lives as well as
252 the scaling factor f (Equation 1). In practice, both the pre-burial exposure duration (or denudation rate)
253 and the local production rate determines the pre-burial nuclides ratio, $R_{AB}(0)$ (Blard et al., 2019).
254 However, when it is buried at low depth (< 10 m) or shielded by a slow sedimentation rate (< 10 m/Ma),
255 the material is still exposed to cosmic rays. Hence, this results in an apparent burial duration (t_b) shorter
256 than its real value. Burial durations computed with Equation 1 without any post deposition correction
257 thus yield an end-member that is a minimum deposition time (t_b).

258 3.4 Inversion

259 We developed an R (R Core Team 2014) inversion program, called IMIS (available at
260 <https://github.com/regard-vincent/IMIS>). It is based on a Monte Carlo approach, taking into account
261 the evolution of the cosmogenic nuclide concentrations in a two-step clast history (Figure 6). The first
262 step corresponds to the catchment denudation (box 1, Figure 6), neglecting the duration of the fluvial
263 sediment transport to the basins. The catchment elevation is set to the current elevation of the basin.
264 This choice is motivated by the following reasons: (1) there is evidence that the ancient total catchment
265 relief was low (no more than several hundreds of meters; (2) the elevation of the basin may have
266 changed, which means that our results are still valid, as mentioned in the discussion; and (3) further
267 sensitivity tests indicate this is not critical for our analysis. The catchment denudation rate is allowed
268 to vary in the code but is fixed in the inversions as presented in the following. This step allows to
269 estimate the nuclide concentration from Equation 2 where P is the surface production, λ is the decay
270 constant, ϵ is the denudation rate, ρ is the density and Λ is the attenuation coefficient; i denotes the
271 various production pathways, usually spallation, and fast and stopped (negative) muons (see Brown et
272 al. 1995; Granger, Kirchner, and Finkel 1996; Heisinger et al. 2002a; Heisinger et al. 2002b; Dunai 2010;
273 Braucher et al. 2011). P depends on the elevation of the source rock; the sensitivity tests showed that,

274 in this context, potential changes in elevation did not significantly impact the results presented
 275 hereafter.

$$276 \quad C = \sum_i \frac{P_i}{\lambda + \frac{\rho \varepsilon}{\Lambda_i}} \text{ (Equation 2)}$$

277 The second step corresponds to the sedimentation in the basin (box 2, Figure 6).

278 In our model, the basin infill is divided into periods, each being bounded by well-defined events such
 279 as the current surface, or in our case, the emplacement of the Artola ~9.5 Ma-old ignimbrite layer. A
 280 period is divided into various sub-periods with a random duration and a random sedimentation rate;
 281 the duration and thicknesses follow uniform laws whereas the sedimentation rate corresponds to the
 282 ratio between thickness and duration. The number of sub-periods is fixed to seven, typically. The total
 283 sedimentation during a period is adjusted (by a multiplication ratio) to satisfy its stratigraphic
 284 thickness. The basement rock and sediment densities are set to 2700 kg/m³ and 2300 kg/m³,
 285 respectively. Once a scenario has been drawn with its succession of sub-periods with specified
 286 sedimentation rates and durations, the model time is subsampled into time steps of 5 ka to compute
 287 the ¹⁰Be and ²¹Ne concentrations, as described in the following.

288 During each time step, we compute the concentrations of ¹⁰Be and ²¹Ne in two steps, first in box 1 and
 289 then in box 2. In box 1, the ¹⁰Be and ²¹Ne concentrations are calculated depending on their respective
 290 production rates at the elevation of the catchment, and the average catchment denudation (Equation
 291 2). These concentrations are attributed to the newly deposited surface layer in the basin in box 2. At
 292 each time step, the ¹⁰Be and ²¹Ne concentrations in all of the deeper layers in the basin are updated
 293 taking both the decay of ¹⁰Be and the undersurface production of ¹⁰Be and ²¹Ne over the last 5 ka
 294 (duration of one-time step) into account. This production strongly depends on the production scheme.
 295 The production at depth is often modelled with an exponential attenuation (although not for model
 296 HS, see below):

$$297 \quad P_i(z) = P_i(z = 0).e^{-\rho z / \Lambda_i}. \text{ (Equation 3)}$$

298 Since there are different models describing the attenuation of ^{10}Be and ^{21}Ne production at depth that
 299 we explore in this study; we detail these models below. In the eroding areas (box 1), we only use one
 300 exponential attenuation scheme, while we use several schemes in the sedimentation area, called GH,
 301 BH, HS, BR (See **Error! Reference source not found.** and Figure 8 for more details). The first letter
 302 stands for the ^{10}Be production scheme: G for Granger and Muzikar (2001), B for Braucher et al. (2011),
 303 H for Heisinger et al. (2002). The second letter is indicative of the ^{21}Ne production scheme: H and S for
 304 Heisinger et al. (2002) and R for Braucher et al. (2011); ^{10}Be production SLHL is set to 4.15 at/g/a
 305 (Martin et al., 2017), and the $^{21}\text{Ne}/^{10}\text{Be}$ ratio is 4.12 (Balco and Shuster 2009a; Kober et al., 2011). As
 306 we will see, the production parameter choice has a strong influence on the modeled concentration
 307 and subsequently on the misfit between the measured concentrations and their modeled values.

308 Once the ^{10}Be and ^{21}Ne concentrations have been updated, new ^{10}Be and ^{21}Ne concentrations are
 309 computed for box 1, which themselves are assigned to a new surface layer of box 2 and so on for the
 310 different time steps until the total duration of the modeled period is reached. This endpoint is reached
 311 when the basin is filled.

312 The procedure described above constitutes a forward model that is run 5,000 times for different
 313 denudation and sedimentation scenarios in a Monte Carlo simulation. The best model parameters are
 314 then selected by minimizing the χ^2 misfit metric between the predicted and measured ^{10}Be and ^{21}Ne
 315 concentrations, defined by Equation 2.

$$316 \quad \chi^2 = \sum_i \left(\frac{C_{obs,i} - C_{mod,i}}{Err_i} \right)^2 \quad (\text{Equation 4})$$

317 where $C_{obs,i}$, $C_{mod,i}$ and Err_i are, respectively the observed concentration, the modelled concentration
 318 and associated analytical uncertainty for the sample n# i. For each Monte Carlo set of inversions, we
 319 calculated three minimum χ^2 values, one for each single nuclide (the concentrations in Equation 2 are
 320 only ^{10}Be or ^{21}Ne ones) and one **considering together** the misfit for the two nuclides (**χ^2 calculated on**
 321 **the entire set of ^{10}Be and ^{21}Ne data**).

322 In order to validate our inversion model, IMIS, we tested it on Davis et al.'s dataset (2014) from the
323 Atacama Desert gravels near our study zone. It provides similar results to the inversions processed by
324 Davis et al. (2014); see supplementary material.

325 4 Results

326 4.1 Concentrations

327 Concentrations (Tables 2 and 3) are comprised between $(6 \pm 4) \times 10^6$ and $(1.38 \pm 0.09) \times 10^8$ at/g for
328 ^{21}Ne (plus three samples that are below the detection limit) and are measurable for ^{10}Be (from
329 $(1.8 \pm 0.3) \times 10^3$ at/g to $(9.70 \pm 0.32) \times 10^5$ at/g), indicating that the minimum burial duration **must be**
330 less than ~ 18 Ma (in the case where the initial concentration is high, as in the present case), the time
331 corresponding to the minimum detectable ^{10}Be concentration (Table 2 and Table 3).

332 4.2 Burial ages

333 Assuming that these samples underwent a single and instantaneous burial episode, these data indicate
334 a burial duration (i.e. minimum deposition time) ranging from 6 to 18 Ma (**Error! Reference source not**
335 **found.**). In the Tesoro Central pit, the obtained burial ages are relatively homogeneous along the
336 stratigraphic column, around 11 Ma. These burial ages slightly increase from ~ 11 (~ 59 m-deep) to ~ 13
337 Ma 111 m below the surface (cf. **Error! Reference source not found.**). The samples located near the
338 enriched copper layer display ages between 11 and 13 Ma. In the Mirador pit, the burial times reflect
339 the stratigraphic order from ~ 7 Ma for the top samples, to ~ 14 Ma at a depth of 45 m below the surface.
340 We decided to discard ET-04, because it is hard to reconcile it with the other data, as the burial duration
341 of this sample is at odds with the stratigraphic order. This material probably underwent several
342 exposure-burial cycles. Moreover, taking ET-04 into account increases the minimum χ^2 by one order of
343 magnitude. Our reference inversion (production parameter BR, denudation rate = 5.10^{-4} m/a,

344 discussed below) gives two important clues. First, the deposition of the copper-rich layer is likely 10-
345 14 Ma old (Figure 9), and is followed by a stage of rapid sedimentation ($\sim 10^{-4}$ m/a, cf. appendix). In
346 fact, our misfit metric χ^2 is not very sensitive to input parameters, because the uncertainties are high
347 compared to the measured concentrations (10-30% for ^{10}Be , **Error! Reference source not found.**, 6-
348 70% for ^{21}Ne , Table 3). Our interpretations are thus robust and have limited dependency on the
349 production scheme used (see appendix).

350

351

352 In the Mirador mining pit, the burial times reflect the stratigraphic order, from ~ 7 Ma for the top
353 samples to ~ 14 Ma at a depth of 45 m below the surface. The upper ~ 7 Ma samples stand just above
354 the 9.5 Ma-old Ar/Ar dated Artola ignimbrite, while the ~ 14 Ma deep samples are located dozens of
355 meters below this (Figure 5). This observation indicates that the $^{21}\text{Ne}/^{10}\text{Be}$ burial durations (despite
356 being minimal, not taking the production during deposition into account) are in agreement with the
357 stratigraphic order (**Error! Reference source not found.**). Data from the Mirador pit better constrain
358 sedimentation rate than the burial times, because the sedimentation rate is more efficient at varying
359 the concentrations than radioactive decay.

360 **4.3 Paleo-denudation and sedimentation rates, determined by forward** 361 **modelling**

362 The initial ^{21}Ne concentration in the sediments is the sum of ^{21}Ne acquired before the deposition,
363 mostly during the material exhumation by denudation on hillslopes and ^{21}Ne produced during
364 sedimentation. In the particular case of similar sedimentation and denudation rates, occurring at a
365 similar elevation, half of the ^{21}Ne concentration comes from exposure on eroding hillslopes and half
366 from sedimentation. In this case, Equation 2 can be inverted to obtain an integrated sedimentation
367 and denudation rate. This sedimentation/denudation rate should therefore be interpreted as a

368 minimum estimate for both denudation and sedimentation. For Mirador, this minimum is in the range
369 0.9-12 m/Ma, a value that can be regarded as similar to modern values (cf. Martinod et al. 2016;
370 Carretier et al. 2018). For Tesoro Central, this minimum is higher, except for ET-04 and lies around 20
371 m/Ma. The apparent disagreement likely comes from the fact that the samples are from different
372 stratigraphic layers with different ages and therefore corresponding to different periods in the basin
373 infilling history.

374 Various forward calculations were performed, with different source area denudation rates. First, for
375 The Tesoro Central pit, the denudation rate is set to a low value for the last 10 Ma (its value has little
376 implication for the inversion), and to a higher value for the older stages. A denudation rate of
377 500 m/Ma is used for reference; as seen in the following, a high denudation rate is needed to explain
378 the low cosmogenic nuclide concentrations observed in the sedimentary column. Inversions can hardly
379 produce low cosmogenic nuclide concentrations, irrespective of the muonic production scheme. The
380 surface position did not vary much for the last 10 Ma, leaving time for significant production at depth.
381 Hence, low concentrations cannot be easily modeled (modeled concentrations are most often too high
382 compared to the observed data, Figure 10). Furthermore, we found that the inversions for the Tesoro
383 Central pit cannot reach satisfactory values for source denudation rates lower than 250 m/Ma for the
384 pre-9.5 Ma period (see Figure 11 and Table 5).

385 For the post-10 Ma period, we performed a forward model on the Mirador dataset, with different post-
386 10 Ma denudation rates. For these latest stages, the results are affected by a lower uncertainty since
387 the sampling of the Mirador site is denser. Best fits (low χ^2) yield relatively high denudation rates,
388 higher than 50 m/Ma for the period 7-9.5 Ma (Figure 12. Figure 12).

389 **4.4 Additional constraints on the copper-rich layer (Tesoro Central)**

390 Our $^{10}\text{Be}/^{21}\text{Ne}$ data constrain the deposition age of the copper-rich layer in the Tesoro Central mining
391 pit between 14 and 10 Ma. Moreover, the ^{10}Be concentration clearly increases towards the surface
392 (Figure 10.A) as does ^{21}Ne (due to larger analytical uncertainties, this tendency is however questionable

393 for ^{21}Ne , Figure 10.B). This suggests either a slow sedimentation rate during the deposition of the
394 copper-bearing layer or a hiatus just after its deposition: the ^{10}Be best fits usually imply a
395 sedimentation rate of the order of 0.5-5 m/Ma. This observation is confirmed by inversions for ^{10}Be ,
396 where the modelled concentrations exhibit a peak of concentration near the top of the copper-bearing
397 layer (Figure 10), with minimum sedimentation rates of 0.5-5 m/Ma for best fit scenarios. These
398 features are observed for 90-100% of the ^{10}Be best inversion models (i.e. with varying sedimentation
399 rates and production schemes); these conclusions are not sensitive to the muonic production scheme.

400 5 Discussion

401
402 Cosmogenic nuclide data show that the deposition of the copper-rich layer occurred during or just
403 before a period of low sedimentation rates sometime between 10 and 14 Ma ago.

404 *Robustness of the analysis*

405 The analysis was performed for a source elevation of 2200 m, similar to the current mining pit
406 elevation. It is possible that the source elevation was different at the time of deposition. The effect of
407 this would be a higher initial content in cosmogenic nuclides (the production at 3000 m above sea level
408 is 50% more than at 2200 m). Assuming an elevation that, 15 Ma ago, was 1000 m higher than today
409 and considering that an important episode of Andean uplift has been documented as having occurred
410 in the Miocene (probably a maximum given that the apatite fission tracks and U-Th/He ages are older
411 than 30 Myr in this area; Sanchez et al. 2018) the difference in the cosmogenic nuclide concentration
412 due to a production rate variation would be lower than those due to the variations in the denudation
413 rates that we explored (1-1000 m/Ma). As a result, we consider our findings to be robust regardless of
414 the initial elevation: the denudation rate thresholds discussed in the next paragraph are slightly offset
415 towards higher denudation rates for higher source areas. It is also possible that the Chilean forearc
416 was uplifted ~ 1 km in late Miocene (e.g., Riquelme et al. 2003; Jordan et al. 2014). In that case, all of

417 our samples may have been eroded and deposited at lower elevation, with a smaller production rate.
418 Again, this difference is included in the range of denudation rates tested. We also tested the effect of
419 the density used for the sedimentary column: varying it between 1800 and 2500 kg/m³ only changes
420 our conclusions with regards to younger sedimentation ages for denser sediment infilling. It does not
421 significantly affect our deductions and only shifts our conclusions towards slightly younger
422 sedimentation ages if the material density is considered (cf. Supporting Information). The fit is slightly
423 better for higher densities because a higher density limits the cosmogenic nuclide production in
424 samples at great depth. For these samples, the predicted cosmogenic nuclide concentrations are too
425 high, particularly with low source denudation rates.

426 The two pits investigated are complementary and provide information about the history of the
427 denudation/sedimentation rates (Table 5). Data from the Tesoro Central pit show that, before 9.5 Ma
428 ago, there was a period of rapid sedimentation (more than 50 m/Ma) of a material produced in a
429 source area subject to high denudation (more than 250 m/Ma). This period was probably short,
430 spanning about 1 Ma, the exact timing of which remains unclear: sometime between 14 and 10 Ma
431 ago. The short duration of this episode of rapid sedimentation makes it compatible with the long-term
432 averaged low denudation rates recorded in the area (16-35 m/Myr from the Oligocene to late Miocene;
433 Arancibia, Matthews, and De Arce 2006). After 9.5 Ma (and before ~7 Ma ago), the source denudation
434 rate and basin sedimentation dropped but remained significant, probably higher than 50 m/Ma. This
435 is higher than what was observed by Davis et al. (2014) for the same period further south (1-10 m/Ma).
436 In the two pits, the sedimentation rate post 9.5 Ma is lower than 2 m/Ma, which is similar to what
437 Davis et al. (2014) observed (Table 5).

438 Currently, the Centinela Basin is fed by a 2041 km²-wide catchment. The sedimentary basin itself has
439 a surface area of 204 km², or one tenth of the catchment area. If all of the sediment was retained by
440 the basin, its long-term sedimentation rate would be ten times the denudation rate. If a sediment by-
441 pass occurred, this rate should be less. Assuming that the feeder catchment has not changed much

442 over the last 15 Ma, which seems reasonable for the Atacama, a catchment denudation rate as high as
443 250 m/Ma would have filled the Centinela Basin in a very short amount of time (50 ka). This duration
444 may be correct, corresponding to a very transitory stage; our data cannot rule it out. This duration
445 could also be overestimated due to a smaller contributing area, as proposed below.

446 ***High denudation rates for the Atacama***

447 It is surprising that large denudation/sedimentation rates occurred after the exotic copper deposition
448 (sometime between 10 and 14 Ma BP) and before the 9.5 Ma-old ignimbrite, while hyper-aridity was
449 established (e.g., Sillitoe and McKee 1996; Dunai, Lopez, and Juez-Larre 2005; Rech et al. 2006; Rech
450 et al. 2010; Evenstar et al. 2009; Jordan et al. 2014; Oerter et al. 2016). Sedimentation rates up to
451 100 m/Ma and denudation rates of more than 250 m/Ma are unexpected and have never been
452 mentioned in the literature (Carretier et al. 2018), with the exception of the very rapid incision rate of
453 the Loa River in the Pleistocene (~1800 m/Ma; Ritter et al., 2018). For example, paleo-denudation rates
454 deduced from ¹⁰Be concentrations in sediment from the El Diablo formation, 400 km north of our study
455 area, have remained on the order of 1-15 m/Ma between 12.8 and 10.3 Ma ago (Madella et al. 2018).
456 Yet, our findings appear robust with respect to different cosmogenic scaling schemes. Compared to
457 long-term denudation rates, these values > 250 m/Ma are still high. The thermochronological data
458 provided by Sanchez et al. (2018) obtained in this area imply 2.5 to 3 km of denudation during the last
459 30-50 Ma (average denudation rates of 50-100 m/Ma). Considering that the denudation occurred
460 mainly before 10 Ma ago (e.g., Arancibia et al., 2006; Riquelme et al., 2018), the average denudation
461 rates deducted from the data of Sanchez et al. (2018) increase up to 150 m/Ma (denudation of 3 km
462 during the period 30-10 Ma ago). One probable scenario is the occurrence of a wetter period before
463 10 Ma ago. In fact, Ritter et al. (2018) showed that river incision is strongly limited by the available
464 water in Atacama. By dating a Pleistocene lake to the north of the Centinela District, they found that
465 the ~500 m incision of the Loa River occurred very rapidly in the last ~270 ka, during a wetter period.

466 If the climate alone is responsible for these large paleo-denudation rates, then hyper-aridity must have
467 taken place in this particular area at about 10 Ma ago.

468 A second possibility is that the sedimentation was constrained by fault activity. For example, Sanchez
469 (2017) produced thermochronological data suggesting activity of a nearby major fault in late Miocene
470 between the Precordillera and the Atacama Salar (see location in Figure 2.A). In this case of active
471 tectonics, the expected denudation/sedimentation signal must have been transient, with fast
472 denudation/sedimentation.

473 To explain these high denudation rates, another hypothesis could be that the basin records a regressive
474 erosion wave during pediment emplacement (Figure 13). Based on sedimentological facies and detrital
475 zircons, Riquelme et al. (2018) proposed a pedimentation phase during late Miocene in the same area
476 based on sedimentological and provenance evidence. The existence of persistent steep and elongated
477 reliefs in the region, interpreted as back-scarp relief (Paskoff 1977; Riquelme et al., 2018) suggests that
478 the pedimentation process could have been preceded by back-scarp retreat (Figure 13). Locally at the
479 position of the back-scarp, where the topography is steeper, the denudation rates may be much higher
480 than the average regional value (Strudley and Murray 2007), providing most of the sediment delivered
481 to our study basins. This average regional denudation rate could therefore have been higher 10 Ma
482 ago (see next paragraph). A higher transient and localized denudation rate would be consistent with
483 the strong slope control of the watershed denudation rate documented in Chile (Carretier et al., 2013)
484 and elsewhere (e.g. Binnie et al., 2007).

485

486 ***Hyperaridity onset timing***

487 The date for the onset of hyperaridity in Atacama has been extensively discussed based on
488 sedimentological arguments (e.g., Hartley and Chong 2002), surface exposure ages (e.g., Dunai et al.,
489 2005) and supergene mineralization ages (e.g., Reich et al., 2009). The proposed timing for hyper-
490 aridification includes Oligocene to Pleistocene ages, and progressive-to-abrupt changes. Ritter et al.

491 (2018) proposed that this debate can be reconciled by taking local climates in Atacama into account.
492 According to these authors, the driest places can have undergone hyper-arid conditions since late
493 Miocene or even Oligocene, whereas other locations have been subjected to varying conditions with
494 alternating arid periods and wetter local conditions. Our data strongly suggest that, during the
495 Neogene, there was a decrease in the denudation rates of the hills in this Atacama region that have
496 provided sediments to our studied basin. The average denudation rate decreased from > 250 m/Ma
497 between 14-10 Ma (Tesoro Central data) to > 50 m/Ma between 9.5-7 Ma (Mirador data). Nowadays,
498 these rates are much lower at < 10 m/Ma (e.g., Placzek et al., 2010; Ritter et al., 2018). This decrease
499 can be explained solely by the hills surrounding the Centinela basins having a smaller slope (Figure 13).
500 The pedimentation and progressively increasing distance between the source and the basin evidenced
501 by Riquelme et al. (2018) during the Miocene must have been associated with a scarp retreat and relief
502 decrease, as well as decreasing denudation rates. The slope is indeed a decisive control on denudation
503 in Chile (Carretier et al., 2018). This does not discard the possibility that progressive hyper-aridification
504 during the Neogene also contributed to the documented denudation decrease. Furthermore, in the
505 basin at the Tesoro Central pit, the sedimentation rate dropped sharply after ~10 Ma. As discussed
506 above, local tectonic conditions controlling the accommodation space as well as the upstream
507 variations in the source area may explain this decrease. Recent research on the eastern border of the
508 Precordillera suggests that local exhumation occurred during the Mid-Miocene from which we can
509 assume a reactivation of the drainage and a higher denudation rate (Sanchez et al., in prep). This does
510 not discard the hypothesis that hyperaridification played a role. In conclusion, both geomorphological
511 and climatic variations can explain our data.

512 ***Supergene copper layer dating***

513 In this framework, the Tesoro Central copper-bearing layer is likely to be 10-14 Ma-old (Figure 9). It is
514 important to note that this age cannot be much older, simply because there would be no detectable
515 ¹⁰Be left in the deepest samples. This age is much younger than the age of ~21 Ma attributed to this

516 layer by lateral correlation (Oerter et al., 2016) with another exotic layer in the Tesoro NE pit found at
517 a distance of 3 km (Figure 2), where supergene minerals were dated by Riquelme et al. (2018). On the
518 contrary, our ages correspond well to the age range of other supergene mineralizations dated at 15-
519 12 Ma in the same district (Figure 2) (Riquelme et al., 2018). This implies that the other exotic deposit
520 in Tesoro Central, above the one we dated, is younger than 10-14 Ma and older than the 9.5 Ma
521 ignimbrite. We therefore provide the first evidence of two exotic deposits in this district in a restricted
522 period between 14 and 9.5 Ma. The exotic layer we have dated corresponds to a particular stage in
523 the geomorphological evolution of this region. It terminates with a stage of low sedimentation
524 (preceding the episode of high sedimentation), for which the best inversions of the ^{10}Be data give
525 median values around 0.5-5 m/Ma. This low sedimentation rate, contemporaneous with the
526 supergene mineralization, is consistent with other studies on the same copper-bearing layer. The low
527 field magnetic susceptibility (AMS) has shown that exotic copper deposits correspond to lower
528 sedimentation rates (Pizarro et al., 2018). Copper minerals infilling the sediment porosity in beds
529 truncated by erosion indicate that exotic mineralization is syngenetic to sedimentation and occurs near
530 the surface under high evaporation rates, as expressed by C and O isotopy (Fernández-Mort et al.,
531 2017).

532

533 6 Conclusions

534 In this study we have combined data from two cosmogenic nuclides (^{10}Be and ^{21}Ne) in order to date
535 and rate mid-Miocene denudation and clastic deposition rates with the aim to better understand the
536 evolution of the late Miocene landscape and the conditions in which exotic copper deposits form in
537 the Atacama Desert.

538 For the first time, we have proven that in-situ produced cosmogenic nuclides (here the $^{10}\text{Be}/^{21}\text{Ne}$ pair)
539 are useful to provide constraints on the dynamics, age, and conditions of an ore deposit formation:

540 the studied exotic layer deposited between 10 and 14 Ma ago, which is almost 10 Ma younger than
541 previously reported by lateral correlation. Moreover, the vertical profile within this layer suggests that
542 it emplaced during a low-deposition rate (quiescent) episode (sedimentation rate of the order of few
543 m/Ma). Exotic copper mineralization is probably promoted by a near-surface position under a high-
544 evaporation setting (Pizarro et al., 2018; Fernández-Mort et al., 2017).

545 Our $^{10}\text{Ne}/^{21}\text{Ne}$ data also established the temporal evolution of the denudation rates in the area which
546 drop around 10 Ma, confirming in the Atacama Desert the onset of hyperaridity in late Miocene
547 proposed by other authors. The current extremely low denudation rate (of the order of 1 m/Ma) has
548 not been continuous for the last 10 Ma. Our data records a > 50 m/Ma denudation rate for the period
549 ~7-10 Ma ago. The preceding period (roughly 10-14 Ma ago) recorded even higher denudation rates,
550 of more than 250 m/Ma, contemporaneous to sedimentation rates over 50 m/Ma. The decrease in the
551 post-14-10 Ma denudation rates records either a progressive aridification of the climate or a slope
552 decrease associated with active tectonics or pediment development, or possibly both phenomena
553 acting at the same time. Consequently, we do not recommend using our results to argue for a
554 progressive (using the paleo-denudation record), or drastic (using the paleo-sedimentation record)
555 establishment of hyperaridity. Our data further support the hypothesis that 14-10 Ma was a crucial
556 time for the landscape evolution in the western Central Andes and that this change (whatever it is,
557 tectonic and/or climatic) was concomitant with the occurrence of copper mineralizations.

558 The success of our analysis was probably favored by the local large thickness of the sedimentary
559 deposits, allowing for more-detailed records than elsewhere within the regional framework. Although
560 sediments this old (> 10 Ma) have only rarely been used for cosmogenic nuclide analyses, our work
561 provides evidence for the potential of cosmogenic nuclide geochemistry and helps push the limits of
562 this technique following recent advances (e.g., Charreau et al. 2011; Davis et al. 2014; Val and Hoke
563 2016; Madella et al. 2018).

564 **References**

- 565 Alpers, C. N., & Brimhall, G. H. (01). Middle Miocene climatic change in the Atacama Desert,
566 northern Chile: Evidence from supergene mineralization at La Escondida. *GSA Bulletin*,
567 *100*(10), 1640–1656. [https://doi.org/10.1130/0016-](https://doi.org/10.1130/0016-7606(1988)100<1640:MMCCIT>2.3.CO;2)
568 [7606\(1988\)100<1640:MMCCIT>2.3.CO;2](https://doi.org/10.1130/0016-7606(1988)100<1640:MMCCIT>2.3.CO;2)
- 569 Amilibia, A., Sàbat, F., McClay, K., Muñoz, J., Roca, E., & Chong, G. (2008). The role of
570 inherited tectono-sedimentary architecture in the development of the central Andean
571 mountain belt: Insights from the Cordillera de Domeyko. *Journal of Structural Geology*,
572 *30*(12), 1520–1539.
- 573 Amundson, R., Dietrich, W., Bellugi, D., Ewing, S., Nishiizumi, K., Chong, G., Owen, J.,
574 Finkel, R., Heimsath, A., Stewart, B., & Caffee, M. (2008). Geomorphologic evidence
575 for the late Pliocene onset of hyperaridity in the Atacama Desert. *GSA Bulletin*, *124*(7–
576 *8*), 1048–1070. <https://doi.org/10.1130/B30445.1>
- 577 Arancibia, G., Matthews, S. J., & Pérez de Arce, C. (2006). K–Ar and ⁴⁰Ar/³⁹Ar
578 geochronology of supergene processes in the Atacama Desert, Northern Chile: Tectonic
579 and climatic relations. *Journal of the Geological Society*, *163*(1), 107–118.
- 580 Arnold, M., Merchel, S., Bourlès, D. L., Braucher, R., Benedetti, L., Finkel, R. C., Aumaître,
581 G., Gottang, A., & Klein, M. (2010). The French accelerator mass spectrometry facility
582 ASTER: Improved performance and developments. *Nuclear Instruments and Methods*
583 *in Physics Research Section B: Beam Interactions with Materials and Atoms*, *268*(11),
584 1954–1959. <https://doi.org/10.1016/j.nimb.2010.02.107>
- 585 Balco, G. (2017). Production rate calculations for cosmic-ray-muon-produced ¹⁰Be and ²⁶Al
586 benchmarked against geological calibration data. *Quaternary Geochronology*, *39*, 150–
587 173.
- 588 Balco, G., & Shuster, D. L. (2009a). ²⁶Al–¹⁰Be–²¹Ne burial dating. *Earth and Planetary*
589 *Science Letters*, *286*(3), 570–575. <https://doi.org/10.1016/j.epsl.2009.07.025>
- 590 Balco, G., & Shuster, D. L. (2009b). Production rate of cosmogenic ²¹Ne in quartz estimated
591 from ¹⁰Be, ²⁶Al, and ²¹Ne concentrations in slowly eroding Antarctic bedrock
592 surfaces. *Earth and Planetary Science Letters*, *281*(1), 48–58.
593 <https://doi.org/10.1016/j.epsl.2009.02.006>
- 594 Bierman, P., & Steig, E. J. (1996). Estimating Rates of Denudation Using Cosmogenic Isotope
595 Abundances in Sediment. *Earth Surface Processes and Landforms*, *21*, 125–139.
596 [https://doi.org/10.1002/\(SICI\)1096-9837\(199602\)21:2<125::AID-ESP511>3.0.CO;2-8](https://doi.org/10.1002/(SICI)1096-9837(199602)21:2<125::AID-ESP511>3.0.CO;2-8)
- 597 Binnie, S. A., Phillips, W. M., Summerfield, M. A., & Fifield, L. K. (2007). Tectonic uplift,
598 threshold hillslopes, and denudation rates in a developing mountain range. *Geology*,
599 *35*(8), 743–746.
- 600 Blard, P.-H., Lupker, M., & Rousseau, M. (2019). Paired-cosmogenic nuclide paleoaltimetry.
601 *Earth and Planetary Science Letters*, *515*, 271–282.
602 <https://doi.org/10.1016/j.epsl.2019.03.005>

- 603 Braucher, R., Guillou, V., Bourlès, D. L., Arnold, M., Aumaître, G., Keddadouche, K., &
604 Nottoli, E. (2015). Preparation of ASTER in-house $^{10}\text{Be}/^{9}\text{Be}$ standard solutions.
605 *Nuclear Instruments and Methods in Physics Research Section B: Beam Interactions*
606 *with Materials and Atoms*, 361, 335–340. <https://doi.org/10.1016/j.nimb.2015.06.012>
- 607 Braucher, R., Merchel, S., Borgomano, J., & Bourlès, D. L. (2011). Production of cosmogenic
608 radionuclides at great depth: A multi element approach. *Earth and Planetary Science*
609 *Letters*, 309(1–2), 1–9. <https://doi.org/10.1016/j.epsl.2011.06.036>
- 610 Braxton, D. P., Cooke, D. R., Ignacio, A. M., Rye, R. O., & Waters, P. J. (2009). Ultra-Deep
611 Oxidation and Exotic Copper Formation at the Late Pliocene Boyongan and Bayugo
612 Porphyry Copper-Gold Deposits, Surigao, Philippines: Geology, Mineralogy,
613 Paleoaltimetry, and their Implications for Geologic, Physiographic, and Tectonic
614 Controls. *Economic Geology*, 104(3), 333–349.
615 <https://doi.org/10.2113/gsecongeo.104.3.333>
- 616 Brown, E. T., Edmond, J. M., Raisbeck, G. M., Yiou, F., Kurz, M. D., & Brook, E. J. (1991).
617 Examination of surface exposure ages of Antarctic moraines using in situ produced
618 ^{10}Be and ^{26}Al . *Geochimica et Cosmochimica Acta*, 55(8), 2269.
- 619 Brown, E. T., Stallard, R. F., Larsen, M. C., Raisbeck, G. M., & Yiou, F. (1995). Denudation
620 rates determined from the accumulation of in situ-produced ^{10}Be in the luquillo
621 experimental forest, puerto rico. *Earth and Planetary Science Letters*, 129(1–4), 193.
- 622 Carretier, S., Tolorza, V., Regard, V., Aguilar, G., Bermúdez, M. A., Martinod, J., Guyot, J.-
623 L., Hérail, G., & Riquelme, R. (2018). Review of erosion dynamics along the major N-S
624 climatic gradient in Chile and perspectives. *Geomorphology*, 300, 45–68.
625 <https://doi.org/10.1016/j.geomorph.2017.10.016>
- 626 Carretier, Sébastien, Regard, V., Vassallo, R., Aguilar, G., Martinod, J., Riquelme, R., Pepin,
627 E., Charrier, R., Hérail, G., Farias, M., Guyot, J.-L., Vargas, G., & Lagane, C. (2013).
628 Slope and climate variability control of erosion in the Andes of central Chile. *Geology*,
629 41(2), 195–198. <https://doi.org/10.1130/g33735.1>
- 630 Charreau, J., Blard, P.-H., Puchol, N., Avouac, J.-P., Lallier-Vergès, E., Bourlès, D., Braucher,
631 R., Gallaud, A., Finkel, R., Jolivet, M., Chen, Y., & Roy, P. (2011). Paleo-erosion rates
632 in Central Asia since 9Ma: A transient increase at the onset of Quaternary glaciations?
633 *Earth and Planetary Science Letters*, 304(1), 85–92.
634 <https://doi.org/10.1016/j.epsl.2011.01.018>
- 635 Chmeleff, J., von Blanckenburg, F., Kossert, K., & Jakob, D. (2010). Determination of the Be-
636 10 half-life by multicollector ICP-MS and liquid scintillation counting. *Nuclear*
637 *Instruments & Methods In Physics Research Section B-Beam Interactions With*
638 *Materials And Atoms*, 268(2), 192–199.
- 639 Clark, A. H., Tosdal, R. M., Farrar, E., & V, A. P. (1990). Geomorphologic environment and
640 age of supergene enrichment of the Cuajone, Quellaveco, and Toquepala porphyry
641 copper deposits, southeastern Peru. *Economic Geology*, 85(7), 1604–1628.
642 <https://doi.org/10.2113/gsecongeo.85.7.1604>

- 643 Cortés-Aranda J., González L. Gabriel, Binnie S. A., Robinson R., Freeman S. P. H. T., &
644 Vargas E. G. (2012). Paleoseismology of the Mejillones Fault, northern Chile: Insights
645 from cosmogenic ^{10}Be and optically stimulated luminescence determinations.
646 *Tectonics*, *31*(2). <https://doi.org/10.1029/2011TC002877>
- 647 Davis, M., Matmon, A., Placzek, C. J., McIntosh, W., Rood, D. H., & Quade, J. (2014).
648 Cosmogenic nuclides in buried sediments from the hyperarid Atacama Desert, Chile.
649 *Quaternary Geochronology*, *19*, 117–126.
650 <https://doi.org/10.1016/j.quageo.2013.06.006>
- 651 De Silva, S. L. (1989). Altiplano-Puna volcanic complex of the central Andes. *Geology*, *17*(12),
652 1102–1106.
- 653 Dunai, T. J., Lopez, G. A. G., & Juez-Larre, J. (2005). Oligocene-Miocene age of aridity in the
654 Atacama Desert revealed by exposure dating of erosion-sensitive landforms. *Geology*,
655 *33*(4), 321–324.
- 656 Dunai, Tibor J. (2010). *Cosmogenic Nuclides: Principles, concepts and applications in the*
657 *Earth surface sciences*. Cambridge University Press.
- 658 Evenstar, L. A., Mather, A. E., Hartley, A. J., Stuart, F. M., Sparks, R. S. J., & Cooper, F. J.
659 (2017). Geomorphology on geologic timescales: Evolution of the late Cenozoic Pacific
660 paleosurface in Northern Chile and Southern Peru. *Earth-Science Reviews*, *171*, 1–27.
661 <https://doi.org/10.1016/j.earscirev.2017.04.004>
- 662 Evenstar, Laura A., Hartley, A. J., Stuart, F. M., Mather, A. E., Rice, C. M., & Chong, G.
663 (2009). Multiphase development of the Atacama Planation Surface recorded by
664 cosmogenic ^3He exposure ages: Implications for uplift and Cenozoic climate change in
665 Western South America. *Geology*, *37*(1), 27–30. <https://doi.org/10.1130/G25437A.1>
- 666 Fernández-Mort, A., Riquelme, R., Alonso-Zarza, A. M., Campos, E., Bissig, T., Mpodozis,
667 C., Carretier, S., Herrera, C., Tapia, M., Pizarro, H., & Muñoz, S. (2017). A genetic
668 model based on evapoconcentration for sediment-hosted exotic-Cu mineralization in
669 arid environments: The case of the El Tesoro Central copper deposit, Atacama Desert,
670 Chile. *Mineralium Deposita*, 1–21. <https://doi.org/10.1007/s00126-017-0780-2>
- 671 Gattacceca, J., Valenzuela, M., Uehara, M., Jull, A. J. T., Giscard, M., Rochette, P., Braucher,
672 R., Suavet, C., Gounelle, M., Morata, D., Munayco, P., Bourrot-Denise, M., Bourles, D.,
673 & Demory, F. (2011). The densest meteorite collection area in hot deserts: The San Juan
674 meteorite field (Atacama Desert, Chile). *Meteoritics & Planetary Science*, *46*(9), 1276–
675 1287. <https://doi.org/10.1111/j.1945-5100.2011.01229.x>
- 676 Gosse, J. C., & Phillips, F. M. (2001). Terrestrial in situ cosmogenic nuclides: Theory and
677 application. *Quaternary Science Reviews*, *20*(14), 1475–1560.
678 [https://doi.org/10.1016/S0277-3791\(00\)00171-2](https://doi.org/10.1016/S0277-3791(00)00171-2)
- 679 Granger, D. E., Kirchner, J. W., & Finkel, R. (1996). Spatially Averaged Long-Term Erosion
680 Rates Measured from in Situ-Produced Cosmogenic Nuclides in Alluvial Sediment. *The*
681 *Journal of Geology*, *104*(3), 249–257. <https://doi.org/10.1086/629823>
- 682 Granger, D. E., & Muzikar, P. F. (2001). Dating sediment burial with in situ-produced

- 683 cosmogenic nuclides: Theory, techniques, and limitations. *Earth and Planetary Science*
684 *Letters*, 188(1–2), 269–281. [https://doi.org/10.1016/S0012-821X\(01\)00309-0](https://doi.org/10.1016/S0012-821X(01)00309-0)
- 685 Hartley, Adrian J., Chong, G., Houston, J., & Mather, A. E. (2005). 150 million years of climatic
686 stability: Evidence from the Atacama Desert, northern Chile. *Journal of the Geological*
687 *Society*, 162(3), 421–424.
- 688 Hartley, Adrian John, & Chong, G. (2002). A late Pliocene age for the Atacama Desert:
689 Implications for the desertification of Western South America. *Geology*, 30(1), 43–46.
690 [https://doi.org/10.1130/0091-7613\(2002\)030<0043:LPAFTA>2.0.CO;2](https://doi.org/10.1130/0091-7613(2002)030<0043:LPAFTA>2.0.CO;2)
- 691 Heisinger, B., Lal, D., Jull, A. J. T., Kubik, P., Ivy-Ochs, S., Knie, K., & Nolte, E. (2002).
692 Production of selected cosmogenic radionuclides by muons: 2. Capture of negative
693 muons. *Earth and Planetary Science Letters*, 200(3), 357–369.
694 [https://doi.org/10.1016/S0012-821X\(02\)00641-6](https://doi.org/10.1016/S0012-821X(02)00641-6)
- 695 Heisinger, B., Lal, D., Jull, A. J. T., Kubik, P., Ivy-Ochs, S., Neumaier, S., Knie, K., Lazarev,
696 V., & Nolte, E. (2002). Production of selected cosmogenic radionuclides by muons 1.
697 Fast muons. *Earth and Planetary Science Letters*, 200(3–4), 345–355.
698 [https://doi.org/10.1016/S0012-821X\(02\)00640-4](https://doi.org/10.1016/S0012-821X(02)00640-4)
- 699 Honda, M., Zhang, X., Phillips, D., Hamilton, D., Deerberg, M., & Schwieters, J. B. (2015).
700 Redetermination of the ^{21}Ne relative abundance of the atmosphere, using a high
701 resolution, multi-collector noble gas mass spectrometer (HELIX-MC Plus).
702 *International Journal of Mass Spectrometry*, 387, 1–7.
703 <https://doi.org/10.1016/j.ijms.2015.05.012>
- 704 Houston, J., & Hartley, A. J. (2003). The central Andean west-slope rainshadow and its
705 potential contribution to the origin of hyper-aridity in the Atacama Desert. *International*
706 *Journal of Climatology: A Journal of the Royal Meteorological Society*, 23(12), 1453–
707 1464.
- 708 Jordan, T. E., Kirk-Lawlor, N. E., Blanco, N. P., Rech, J. A., & Cosentino, N. J. (2014).
709 Landscape modification in response to repeated onset of hyperarid paleoclimate states
710 since 14 Ma, Atacama Desert, Chile. *Geological Society of America Bulletin*, 126(7–8),
711 1016–1046. <https://doi.org/10.1130/B30978.1>
- 712 Kahou, Z. S., Brichau, S., Poujol, M., Duchêne, S., Campos, E., Leisen, M., d’Abzac, F.-X.,
713 Riquelme, R., & Carretier, S. (2020). First U-Pb LA-ICP-MS in situ dating of supergene
714 copper mineralization: Case study in the Chuquicamata mining district, Atacama
715 Desert, Chile. *Mineralium Deposita*, 1–14.
- 716 Kober, F., Alfimov, V., Ivy-Ochs, S., Kubik, P. W., & Wieler, R. (2011). The cosmogenic ^{21}Ne
717 production rate in quartz evaluated on a large set of existing ^{21}Ne – ^{10}Be data. *Earth*
718 *and Planetary Science Letters*, 302(1–2), 163–171.
719 <https://doi.org/10.1016/j.epsl.2010.12.008>
- 720 Kober, F., Ivy-Ochs, S., Schlunegger, F., Baur, H., Kubik, P. W., & Wieler, R. (2007).
721 Denudation rates and a topography-driven rainfall threshold in northern Chile: Multiple
722 cosmogenic nuclide data and sediment yield budgets. *Geomorphology*, 83(1–2), 97–

- 723 120.
- 724 Kober, F., Ivy-Ochs, S., Zeilinger, G., Schlunegger, F., Kubik, P. W., Baur, H., & Wieler, R.
725 (2009). Complex multiple cosmogenic nuclide concentration and histories in the arid
726 Rio Luta catchment, northern Chile. *Earth Surface Processes And Landforms*, 34(3),
727 398–412.
- 728 Korschinek, G., Bergmaier, A., Faestermann, T., Gerstmann, U. C., Knie, K., Rugel, G.,
729 Wallner, A., Dillmann, I., Dollinger, G., & von Gostomski, Ch. L. (2010). A new value
730 for the half-life of ^{10}Be by Heavy-Ion Elastic Recoil Detection and liquid scintillation
731 counting. *Nuclear Instruments and Methods in Physics Research Section B: Beam
732 Interactions with Materials and Atoms*, 268(2), 187–191.
733 <https://doi.org/10.1016/j.nimb.2009.09.020>
- 734 Lal, D. (1991). Cosmic ray labeling of erosion surfaces: In-situ nuclide production rates and
735 erosion models. *Earth Planet. Sci. Lett.*, 104, 424–439.
- 736 Madella, A., Delunel, R., Akçar, N., Schlunegger, F., & Christl, M. (2018). ^{10}Be -inferred
737 paleo-denudation rates imply that the mid-Miocene western central Andes eroded as
738 slowly as today. *Scientific Reports*, 8(1). <https://doi.org/10.1038/s41598-018-20681-x>
- 739 MaksaeV, V., & Zentilli, M. (1999). *Fission track thermochronology of the Domeyko
740 Cordillera, northern Chile; implications for Andean tectonics and porphyry copper
741 metallogenesis.*
- 742 Marinovic, N., & Garcia, M. (n.d.). *Hoja Pampa Unión: Region de Antofagasta escala
743 1:100.000.*
- 744 Martin, L. C. P., Blard, P.-H., Balco, G., Lavé, J., Delunel, R., Lifton, N., & Laurent, V. (2017).
745 The CREp program and the ICE-D production rate calibration database: A fully
746 parameterizable and updated online tool to compute cosmic-ray exposure ages.
747 *Quaternary Geochronology*, 38, 25–49. <https://doi.org/10.1016/j.quageo.2016.11.006>
- 748 Martinod, J., Regard, V., Riquelme, R., Aguilar, G., Guillaume, B., Carretier, S., Cortés-
749 Aranda, J., Leanni, L., & Hérail, G. (2016). Pleistocene uplift, climate and
750 morphological segmentation of the Northern Chile coasts (24°S–32°S): Insights from
751 cosmogenic ^{10}Be dating of paleoshorelines. *Geomorphology*, 274, 78–91.
752 <https://doi.org/10.1016/j.geomorph.2016.09.010>
- 753 Mora, R., Artal, J., Brockway, H., Martinez, E., & Muhr, R. (2004). El Tesoro exotic copper
754 deposit, Antofagasta region, northern Chile. *Society of Economic Geologists, Special
755 Publication*, 11, 187–197.
- 756 Mortimer, C. (1973). The Cenozoic history of the southern Atacama Desert, Chile. *Journal of
757 the Geological Society*, 129(5), 505–526. <https://doi.org/10.1144/gsjgs.129.5.0505>
- 758 Mote, T. I., Becker, T. A., Renne, P., & Brimhall, G. H. (2001). Chronology of Exotic
759 Mineralization at El Salvador, Chile, by $^{40}\text{Ar}/^{39}\text{Ar}$ Dating of Copper Wad and
760 Supergene Alunite. *Economic Geology*, 96(2), 351–366.
761 <https://doi.org/10.2113/gsecongeo.96.2.351>

- 762 Mpodozis, C, Marinovic, N., Smoje, I., & Cuitiño, L. (1993). Estudio Geológico-Estructural de
763 la Cordillera de Domeyko entre Sierra Limón Verde y Sierra Mariposas, Región de
764 Antofagasta. *Servicio Nacional de Geología y Minería, Informe Registrado*, 4.
- 765 Mpodozis, Constantino, & Cornejo, P. (2012). Cenozoic Tectonics and Porphyry Copper
766 Systems of the Chilean Andes. In J. W. Hedenquist, M. Harris, & F. Camus (Eds.),
767 *Geology and Genesis of Major Copper Deposits and Districts of the World: A Tribute*
768 *to Richard H. Sillitoe* (Vol. 1–Book, Section). Society of Economic Geologists.
769 <https://doi.org/10.5382/SP.16.14>
- 770 Münchmeyer, C. (1996). Exotic deposits-products of lateral migration of supergene solutions
771 from porphyry copper deposits. *Soc. Econ. Geol. Spec. Publ.*, 5, 43–58.
- 772 Niedermann, S. (2002). Cosmic-Ray-Produced Noble Gases in Terrestrial Rocks: Dating Tools
773 for Surface Processes. *Reviews in Mineralogy and Geochemistry*, 47(1), 731–784.
774 <https://doi.org/10.2138/rmg.2002.47.16>
- 775 Nishiizumi, K., Caffee, M. W., Finkel, R. C., Brimhall, G., & Mote, T. (2005). Remnants of a
776 fossil alluvial fan landscape of Miocene age in the Atacama Desert of northern Chile
777 using cosmogenic nuclide exposure age dating. *Earth And Planetary Science Letters*,
778 237(3–4), 499–507.
- 779 Nishiizumi, K., Imamura, M., Caffee, M. W., Southon, J. R., Finkel, R. C., & McAninch, J.
780 (2007). Absolute calibration of Be-10 AMS standards. *Nuclear Instruments & Methods*
781 *In Physics Research Section B-Beam Interactions With Materials And Atoms*, 258(2),
782 403–413.
- 783 Oerter, E., Amundson, R., Heimsath, A., Jungers, M., Chong, G., & Renne, P. (2016). Early to
784 Middle Miocene climate in the Atacama Desert of Northern Chile. *Palaeogeography,*
785 *Palaeoclimatology,* *Palaeoecology*, 441, 890–900.
786 <https://doi.org/10.1016/j.palaeo.2015.10.038>
- 787 Owen, J. J., Amundson, R., Dietrich, W. E., Nishiizumi, K., Sutter, B., & Chong, G. (2011).
788 The sensitivity of hillslope bedrock erosion to precipitation. *Earth Surface Processes*
789 *and Landforms*, 36(1), 117–135. <https://doi.org/10.1002/esp.2083>
- 790 Palacios, C., Rouxel, O., Reich, M., Cameron, E. M., & Leybourne, M. I. (2011). Pleistocene
791 recycling of copper at a porphyry system, Atacama Desert, Chile: Cu isotope evidence.
792 *Mineralium Deposita*, 46(1), 1–7. <https://doi.org/10.1007/s00126-010-0315-6>
- 793 Paskoff, R. (1977). The Quaternary of Chile: The state of research. *Quaternary Research*, 8, 2–
794 31.
- 795 Perello, J., Muhr, R., Mora, R., Martinez, E., Brockway, H., Swaneck, T., Artal, J., Mpodozis,
796 C., Münchmeyer, C., & Clifford, J. (2010). Wealth creation through exploration in a
797 mature terrain: The case history of the Centinela district, northern Chile porphyry
798 copper belt. *The Challenge of Finding New Mineral Resources: Global Metallogeny,*
799 *Innovative Exploration, and New Discoveries*, 229–252.
- 800 Pizarro, H., Rousse, S., Riquelme, R., Veloso, E., Campos, E., González, R., Bissig, T.,
801 Carretier, S., Fernández-Mort, A., & Muñoz, S. (2018). The origin of the magnetic

- 802 record in Eocene-Miocene coarse-grained sediments deposited in hyper-arid/arid
803 conditions: Examples from the Atacama Desert. *Palaeogeography, Palaeoclimatology,*
804 *Palaeoecology*. <https://doi.org/10.1016/j.palaeo.2018.12.009>
- 805 Placzek, C., Granger, D. E., Matmon, A., Quade, J., & Ryb, U. (2014). Geomorphic process
806 rates in the central Atacama Desert, Chile: Insights from cosmogenic nuclides and
807 implications for the onset of hyperaridity. *American Journal of Science*, *314*, 1462–
808 1512. <http://dx.doi.org/10.2475/10.2014.03>
- 809 Quang, C. X., Clark, A. H., Lee, J. K. W., & Hawkes, N. (2005). Response of Supergene
810 Processes to Episodic Cenozoic Uplift, Pediment Erosion, and Ignimbrite Eruption in
811 the Porphyry Copper Province of Southern Perú. *Economic Geology*, *100*(1), 87–114.
812 <https://doi.org/10.2113/100.1.0087>
- 813 Rech, J. A., Currie, B. S., Michalski, G., & Cowan, A. M. (2006). Neogene climate change and
814 uplift in the Atacama Desert, Chile. *Geology*, *34*(9), 761–764.
815 <https://doi.org/10.1130/G22444.1>
- 816 Rech, J. A., Currie, B. S., Shullenberger, E. D., Dunagan, S. P., Jordan, T. E., Blanco, N.,
817 Tomlinson, A. J., Rowe, H. D., & Houston, J. (2010). Evidence for the development of
818 the Andean rain shadow from a Neogene isotopic record in the Atacama Desert, Chile.
819 *Earth and Planetary Science Letters*, *292*(3), 371–382.
820 <https://doi.org/10.1016/j.epsl.2010.02.004>
- 821 Reich, M., Palacios, C., Vargas, G., Luo, S., Cameron, E. M., Leybourne, M. I., Parada, M. A.,
822 Zúñiga, A., & You, C.-F. (2009). Supergene enrichment of copper deposits since the
823 onset of modern hyperaridity in the Atacama Desert, Chile. *Mineralium Deposita*, *44*(5),
824 497. <https://doi.org/10.1007/s00126-009-0229-3>
- 825 Reich, M., & Vasconcelos, P. M. (2015). Geological and Economic Significance of Supergene
826 Metal Deposits. *Elements*, *11*(5), 305–310. <https://doi.org/10.2113/gselements.11.5.305>
- 827 Riquelme, R., Martinod, J., Herail, G., Darrozes, J., & Charrier, R. (2003). A geomorphological
828 approach to determining the Neogene to Recent tectonic deformation in the Coastal
829 Cordillera of northern Chile (Atacama). *Tectonophysics*, *361*(3–4), 255.
- 830 Riquelme, Rodrigo, Tapia, M., Campos, E., Mpodozis, C., Carretier, S., González, R., Muñoz,
831 S., Fernández-Mort, A., Sanchez, C., & Marquardt, C. (2018). Supergene and exotic Cu
832 mineralization occur during periods of landscape stability in the Centinela Mining
833 District, Atacama Desert. *Basin Research*, *30*(3), 395–425.
834 <https://doi.org/10.1111/bre.12258>
- 835 Ritter, B., Binnie, S. A., Stuart, F. M., Wennrich, V., & Dunai, T. J. (2018). Evidence for
836 multiple Plio-Pleistocene lake episodes in the hyperarid Atacama Desert. *Quaternary*
837 *Geochronology*, *44*, 1–12. <https://doi.org/10.1016/j.quageo.2017.11.002>
- 838 Ritter, B., Stuart, F. M., Binnie, S. A., Gerdes, A., Wennrich, V., & Dunai, T. J. (2018).
839 Neogene fluvial landscape evolution in the hyperarid core of the Atacama Desert.
840 *Scientific Reports*, *8*(1), 13952. <https://doi.org/10.1038/s41598-018-32339-9>
- 841 Sanchez, C., Brichau, S., Riquelme, R., Carretier, S., Bissig, T., Lopez, C., Mpodozis, C.,

- 842 Campos, E., Regard, V., Hérail, G., & Marquardt, C. (2018). Exhumation history and
843 timing of supergene copper mineralisation in an arid climate: New thermochronological
844 data from the Centinela District, Atacama, Chile. *Terra Nova*, *30*(1), 78–85.
845 <https://doi.org/10.1111/ter.12311>
- 846 Sartégou, A., Bourlès, D. L., Blard, P.-H., Braucher, R., Tibari, B., Zimmermann, L., Leanni,
847 L., Aumaître, G., & Keddadouche, K. (2018). Deciphering landscape evolution with
848 karstic networks: A Pyrenean case study. *Quaternary Geochronology*, *43*, 12–29.
849 <https://doi.org/10.1016/j.quageo.2017.09.005>
- 850 Sillitoe, R.H., & McKee, E. H. (1996). Age of Supergene oxidation and enrichment in the
851 Chilean porphyry copper province. *Economic Geology*, *91*(1), 16.
- 852 Sillitoe, Richard H. (2010). Porphyry copper systems. *Economic Geology*, *105*(1), 3–41.
- 853 Silva, S. L. de. (1989). Altiplano-Puna volcanic complex of the central Andes. *Geology*, *17*(12),
854 1102–1106. [https://doi.org/10.1130/0091-7613\(1989\)017<1102:APVCOT>2.3.CO;2](https://doi.org/10.1130/0091-7613(1989)017<1102:APVCOT>2.3.CO;2)
- 855 Strudley, M. W., & Murray, A. B. (2007). Sensitivity analysis of pediment development
856 through numerical simulation and selected geospatial query. *Geomorphology*, *88*(3),
857 329–351. <https://doi.org/10.1016/j.geomorph.2006.12.008>
- 858 Suarez, M., & Bell, C. M. (1987). Upper Triassic to Lower Cretaceous continental and coastal
859 saline lake evaporites in the Atacama region of northern Chile. *Geological Magazine*,
860 *124*(5), 467–475.
- 861 Tapia, M., Riquelme, R., Marquardt, C., Mpodozis, C., & Mora, R. (2012). Estratigrafía y
862 sedimentología de la Cuenca El Tesoro, Distrito Centinela (región de Antofagasta) y su
863 relación con la mineralización exótica de cobre. *XIII Congreso Geológico Chile*,
864 *Antofagasta*.
- 865 Team, R. C. (2015). R Foundation for Statistical Computing; Vienna, Austria: 2014. *R: A*
866 *Language and Environment for Statistical Computing*, 2013.
- 867 Tomlinson, A. J., & Blanco, N. (1997). Structural evolution and displacement history of the
868 West Fault System, Cordillera, Chile: Part 2, postmineral history. *Congreso*
869 *Geológico Chileno*, *8*, 1878–1882.
- 870 Val, P., & Hoke, G. D. (2016). A practical tool for examining paleoerosion rates from
871 sedimentary deposits using cosmogenic radionuclides: Examples from hypothetical
872 scenarios and data. *Geochemistry, Geophysics, Geosystems*, *17*(12), 5078–5088.
- 873 Vermeesch, P., Balco, G., Blard, P.-H., Dunai, T. J., Kober, F., Niedermann, S., Shuster, D. L.,
874 Strasky, S., Stuart, F. M., & Wieler, R. (2015). Interlaboratory comparison of
875 cosmogenic ^{21}Ne in quartz. *Quaternary Geochronology*, *26*, 20–28.
- 876 Wang, F., Michalski, G., Seo, J.-H., Granger, D. E., Lifton, N., & Caffee, M. (2015). Beryllium-
877 ^{10}Be concentrations in the hyper-arid soils in the Atacama Desert, Chile: Implications for
878 arid soil formation rates and El Niño driven changes in Pliocene precipitation.
879 *Geochimica et Cosmochimica Acta*, *160*, 227–242.
880 <https://doi.org/10.1016/j.gca.2015.03.008>

881 Zimmermann, L., Blard, P. H., Burnard, P., Medynski, S., Pik, R., & Puchol, N. (2012). A new
 882 single vacuum furnace design for cosmogenic ^3He dating. *Geostandards and*
 883 *Geoanalytical Research*, 36(2), 121–129.

884 7 Tables

885 **Table 1.** Cosmogenic production schemes, derived from Granger and Muzikar (2001, GR), Braucher et
 886 al. (2011, BH and BR), Heisinger et al. (2002; 2002, labelled H and for Neon production in GR, BR, HS).
 887 ^{10}Be production SLHL is set to 4.15 at/g/a (Martin et al., 2017), and the $^{21}\text{Ne}/^{10}\text{Be}$ ratio is 4.12 (Balco
 888 and Shuster 2009a; Kober et al. 2011).

			GH	BH	HS	BR
	Spallation	Λ , Attenuation coefficient (kg/m^2)		1600		
Beryllium-10		Λ , Attenuation coefficients (kg/m^2)	7380 / 26880 / 43600	15000 / 43200	H	15000 / 43200
	Muons	Surface production ratio (%)	1.8 / 0.4 / 0.4	0.15 / 0.51	0.28/0.92	0.15 / 0.51
		^{21}Ne to ^{10}Be spallation production ratio		4.12		
Neon-21		Λ , Attenuation coefficients (kg/m^2)		H		Idem ^{10}Be
	Muons	Surface production ratio (%)		0 / 3.6		

889

890

891

892

893 **Table 2.** ^{10}Be concentrations. † denote a sample entirely processed at CEREGE. Final uncertainty is
 894 corrected for process blank, AMS standard and AMS systematic error.

Sample	Mass Quartz g	Carrier ^9Be at	$\text{N } ^{10}\text{Be}$	Measured $^{10}\text{Be}/^9\text{Be}$	uncertainty measure+blank %	$[^{10}\text{Be}]$ at/g	+/-
Process blank							
All samples except MIR-10		2.39E+19	38	4.73E-15	16.29%		
MIR-10 only		2.04E+19	41	5.41E-15	15.66%		
EI Tesoro							
ET-01	67.35	2.39E+19	15	2.67E-14	25.86%	7817	2021
ET-02	62.13	2.41E+19	14	2.44E-14	31.75%	7630	2423
ET-03	66.51	2.39E+19	18	1.87E-14	29.98%	5030	1508
ET-04	68.28	2.40E+19	15	1.44E-14	26.70%	3378	902
ET-05	59.82	2.41E+19	54	2.28E-14	14.45%	7288	1053
ET-06	6.19	2.37E+19	46	5.87E-15	26.77%	4337	1161
ET-07	13.31	2.38E+19	67	6.45E-15	12.30%	3059	376
ET-08	57.76	2.41E+19	28	8.98E-15	18.95%	1774	336
ET-09	19.66	2.38E+19	44	7.46E-15	15.50%	3298	511
AMS blank ET			4	4.75E-16			
EI Mirador							
MIR-01	12.35	2.38E+19	327	4.00E-14	5.71%	68021	3887
MIR-04	2.79	2.38E+19	1202	8.17E-14	3.26%	657012	21426
MIR-05	3.70	2.38E+19	1176	1.56E-13	3.32%	969755	32215
MIR-11	3.60	2.39E+19	30	5.50E-15	18.31%	5133	940
AMS blank MIR, except MIR-10			3	4.23E-16			
MIR-10†	15.40	2.04E+19	71	8.67E-15	15.03%	4320	2151
AMS blank MIR-10			5	5.52E-16			

† sample prepared and measured at CEREGE

Final uncertainty is corrected for process blank.

895

896

897

898

899 **Table 3.** ^{21}Ne concentrations (cf. Supporting Information)

Sample	Mass Quartz mg	Extraction temperature (°C)	^{20}Ne [^{20}Ne] 10^3 at/g	+/- (1 σ)	$^{21}\text{Ne}/^{20}\text{Ne}$	+/- (1 σ)	$^{22}\text{Ne}/^{20}\text{Ne}$	+/- (1 σ)	Computed cosmogenic [^{21}Ne] 10^6 at/g	+/- (1 σ)	Computed cosmogenic [^{21}Ne] 10^6 at/g	+/- (1 σ)
El Tesoro												
ET-01	173.6	600	3.3	0.1	0.00274	0.00010	0.10095	0.00289	< DL		< DL	
	173.6	1400	51.7	0.6	0.00288	0.00008	0.10130	0.00248	< DL		< DL	
ET-02	149.8	600	7.6	0.2	0.00314	0.00008	0.10201	0.00224	1.8	0.8	8.8	5.8
	149.8	1400	61	0.6	0.00302	0.00008	0.10055	0.00245	7	5		
ET-03	147.7	1400	41	0.5	0.00309	0.00010	0.10191	0.00305			8	4
ET-04	185.5	1400	36.1	0.5	0.00629	0.00017	0.10181	0.00287			123	7
ET-05	156.5	1400	32	0.5	0.00316	0.00012	0.10158	0.00343			8	4
ET-06	105.6	1400	7.1	0.4	0.00386	0.00071	0.10560	0.01955			7	5
ET-07	185.6	1400	31	0.5	0.00317	0.00011	0.10155	0.00313			8	4
ET-08	195.4	1400	37	0.5	0.00307	0.00009	0.10070	0.00273			6	4
ET-09	211.8	1400	44.5	0.6	0.00296	0.00008	0.10115	0.00243			< DL	
El Mirador												
MIR-01	215.1	1400	2.8	0.4	0.00638	0.00122	0.10303	0.02390			10	4
MIR-04	155.1	1400	5.1	0.4	0.02602	0.00335	0.12506	0.02047			118	20
MIR-05	145.9	600	0.1	0.1	0.00845	0.00298	0.08614	0.06122	0.7	0.6	137.7	8.6
	145.9	1400	38.4	0.5	0.00645	0.00019	0.10512	0.00327	137	8		
MIR-10	162.3	600	3	0.1	0.00297	0.00010	0.09969	0.00314	< DL		21.4	5.5
	162.3	1400	59.3	0.7	0.00326	0.00008	0.10177	0.00247	21.4	5.5		
MIR-11	79.8	1400	4.3	0.1	0.00274	0.00013	0.09973	0.00402			< DL	

901

902

903

904

905 **Table 4.** $^{21}\text{Ne}/^{10}\text{Be}$ burial duration (i.e., minimum deposition time, cf. text).

Sample	Depth (m)	^{10}Be concentration		^{21}Ne conc. $\times 10^6$		$^{21}\text{Ne}/^{10}\text{Be}$	Burial time (source elev =2500m)		Burial time (source elev =4000m)		Minimum erosion and sedimentation rate m/myr
		at/g	+/-	at/g	+/-		Ma	+/-	Ma	+/-	
ET-01	57	7985	3273	<DL							
ET-02	59	7815	3968	8.80	5.80	1126	11.2	1.5	11.2	1.5	21.7
ET-03	63	5201	2619	8	4	1538	11.8	1.4	11.8	1.5	19.0
ET-04	84	3545	1713	123	7	34699	16.9	1	17.5	1	1.0
ET-05	105	7479	1786	8	4	1070	11.0	1.1	11.1	1.1	15.3
ET-06	106	6156	7116	7	5	1137	11.2	2	11.2	2.1	17.1
ET-07	108	3907	1899	8	4	2048	12.3	1.4	12.4	1.5	16.7
ET-08	111	1973	892	6	4	3042	13.2	1.6	13.2	1.6	22.3
ET-09	115	3873	1790	<DL							
MIR-01	18	68021	6209	10	4	147	7.0	0.8	7.1	0.8	11.9
MIR-04	13	657012	32335	118	20	180	6.4	0.2	7.0	0.3	1.0
MIR-05	12	969755	46786	137.70	8.60	142	5.8	0.1	6.4	0.1	0.9
MIR-11	45	4320	2057	21.40	5.50	4954	13.9	1.1	14.1	1.1	7.1
MIR-10	63	5133	8383	<DL							

907

908

909

910 **Table 5.** Summary of information on sedimentation and denudation rates inferred from the analysis
 911 presented in this work.

Time period	Sedimentation rate (m/My)	Source denudation rate (m/My)
Present	<2	<1
7 Ma - present	<2	<10
9.5 - 7 Ma	<2	>50
x - 9.5Ma	>100	>250
Deposition of the copper rich layer. Ends sometime between 10 and 14 Ma (= x)		
	0.5-5	>250

912

913

914 8 Figures

915 Figure 1: Onset of (hyper)aridity in the Atacama Desert. A. Map of the Atacama Desert *in northern Chile*
 916 *with study site locations and data type; the colors refer to the main morphostructural domain (CC : Coastal Cordillera, CD :*
 917 *Central Depression, PC : Precordillera, AS : Atacama Salar, WC : Western Cordillera). The red rectangle represents the Centinela*
 918 *District position. B. Review of the aridity and hyperaridity onset timing inferred from various methods (method indicated in*
 919 *square in B.); light grey for aridity and dark grey for hyperaridity.*

920

921 Figure 2 A. Location of the Centinela District via an oblique view of northern Chile in Google Earth. B.
 922 Geological map modified after Riquelme et al. (2018) 1. Post-mid-Miocene poorly consolidated gravel
 923 deposits constituting the alluvial fans observed on the landscape surface; 2. Eocene mineralized
 924 porphyry intrusions (45-39 Ma) 3. Upper Cretaceous sedimentary and volcanic rocks. 4. Cretaceous
 925 and Paleocene intrusions. 5. Jurassic calcareous rocks. 6. Upper Paleozoic and Triassic basement. E.
 926 Esperanza gravels. I, TII and TIII. Tesoro I, II and TIII gravels, respectively. At. Atravesado gravels. Ar.
 927 Arrieros gravels. A-A' shows the location of the structural profile C.

928

929 Figure 3: Quantification of the erosion (denudation) rates in the northern Chilean Atacama Desert (18-30°S) over
 930 decades shown in red (suspended sediment gauging), over millennia shown in blue or green (cosmogenic
 931 isotopes to measure either local or catchment-averaged denudation rates) or over million years shown in purple
 932 (incision of geological surfaces) (extracted from the database of Carretier et al., 2018). The box width reflects the
 933 number of data (indicated inside or under the box).

934

935 Figure 4: Aerial views of the Tesoro Central and Mirador open-pit mines (A. and B., respectively) with
 936 sampling paths. 1. View of part of the Tesoro Central sampling path focused on the exotic-Cu ore
 937 deposit layer (highlighted in turquoise) with sample locations (for the entire column sampling refer to
 938 Figure 5). 2. View of the Mirador open-pit mine sampling path with the contact between the gravels
 939 and Cu-Supergene deposit and sample locations.

940

941 Figure 5: Sedimentary columns of the Tesoro Central and Mirador open-pit mines (adapted from
 942 Fernández-Mort et al., 2017) with the sampling depths, gravel formation names and sedimentary
 943 details. The 9.52 ± 0.02 Ma age for the Artola ignimbrite has been measured by Riquelme et al. (2018).

944

945 Figure 6: The conceptual model upon which the inversion is designed. There are two independent steps
 946 in the clast history. First, they erode upstream and are transported toward the sedimentary basin (box
 947 1 of the inversion program) and, second, they are covered by sediments during the basin infilling (box
 948 2 of the inversion program).

949

950 Figure 7: Bipyramid automorph quartz found in MIR13-01 reworked from 9.5 Ma-old ignimbrite
 951 (Riquelme et al. 2018)

952

953 Figure 8. Production vs. depth (log scale) for the different schemes (left: ^{10}Be ; right: ^{21}Ne). The different
 954 colored lines represent the different production rate schemes tested: GH, BH, HS and BR (see Table 1
 955 for further details).

956

957 Figure 9: Reference inversion for the El Tesoro mining pit (BR). (A) The color corresponds to the χ^2
 958 value: light yellow to brown, where a darker color is a better fit; the grey areas correspond to the
 959 tested scenario leading to improbable χ^2 values. The sample positions correspond to the ticks on the
 960 left; the copper layer is highlighted in turquoise. The inversion is constrained at three positions:
 961 arbitrary initial ($t = 20$ Ma, $z = -160$ m), ignimbrite layer ($t = 9.5 \pm 0.3$ Ma, $z = -10$ m) and surface ($t = 0$, z
 962 $= 0$). (B) Explanations of how to read this graph.

963

964 Figure 10. Cosmogenic isotope concentration (reference inversion) according to depth (Tesoro
 965 Central), A. for ^{10}Be and B. for ^{21}Ne . For both figures, the light colors correspond to every Monte Carlo
 966 scenario tested; the bold lines represent the best χ^2 scenario for ^{10}Be only, ^{21}Ne only and for both
 967 nuclides in blue, red and black, respectively. The circles and associated horizontal lines indicate the
 968 measured concentrations and their related uncertainties.

969

970 Figure 11. Best χ^2 for El Tesoro in function of the source area denudation rate for the period older than
 971 9.5 Ma, for various production schemes for both nuclides (^{10}Be and ^{21}Ne , logarithmic χ^2 -scale). The
 972 points indicate the best χ^2 from the inversions, the trend is drawn as lines.

973

974 Figure 12. χ^2 for the El Mirador pit (without MIR-01, which derives from an ignimbrite) in function of
 975 the source area denudation rate for the period younger than 9.5 Ma, for various production schemes
 976 for either ^{10}Be (top, linear χ^2 -scale) or ^{21}Ne and ^{10}Be data (bottom, logarithmic χ^2 -scale). The latter
 977 shows that low values are reached for denudation rates higher than ~ 40 m/Ma.

978

979 Figure 13. Back-scarp retreat model. It is possible that the basins were roughly located at the location
 980 of a scarp ~ 12 Ma ago, with the rapidly eroding scarp ($\epsilon > 250$ m/Ma) as the main source of sediment.

981 Subsequently, the back-scarp gradually retreated to the present, with an intermediate period marked
982 by intermediate denudation rates and the Artola ignimbrite deposition at 9.5 Ma BP. The current state
983 is characterized by low denudation rates (< 10 m/Ma).

984

985 **9 Data Sharing and Data Accessibility**

986 The data that support the findings of this study are found in the core of the paper, except the code
987 IMIS, openly available in GitHub at <https://github.com/regard-vincent/IMIS>.

			GH	BH	HS	BR
	Spallation	Λ , Attenuation coefficient (kg/m ²)		1600		
Beryllium-10		Λ , Attenuation coefficients (kg/m ²)	7380 / 26880 / 43600	15000 / 43200	H	15000 / 43200
	Muons	Surface production ratio (%)	1.8 / 0.4 / 0.4	0.15 / 0.51	0.28/0.92	0.15 / 0.51
		²¹ Ne to ¹⁰ Be spallation production ratio		4.12		
Neon-21		Λ , Attenuation coefficients (kg/m ²)		H		Idem ¹⁰ Be
	Muons	Surface production ratio (%)		0 / 3.6		

Sample	Mass Quartz g	Carrier ⁹ Be at	N ¹⁰ Be	Measured ¹⁰ Be/ ⁹ Be	uncertainty measure+blank %	[¹⁰ Be] at/g	+/-
Process blank							
All samples except MIR-10		2.39E+19	38	4.73E-15	16.29%		
MIR-10 only		2.04E+19	41	5.41E-15	15.66%		
EI Tesoro							
ET-01	67.35	2.39E+19	15	2.67E-14	25.86%	7817	2021
ET-02	62.13	2.41E+19	14	2.44E-14	31.75%	7630	2423
ET-03	66.51	2.39E+19	18	1.87E-14	29.98%	5030	1508
ET-04	68.28	2.40E+19	15	1.44E-14	26.70%	3378	902
ET-05	59.82	2.41E+19	54	2.28E-14	14.45%	7288	1053
ET-06	6.19	2.37E+19	46	5.87E-15	26.77%	4337	1161
ET-07	13.31	2.38E+19	67	6.45E-15	12.30%	3059	376
ET-08	57.76	2.41E+19	28	8.98E-15	18.95%	1774	336
ET-09	19.66	2.38E+19	44	7.46E-15	15.50%	3298	511
AMS blank ET			4	4.75E-16			
EI Mirador							
MIR-01	12.35	2.38E+19	327	4.00E-14	5.71%	68021	3887
MIR-04	2.79	2.38E+19	1202	8.17E-14	3.26%	657012	21426
MIR-05	3.70	2.38E+19	1176	1.56E-13	3.32%	969755	32215
MIR-11	3.60	2.39E+19	30	5.50E-15	18.31%	5133	940
AMS blank MIR, except MIR-10			3	4.23E-16			
MIR-10†	15.40	2.04E+19	71	8.67E-15	15.03%	4320	2151
AMS blank MIR-10			5	5.52E-16			

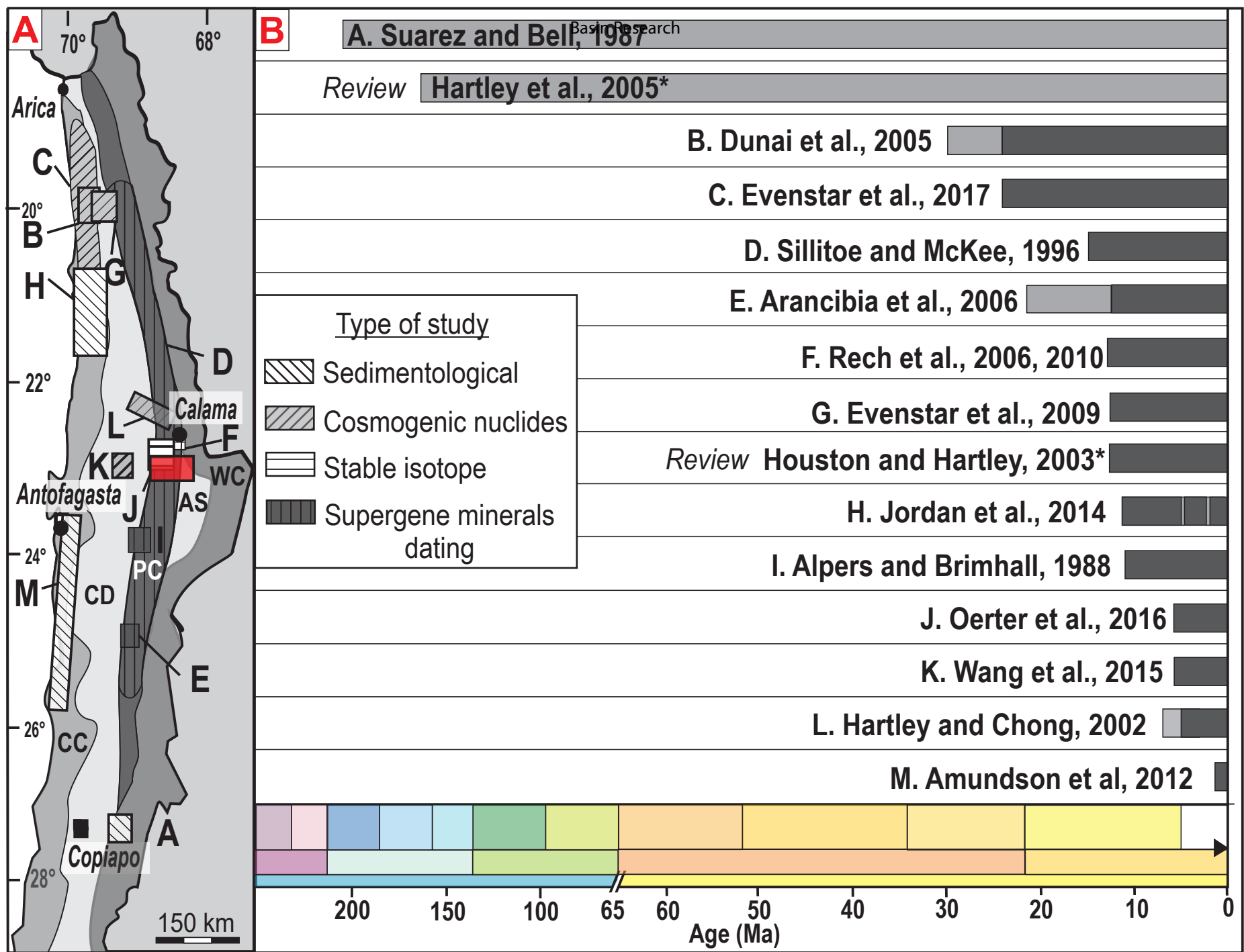
† sample prepared and measured at CEREGE

Final uncertainty is corrected for process blank.

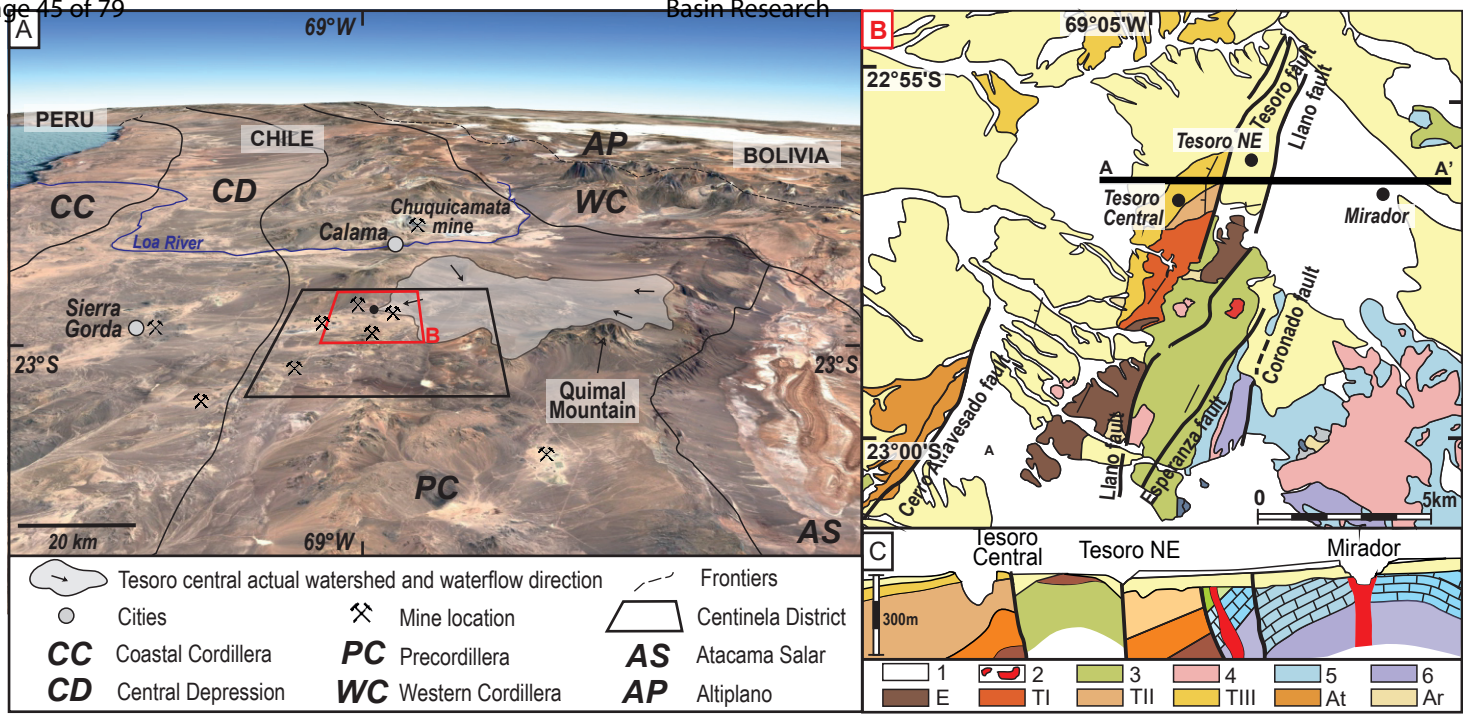
Sample	Mass Quartz mg	Extraction temperature (°C)	[²⁰ Ne] 10 ⁹ at/g	+/- (1σ)	²¹ Ne/ ²⁰ Ne	+/- (1σ)	²² Ne/ ²⁰ Ne	+/- (1σ)	Computed cosmogenic [²¹ Ne] 10 ⁶ at/g	+/- (1σ)	Computed cosmogenic [²¹ Ne] 10 ⁶ at/g	+/- (1σ)
EI Tesoro												
ET-01	173.6	600	3.3	0.1	0.00274	0.00010	0.10095	0.00289	< DL		< DL	
	173.6	1400	51.7	0.6	0.00288	0.00008	0.10130	0.00248	< DL		< DL	
ET-02	149.8	600	7.6	0.2	0.00314	0.00008	0.10201	0.00224	1.8	0.8	8.8	5.8
	149.8	1400	61	0.6	0.00302	0.00008	0.10055	0.00245	7	5		
ET-03	147.7	1400	41	0.5	0.00309	0.00010	0.10191	0.00305			8	4
ET-04	185.5	1400	36.1	0.5	0.00629	0.00017	0.10181	0.00287			123	7
ET-05	156.5	1400	32	0.5	0.00316	0.00012	0.10158	0.00343			8	4
ET-06	105.6	1400	7.1	0.4	0.00386	0.00071	0.10560	0.01955			7	5
ET-07	185.6	1400	31	0.5	0.00317	0.00011	0.10155	0.00313			8	4
ET-08	195.4	1400	37	0.5	0.00307	0.00009	0.10070	0.00273			6	4
ET-09	211.8	1400	44.5	0.6	0.00296	0.00008	0.10115	0.00243			< DL	
EI Mirador												
MIR-01	215.1	1400	2.8	0.4	0.00638	0.00122	0.10303	0.02390			10	4
MIR-04	155.1	1400	5.1	0.4	0.02602	0.00335	0.12506	0.02047			118	20
MIR-05	145.9	600	0.1	0.1	0.00845	0.00298	0.08614	0.06122	0.7	0.6	137.7	8.6
	145.9	1400	38.4	0.5	0.00645	0.00019	0.10512	0.00327	137	8		
MIR-10	162.3	600	3	0.1	0.00297	0.00010	0.09969	0.00314	< DL		21.4	5.5
	162.3	1400	59.3	0.7	0.00326	0.00008	0.10177	0.00247	21.4	5.5		
MIR-11	79.8	1400	4.3	0.1	0.00274	0.00013	0.09973	0.00402			< DL	

Sample	Depth (m)	¹⁰ Be concentration		²¹ Ne conc. x10 ⁶		²¹ Ne/ ¹⁰ Be	Burial time (source elev =2500m)		Burial time (source elev =4000m)		Minimum erosion and sedimentation rate m/myr
		at/g	+/-	at/g	+/-		Ma	+/-	Ma	+/-	
ET-01	57	7985	3273	<DL							
ET-02	59	7815	3968	8.80	5.80	1126	11.2	1.5	11.2	1.5	21.7
ET-03	63	5201	2619	8	4	1538	11.8	1.4	11.8	1.5	19.0
ET-04	84	3545	1713	123	7	34699	16.9	1	17.5	1	1.0
ET-05	105	7479	1786	8	4	1070	11.0	1.1	11.1	1.1	15.3
ET-06	106	6156	7116	7	5	1137	11.2	2	11.2	2.1	17.1
ET-07	108	3907	1899	8	4	2048	12.3	1.4	12.4	1.5	16.7
ET-08	111	1973	892	6	4	3042	13.2	1.6	13.2	1.6	22.3
ET-09	115	3873	1790	<DL							
MIR-01	18	68021	6209	10	4	147	7.0	0.8	7.1	0.8	11.9
MIR-04	13	657012	32335	118	20	180	6.4	0.2	7.0	0.3	1.0
MIR-05	12	969755	46786	137.70	8.60	142	5.8	0.1	6.4	0.1	0.9
MIR-11	45	4320	2057	21.40	5.50	4954	13.9	1.1	14.1	1.1	7.1
MIR-10	63	5133	8383	<DL							

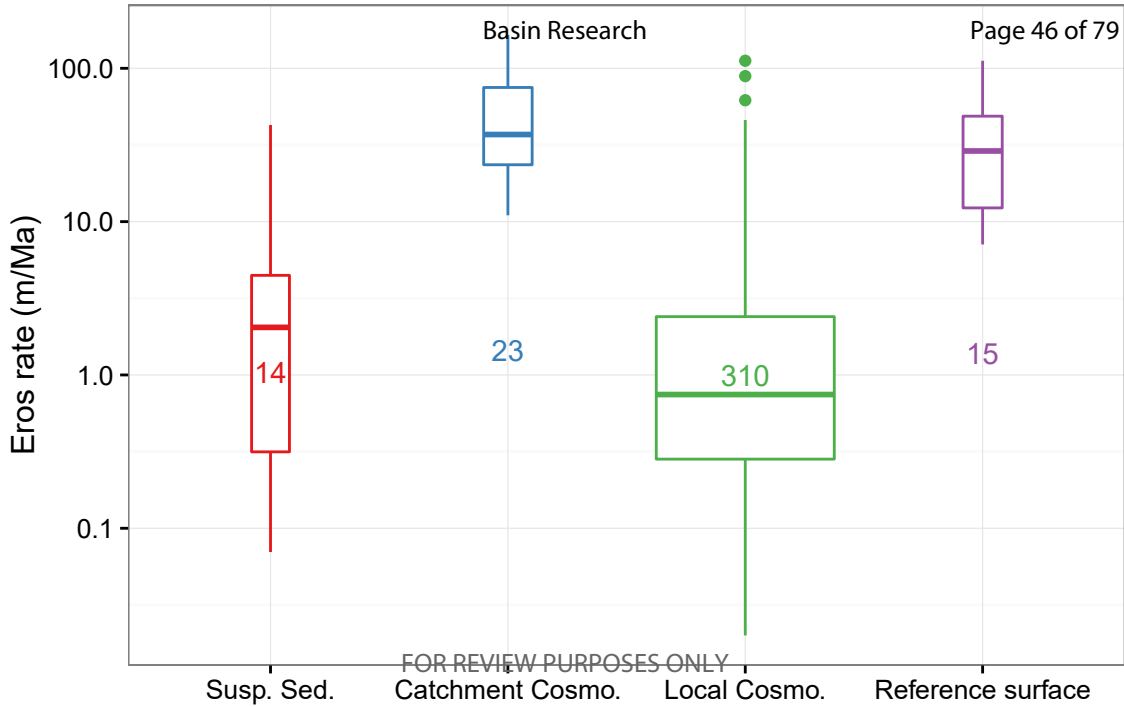
Time period	Sedimentation rate (m/My)	Source denudation rate (m/My)
Present	<2	<1
7 Ma - present	<2	<10
9.5 - 7 Ma	<2	>50
x - 9.5Ma	>100	>250
Deposition of the copper rich layer. Ends sometime between 10 and 14 Ma		
(= x)	0.5-5	>250



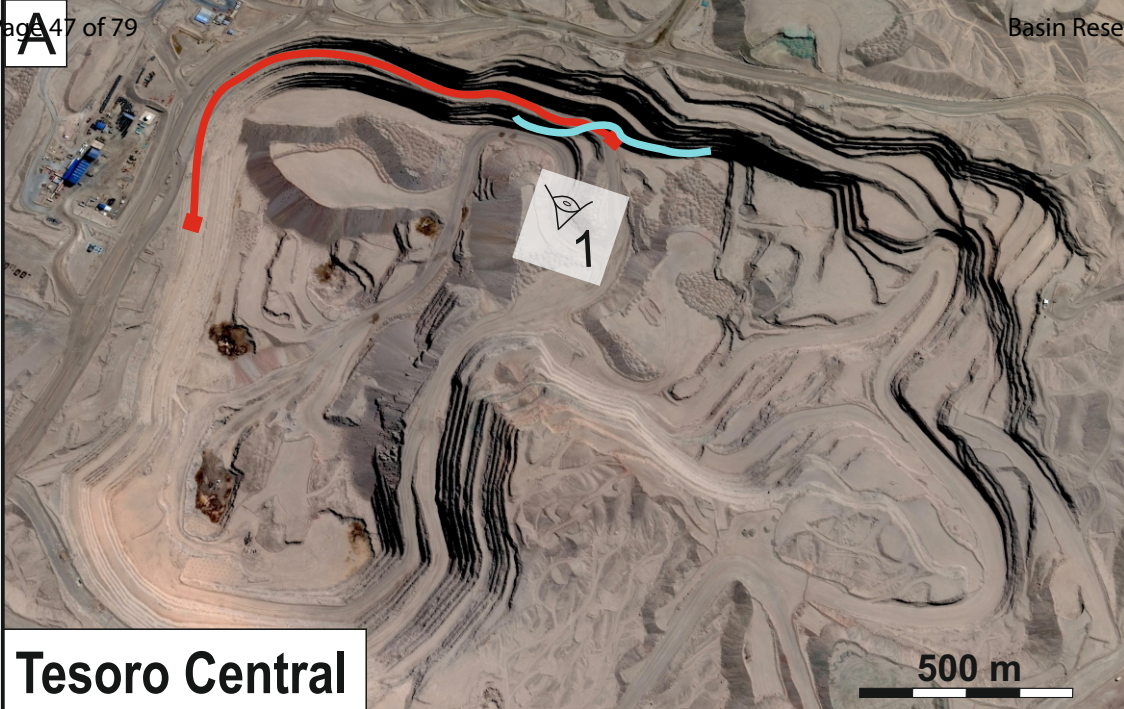
Sanchez et al. Fig 1



Sanchez et al. Figure 2



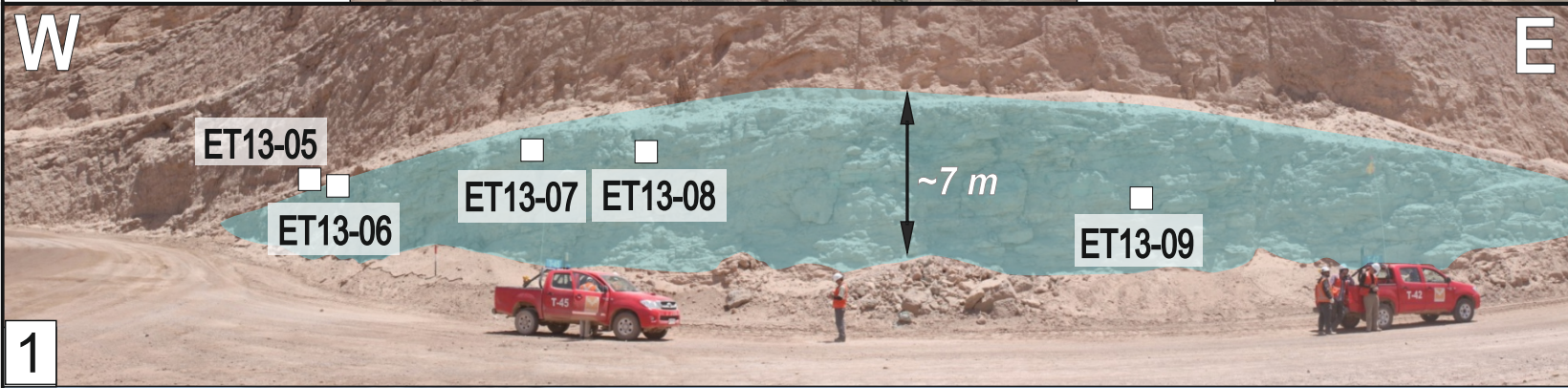
Sanchez et al. Figure 3



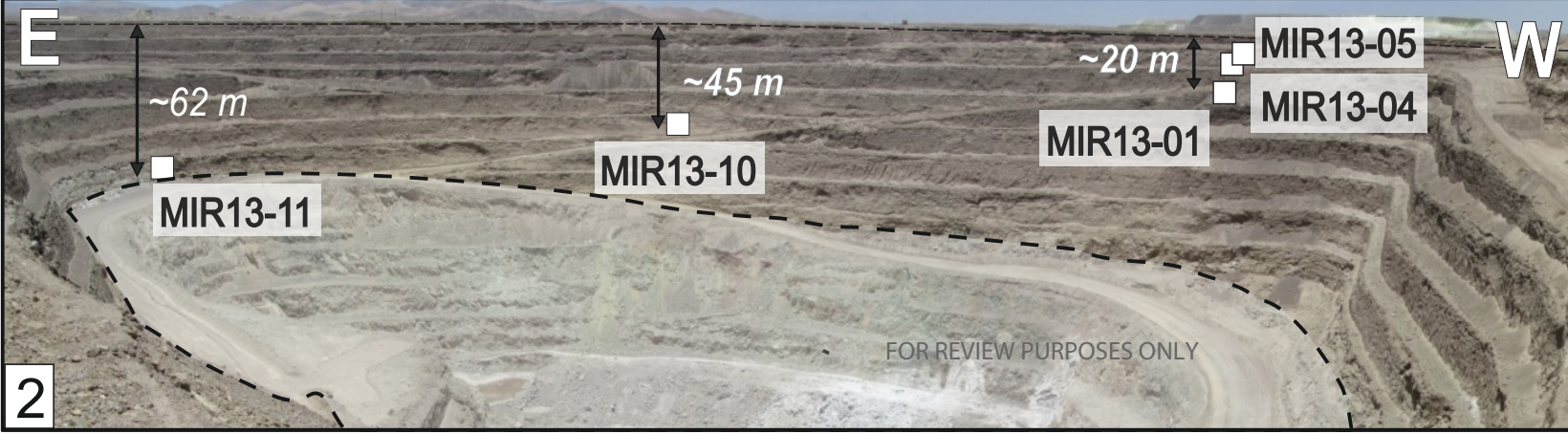
Tesoro Central



Mirador









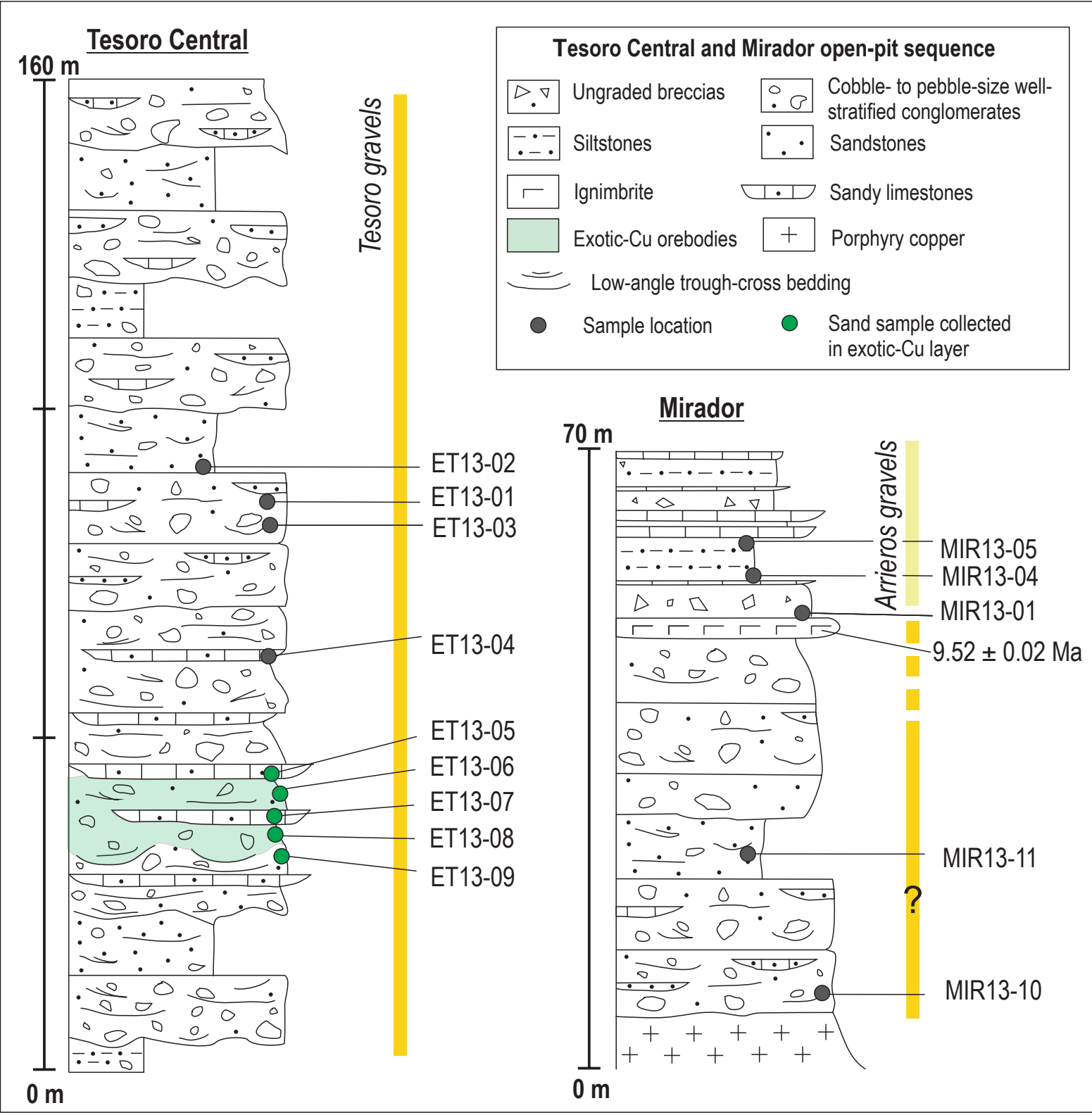
1



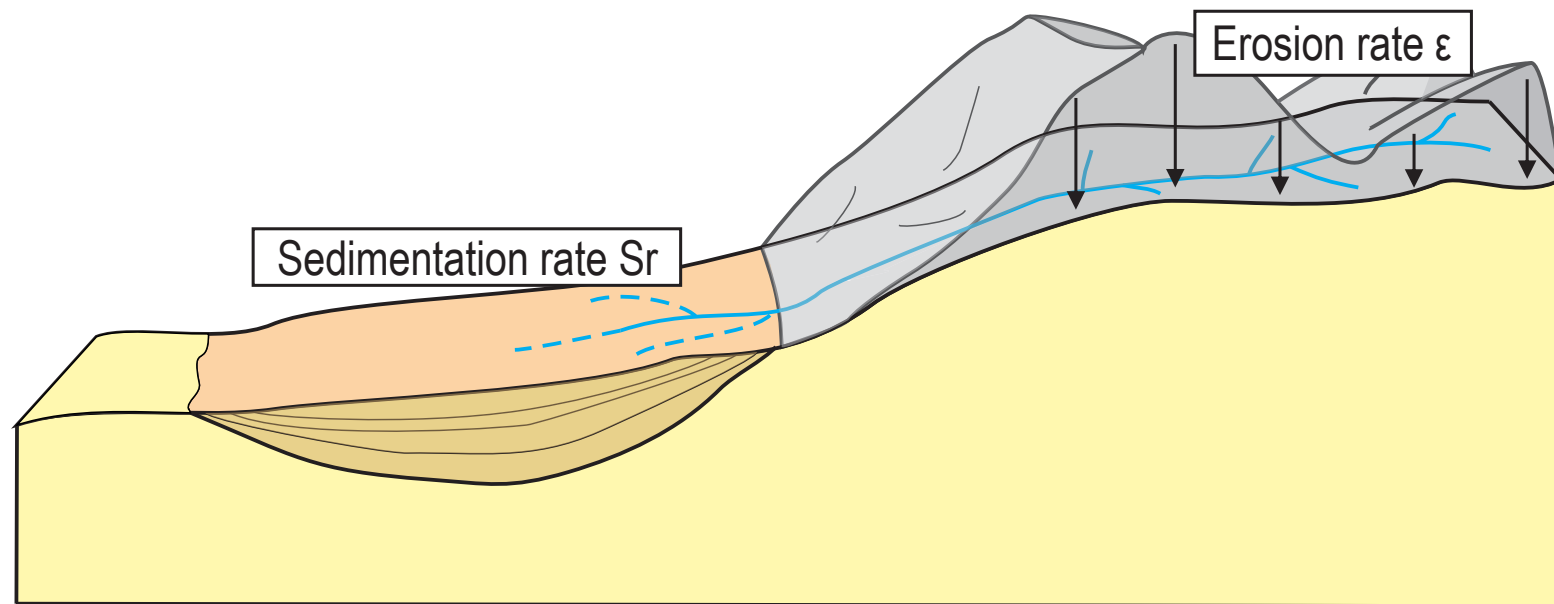
2

Legend

-  Sampling path
-  Exotic-Cu ore deposit enriched layer
-  Picture views
-  Exotic-Cu ore deposit
-  Contact between gravels and Cu supergene deposit
-  Samples
- ET13-05** Sample names



Sanchez et al. Figure 5

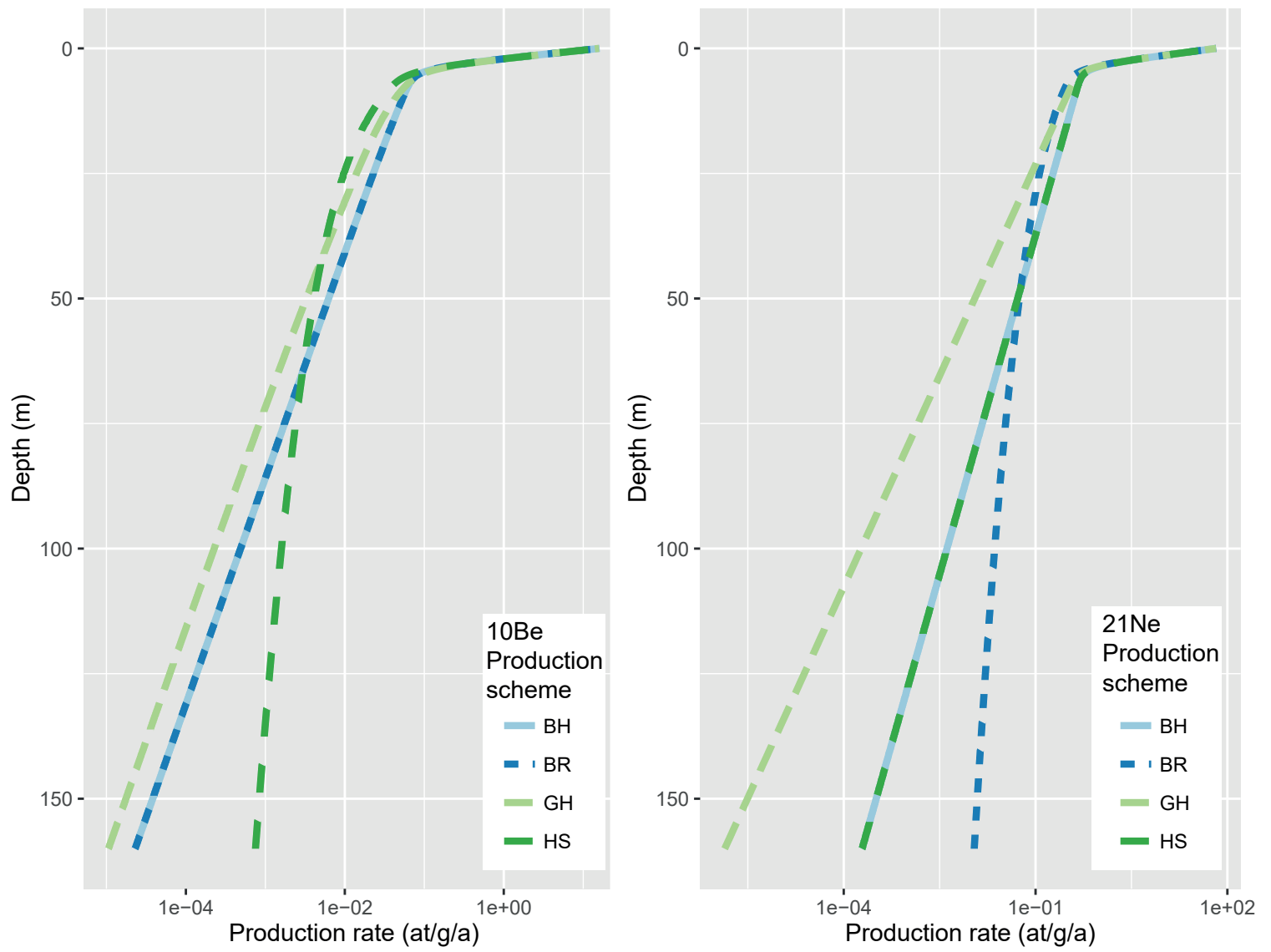


Sanchez et al. Figure 6

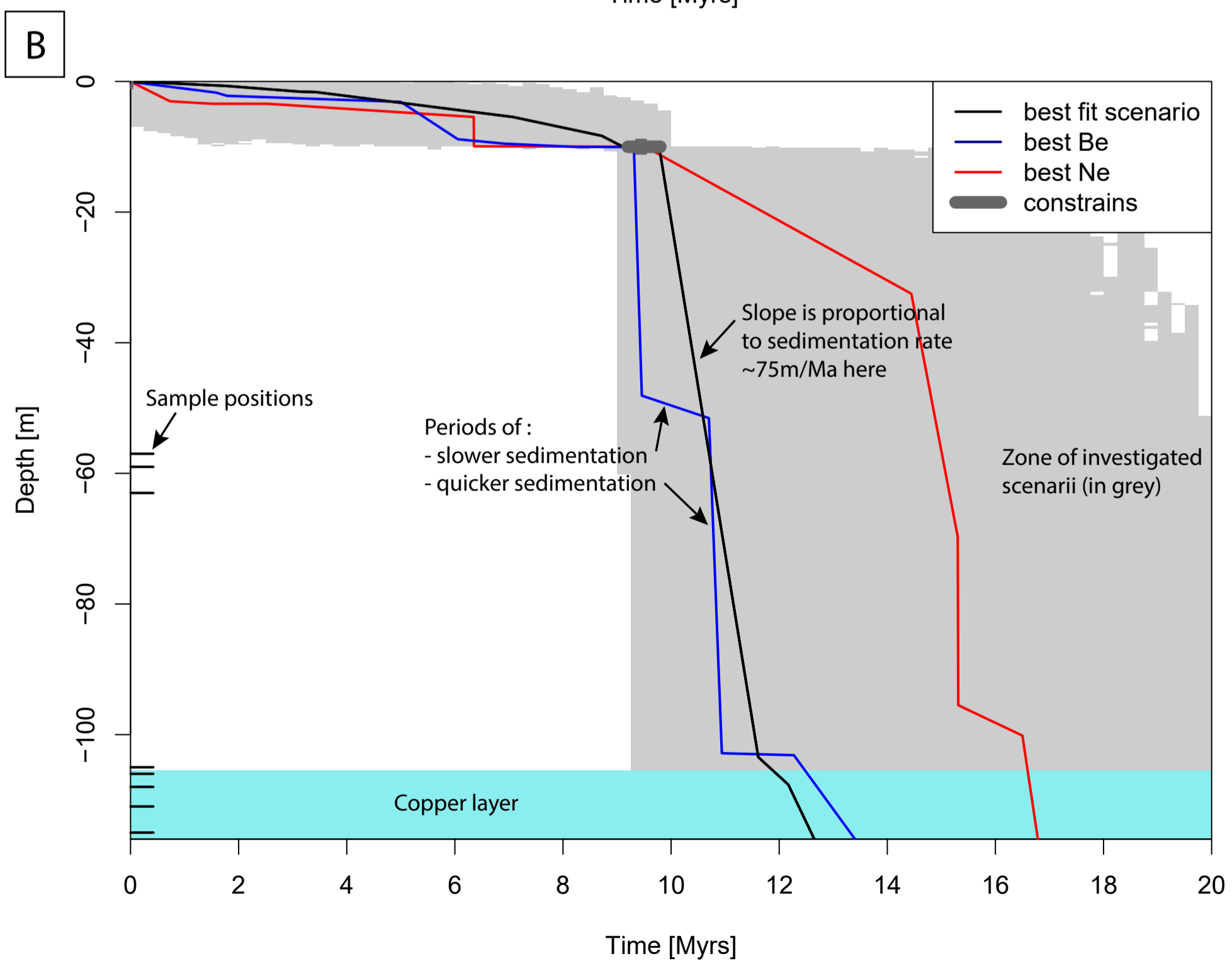
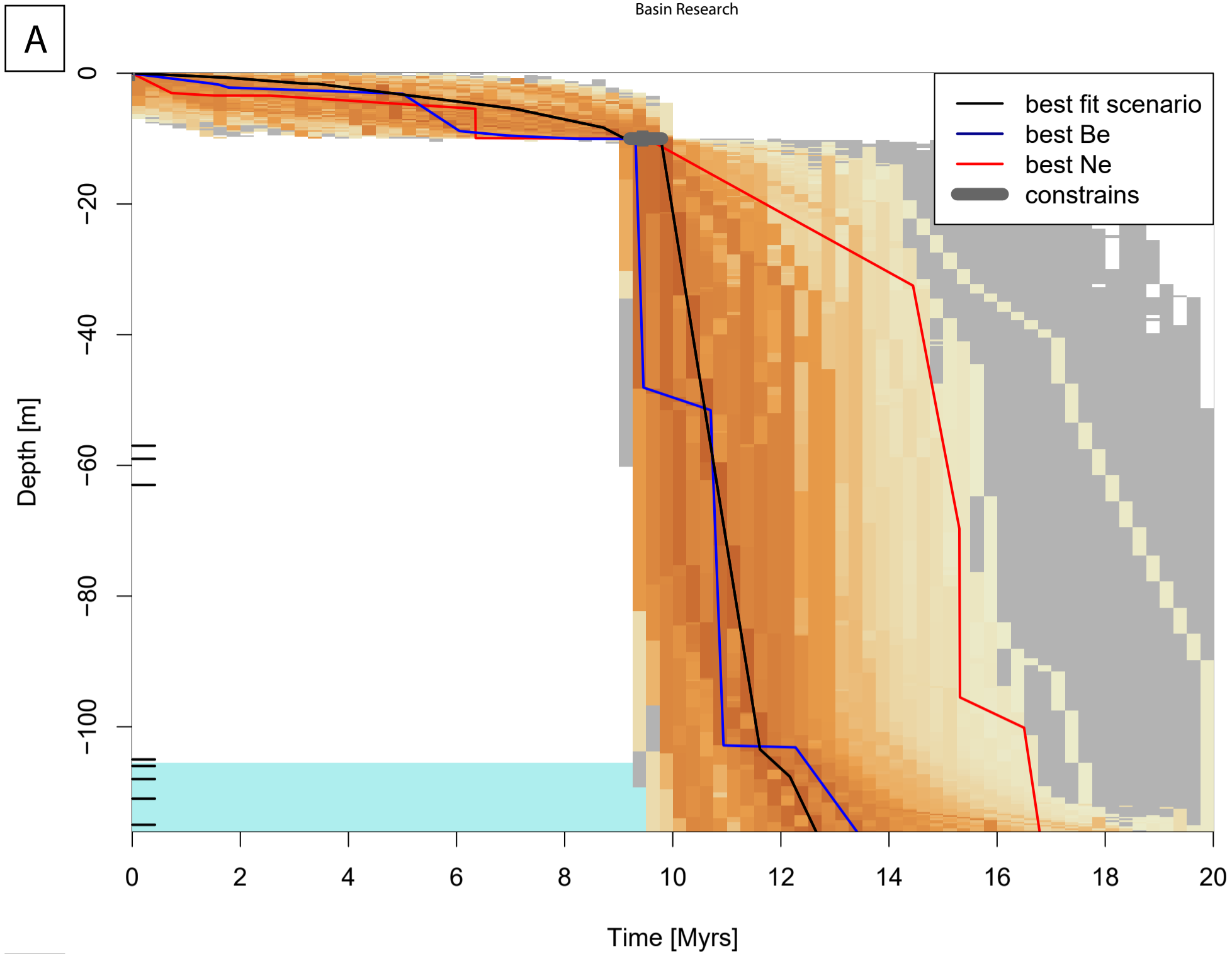


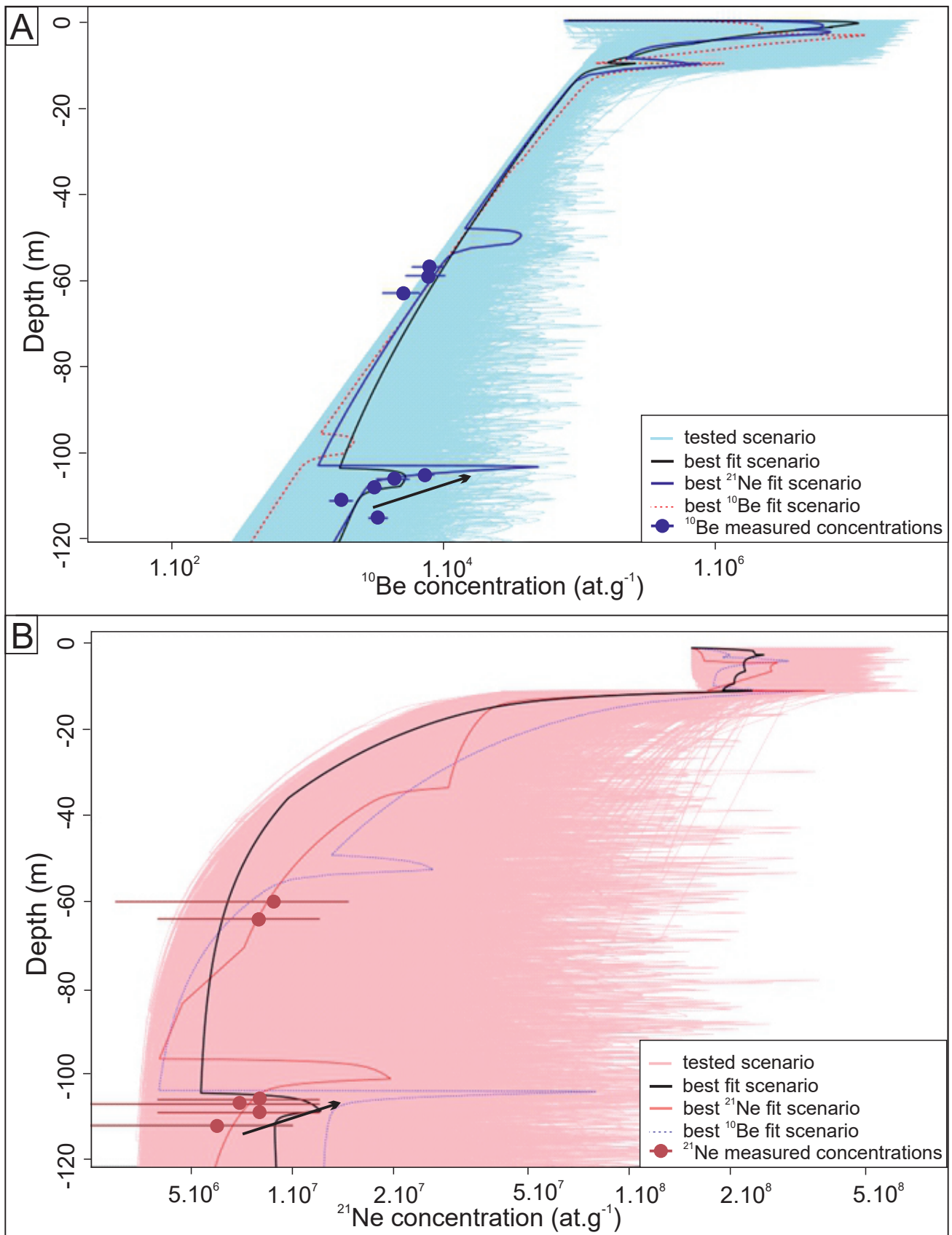
Bipyramid automorph quartz found in MIR13-01 reworked from 9.5 Ma-old ignimbrite (Riquelme et al., 2018)

111x80mm (72 x 72 DPI)

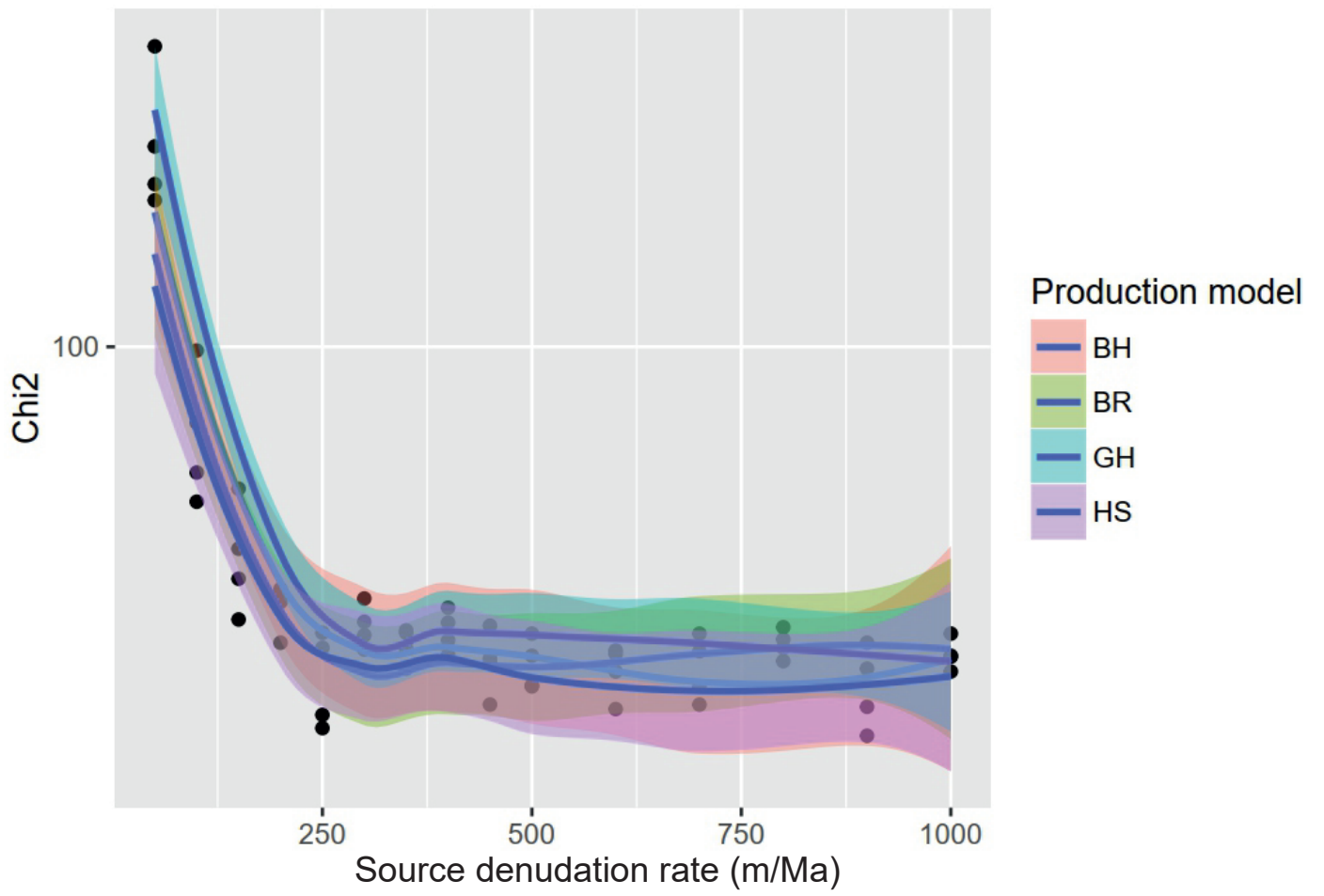


Sanchez et al. Figure 8

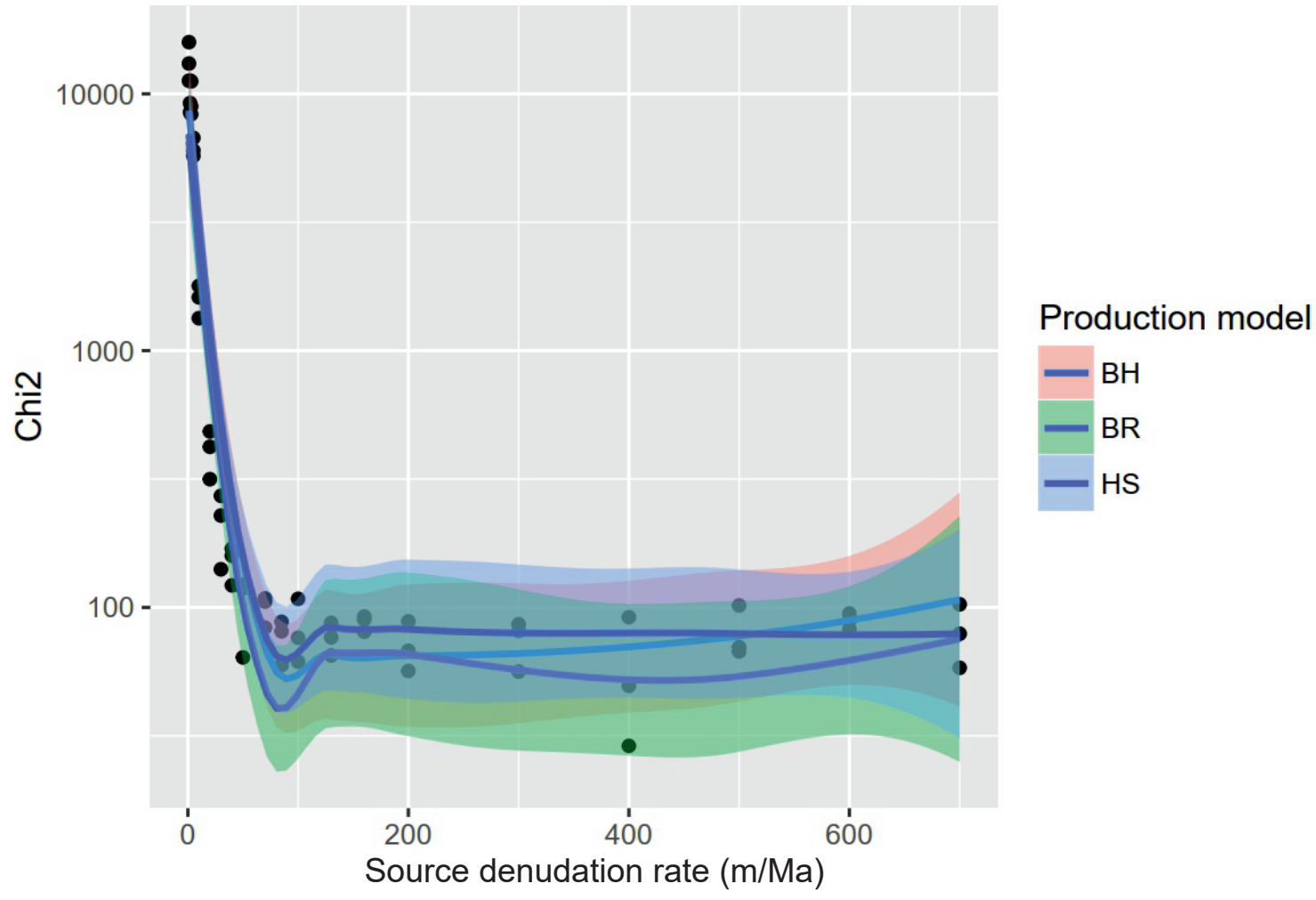




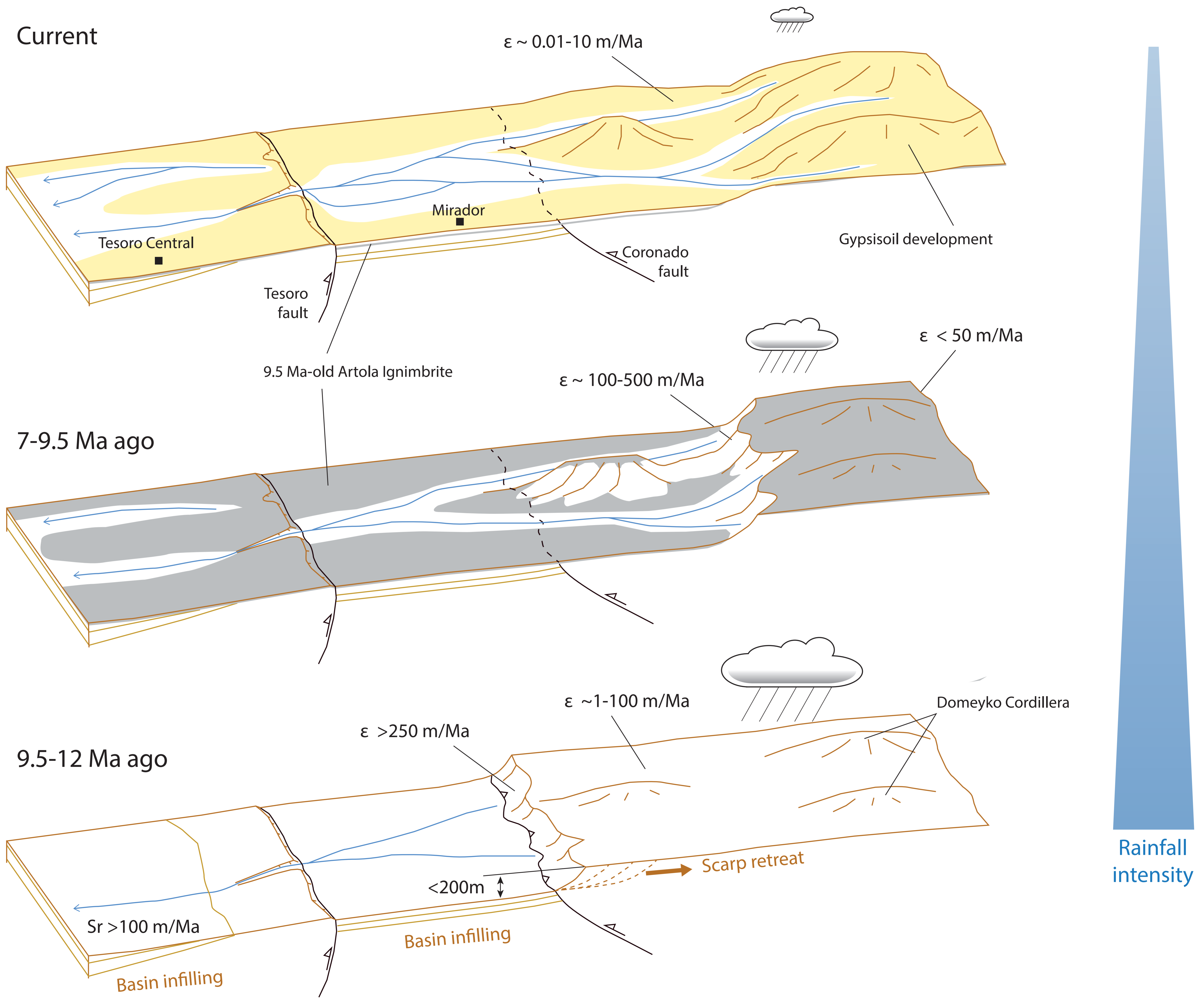
Sanchez et al. Figure 10



Sanchez et al. Figure 11



Sanchez et al. Figure 12



Sanchez et al. Figure 13

Supporting information

Contents

1	Sample preparation	1
2	Reference inversion.....	3
2.1	Reference inversion, production scheme BH	4
2.2	Reference inversion, production scheme BR.....	7
2.3	Reference inversion, production scheme HS.....	9
3	Density in reference experiment.....	11
4	Reference inversion for el Mirador pit	13
5	Test inversion for Davis et al. 2014 data	15

1 Sample preparation

Samples were first crushed and sieved to select the granulometric fraction between 0.5 and 1 mm. Magnetic minerals were separated from the bulk by a magnetic separator (Frantz L-1). Then, the non-magnetic fractions underwent a series of leaching steps with a mixture of concentrated hydrochloric and hexafluorosilicic acids to remove all minerals but quartz. Meteoric ^{10}Be was removed from quartz by three partial dissolutions with concentrated hydrofluoric acid (Brown et al., 1991). Decontaminated quartz was then divided into two aliquots.

The first aliquots were used for ^{10}Be analysis at GET (except MIR-10, see **Error! Reference source not found.**). Decontaminated quartz was totally dissolved with concentrated hydrofluoric acid after adding $\sim 310 \mu\text{g}$ of ^9Be carrier ($\sim 2.4 \times 10^{19}$ atoms of ^9Be , Table 2). The resulting solutions were evaporated until dryness and samples were re-dissolved with hydrochloric acid.

Meanwhile the sample preparation the grain morphology was observed and specific grain shapes were observed. In sample MIR13-01, , which is stratigraphically just above the 9.5 Ma-old ignimbrite (De Silva, 1989; Riquelme et al., 2018), the quartz minerals present bipyramidal shapes (see **Error! Reference source not found.**7). This crystal automorph shape suggests that it has a volcanic origin and was not transported over a long distance. MIR13-01 quartz minerals are thus likely to come from upstream erosion of the 9.5 Ma-old ignimbrite.

Afterwards, samples passed through an anion exchange column to remove iron and a cation exchange column to discard boron and recover Be. Finally, the eluted Be was precipitated to $\text{Be}(\text{OH})_2$ with concentrated ammonia and oxidized to BeO. After target preparation at CEREGE by mixing Niobium powder with the BeO, the $^{10}\text{Be}/^9\text{Be}$ ratios were measured by Accelerator Mass Spectrometry (AMS) at the French National AMS Facility ASTER of CEREGE in Aix-en-Provence (Arnold et al., 2010). The measured $^{10}\text{Be}/^9\text{Be}$ ratios were calibrated against a house standard STD-11 with an assigned value of $(1.191 \pm 0.013) \times 10^{-11}$ (Braucher et al., 2015). This calibration procedure is similar to the KNSTD07 standardization (Nishiizumi et al., 2007; Braucher et al., 2015). Analytical 1σ uncertainties include uncertainties in AMS counting statistics, uncertainty in the $^{10}\text{Be}/^9\text{Be}$ standard, an external AMS error

of 0.5% (Arnold et al., 2010), and a chemical blank measurement. In all computations, a ^{10}Be half-life of $(1.387 \pm 0.01) \times 10^6$ years was used (Chmeleff et al., 2010; Korschinek et al., 2010).

The second quartz aliquots were used for measuring the cosmogenic ^{21}Ne concentration at the CRPG Nancy noble gas lab. The purity of the quartz samples was checked under a binocular microscope and completed by DRX analysis. Quartz samples were packed in tin foil and loaded in a custom designed carousel resistance furnace (Zimmermann et al., 2012) connected to a purification line with a cryogenic trap. Neon isotope abundances were measured with the Split Flight Tube mass spectrometer dedicated to the cosmogenic noble gas analysis (Vermeesch et al., 2015). The extraction of neon by quartz step-heating, gas purification and analytical procedures was similar to the procedures described in Sartégou et al. (2018). Computation of the atmosphere-corrected cosmogenic ^{21}Ne concentration ($^{21}\text{Ne}_{\text{cos}}$) was performed following:

$$^{21}\text{Ne}_{\text{cos}} = R_c \times ^{20}\text{Ne}_{\text{atm}} \times (R_m - R_a)/(R_c - R_a), \text{ (equation 2)}$$

where $^{20}\text{Ne}_m$ (at.g^{-1}) is the measured ^{20}Ne concentration in quartz, $R_c = 0.8$ the cosmogenic $^{21}\text{Ne}/^{20}\text{Ne}$ production ratio (Niedermann, 2002); R_m is the measured $^{21}\text{Ne}/^{20}\text{Ne}$ ratio and $R_a = 0.002905$ is the atmospheric $^{21}\text{Ne}/^{20}\text{Ne}$ ratio (Honda et al., 2015) (Figure A1).

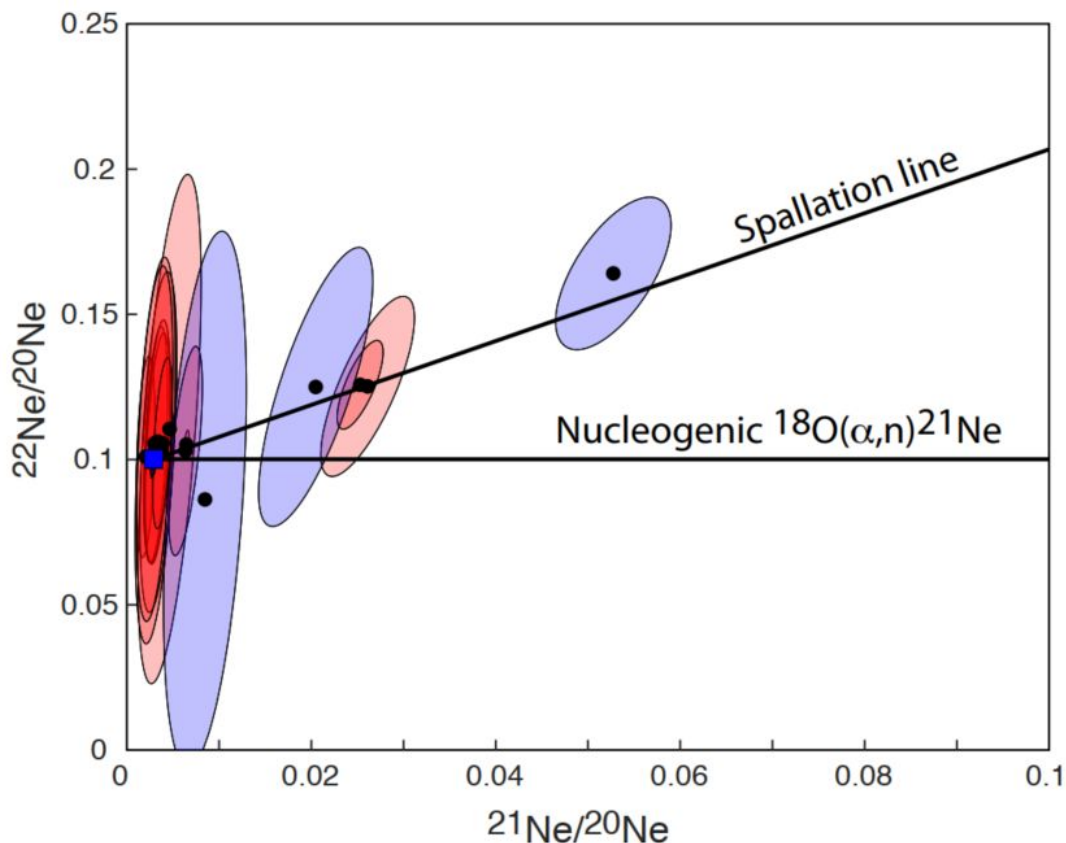


Figure A1: Neon isotopic ratios measured in all heating steps of the samples and the CRONUS-A standard presented in this study. The ellipses represent the 68% confidence region. The plot accounts for the covariance between errors. The colors represent the neon extraction temperature: blue, $< 800^\circ\text{C}$, red, $> 1200^\circ\text{C}$. The spallation line is computed assuming a pure mixing between the atmospheric end members (blue square, the neon isotopic ratios for air are from Honda et al., 2015) and assuming a $^{22}\text{Ne}/^{21}\text{Ne}$ production ratio of 1.1 (Niedermann, 2002).

The calibration was checked by analyzing CRONUS-A quartz standards on the same analytical system (Dunai et al., 2005; Vermeesch et al., 2015). All of the measured CRONUS-A standards yielded $^{21}\text{Ne}_{\text{cos}}$ concentrations that are consistent with the range of values reported by several international laboratories (Vermeesch et al., 2015).

2 Sensitivity analysis

Parameter tested	Reference	Result tested	Reference value	Value when varying the tested parameter	Reference
Production scheme	BR	Copper rich layer age	10-14 Ma	Not significantly different	Appendix
		Denudation rate before 9.5 Ma	> 250	Not significantly different	Figure 11
Density of the sediments	2300 kg/m ³	Copper rich layer age	10-14 Ma	Not significantly different, larger range for lower densities (10-15Ma for 2100 kg/m ³ , 10-16 Ma for 1900 kg/m ³)	Appendix
		χ^2	10-20	Not significantly different for higher densities. Increases for lower densities up to ~60 (worse fit), except for the GR production scheme	Figure A12

Table 1. Main parameters tested for a sensitivity analysis

The effect of the main parameters tested is found in Table A1.

3 Reference inversion

The following Figure A2 shows the inverted sedimentation rate as a function of depth. This figure highlights the different sediment phases (Figure A2). Before basin infilling (we note that this phase is poorly constrained by our sampling strategy), the sedimentation rate was in the range 10^{-7} - 10^{-5} m/a (0.1-10 m/Ma). During basin infilling (depth between ~105 and ~10 m), the sedimentation rate increased to 10^{-5} - 10^{-4} m/a (10-500 m/Ma). It has then dropped to less than 10^{-6} m/a (< 1 m/Ma) for the last 10 Ma.

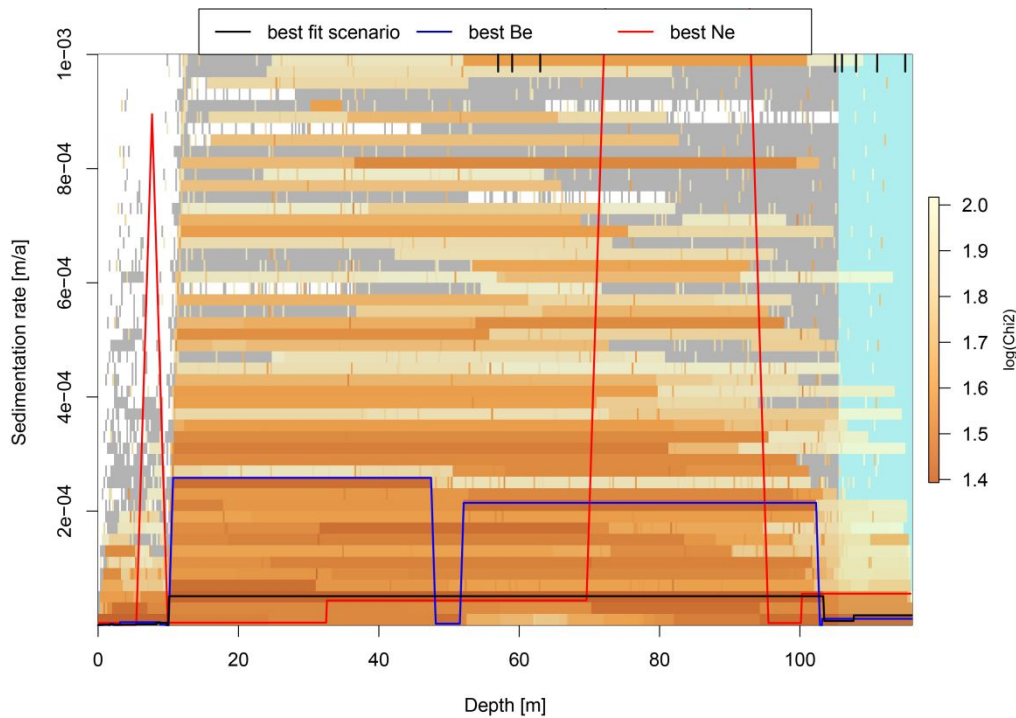


Figure A2. Graph representing the sedimentation rate (m/a) vs. depth (m) (reference inversion, BR). The black, blue and red lines correspond to the best fit scenarios for both ^{10}Be and ^{21}Ne , ^{10}Be only and ^{21}Ne only, respectively.

In the following, we present the results from the reference inversion with the other production schemes used. As a reminder, the different schemes used are called GH, BH, HS and BR (see **Error! Reference source not found.** and **Error! Reference source not found.** for more details). The first letter stands for the ^{10}Be production scheme: G stands for Granger and Muzikar (2001), B for Braucher et al. (2011), H for Heisinger et al. (2002) formulation with the updated muon interaction parameters given by Balco (2017). The second letter is indicative of the ^{21}Ne production scheme: H and S stands for Heisinger et al. (2002) and R for Braucher et al. (2011); ^{10}Be production SLHL is set to 4.15 at/g/a (Martin et al., 2017), and the $^{21}\text{Ne}/^{10}\text{Be}$ ratio is 4.12 (Balco & Shuster, 2009; Kober et al., 2011). The reference is model BR.

3.1 Reference inversion, BH production scheme

The constant denudation rate is 500 m/Ma. The next figures correspond to inversion with BH production systematics; B indicates the spallation and the muon attenuation and productions are those from Braucher et al. (2011) for ^{10}Be . For ^{21}Ne , the attenuation scheme follows the definition by Heisinger et al. (2002).

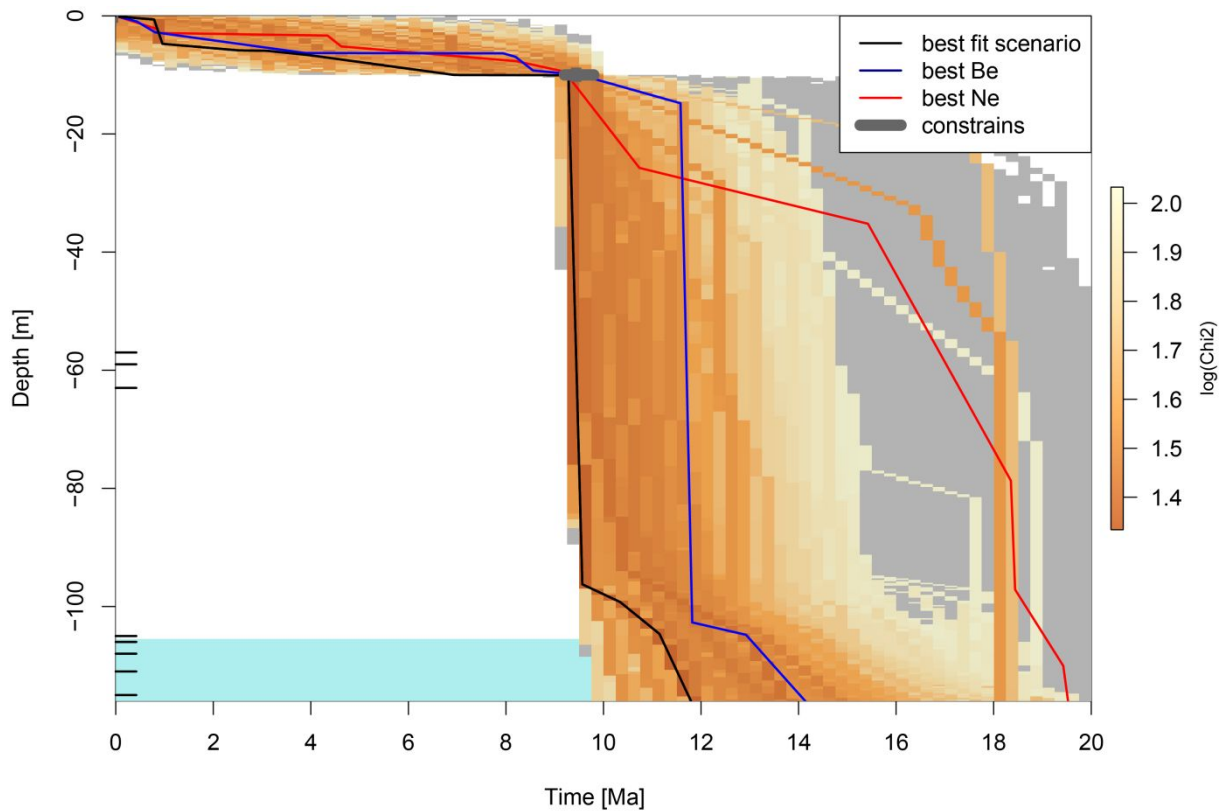


Figure A3. Age of the sediments (Ma) in function of the depth (m) in the Tesoro Mine, using the BH production parameters. The black, blue and red lines correspond to the best fit scenario for both ^{10}Be and ^{21}Ne , ^{10}Be and ^{21}Ne only, respectively.

The comparison between Figure A3 and Figure 9 indicates that this inversion produces similar results, but that they are shuffled by a couple of very different likely scenarios (i.e., those on the right, at around 18-20 Ma). Disregarding these rare scenarios leads to the conclusion that the probable age of the copper layer is around 10-16 Ma).

Figure A4 shows that the data are satisfactorily adjusted by the best-fit models. Both ^{10}Be only and $^{10}\text{Be}/^{21}\text{Ne}$ best fit models show a hump, produced by low sedimentation rates during and after deposition of the copper-rich layer. The associated sedimentation rates are shown in Figure A5.

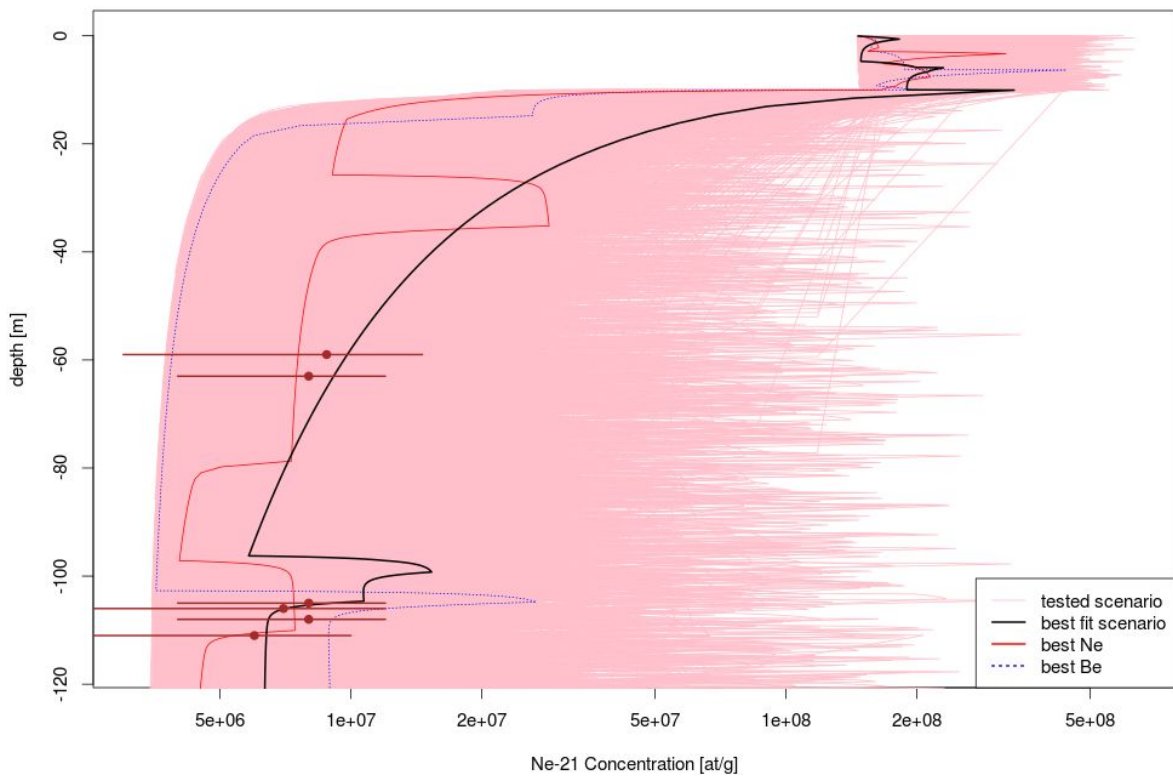
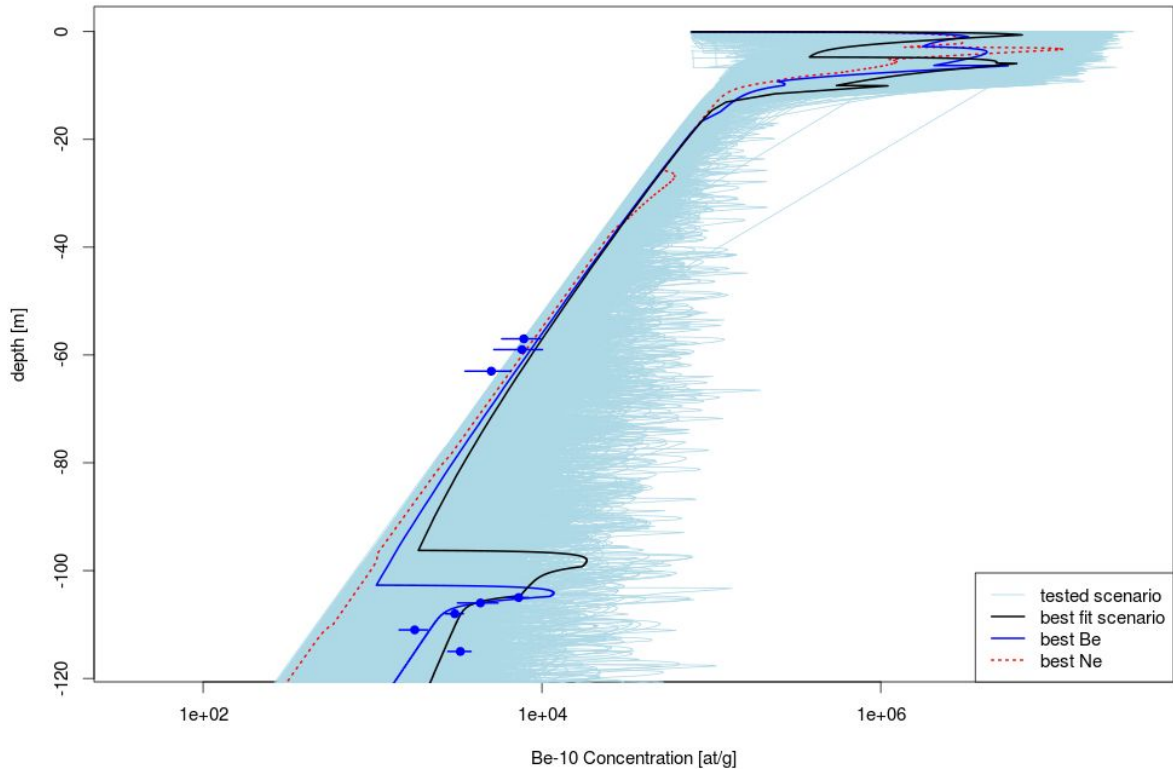


Figure A4. Cosmogenic isotope concentration (reference inversion) in the Tesoro Central open pit using the BH parameters, according to depth; the top figure shows ^{10}Be and the bottom shows ^{21}Ne . For both figures, the light colors correspond to every Monte Carlo scenario tested; the bold lines represent the best χ^2 scenario for ^{10}Be only, ^{21}Ne only and for both nuclides in blue, red and black, respectively. The circles and associated horizontal lines indicate the measured concentrations and their related

uncertainties.

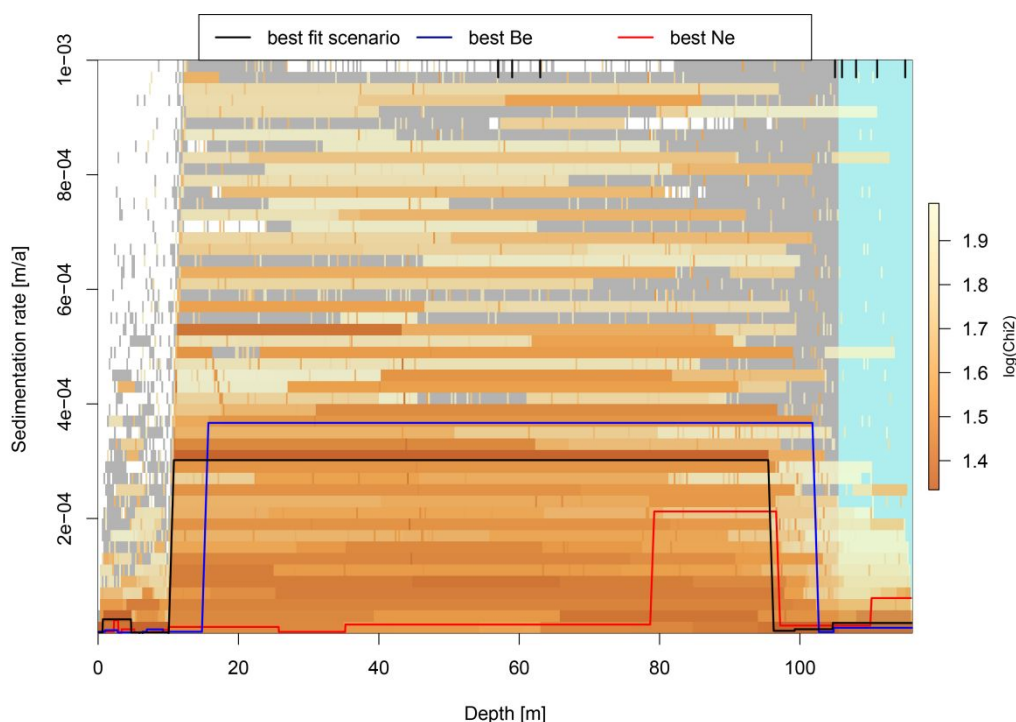


Figure A5. Sedimentation rate vs. depth in the reference inversion with the BH production scheme. The black, blue and red lines correspond to the best fit scenario for both ^{10}Be and ^{21}Ne , ^{10}Be and ^{21}Ne only, respectively. This complex graph basically indicates that the copper layer deposition is characterized by relatively low sedimentation rates and is followed by even lower sedimentation rates (depth ~ 100 m). A large increase in sedimentation rates is observed from a depth of 95-100 m to a depth of 10 m (Artola ignimbrite). The last 10 Ma, corresponding to the last 10 m is characterized by very low sedimentation rates ($\sim 10^{-6}$ m/a).

3.2 Reference inversion, GR production scheme

The denudation rate is still at 500 m/Ma. The next figures correspond to inversion with GR production systematics; G indicates the spallation and muon attenuation and productions are those from Granger and Muzikar (2001) for ^{10}Be . For ^{21}Ne , the attenuation scheme follows the definition by Heisinger et al. (2002).

The comparison between Figure A6 and Figure 9 indicates that, similarly to what observed with production BH (Figure A3), this inversion produces similar results, leading to the conclusion that the probable age of the copper layer is around 10-14 Ma.

As expected, Figure A7-B is similar to Figure A4-B. On the contrary, the comparison of Figure A7-A with Figure A4-A and Figure 10 indicates that the GR production scheme can produce lower ^{10}Be concentrations, and is the most suitable in this case.

The sedimentation rates (Figure A8) and infilling scenarios (Figure A6) indicate, as shown in the other production schemes, that the copper-rich layer was deposited during a period of low sedimentation rates.

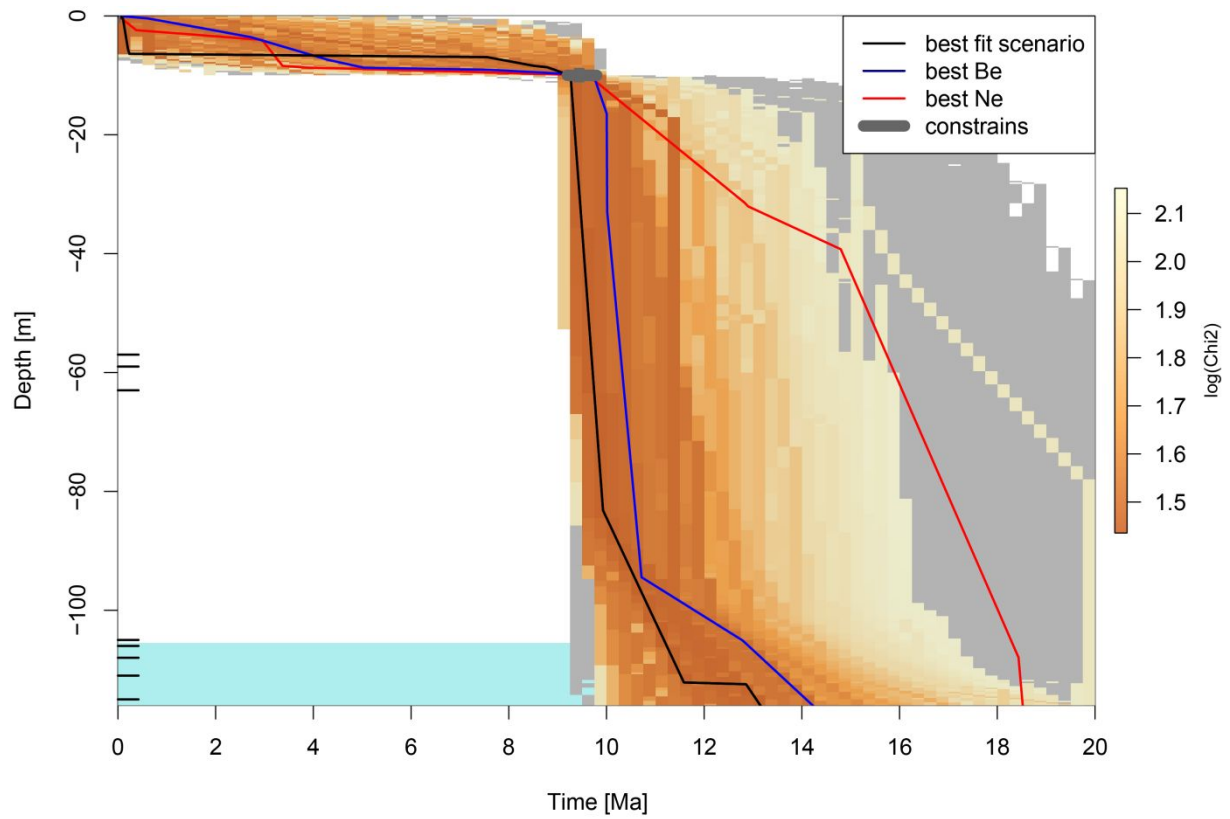


Figure A6. Age of the sediments (Ma) in function of the depth (m) in the Tesoro Mine, using the BR production parameters. The black, blue and red lines correspond to the best fit scenario for both ^{10}Be and ^{21}Ne , ^{10}Be and ^{21}Ne only, respectively.

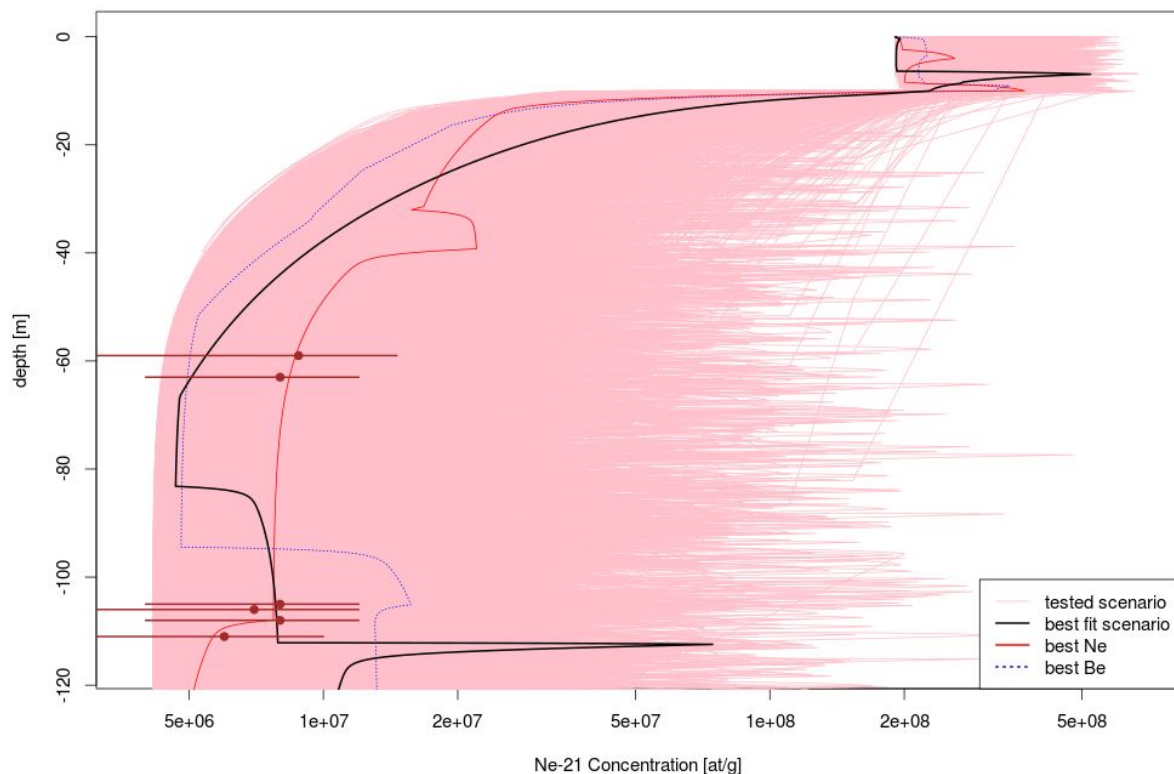
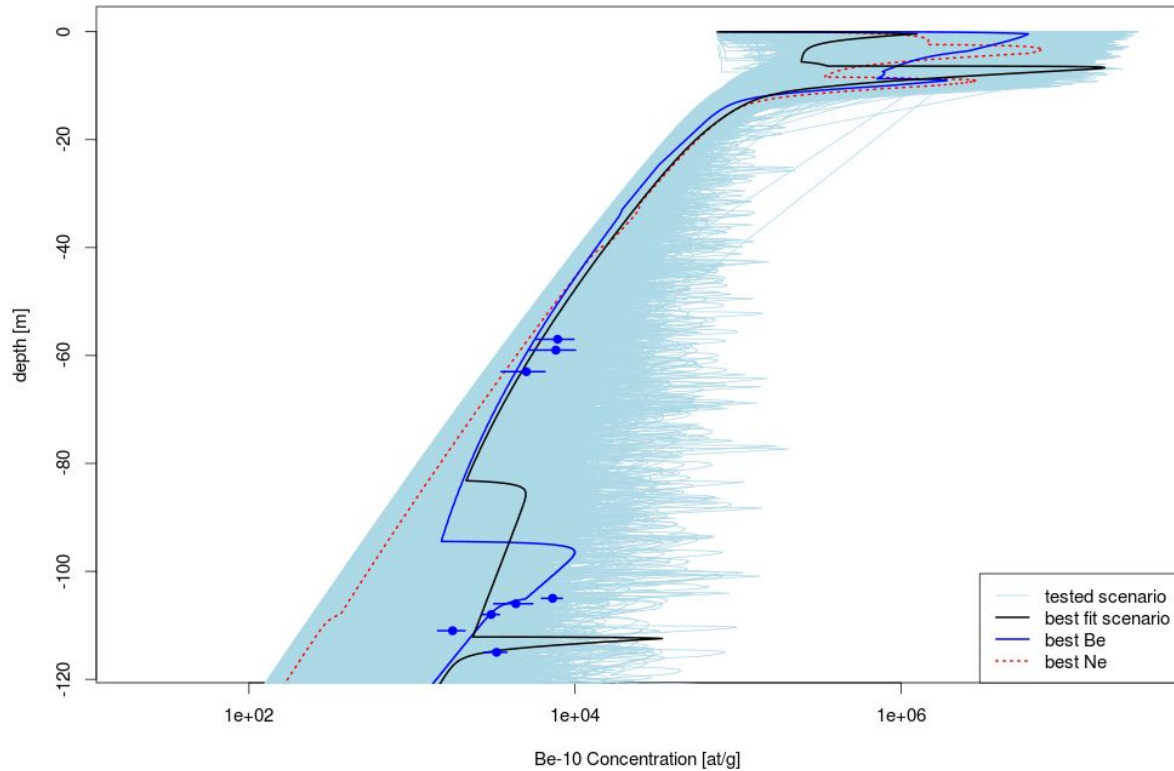


Figure A7. Cosmogenic isotope concentration (reference inversion, GR production scheme) in the Tesoro Central open pit using the GR parameters, according to depth; the top figure shows ^{10}Be and the bottom shows ^{21}Ne . For both figures, the light colors correspond to every Monte Carlo scenario tested; the bold lines represent the best χ^2 scenario for ^{10}Be only, ^{21}Ne only and for both nuclides in blue, red and black, respectively. The circles and associated horizontal lines indicate the measured concentrations and their related uncertainties.

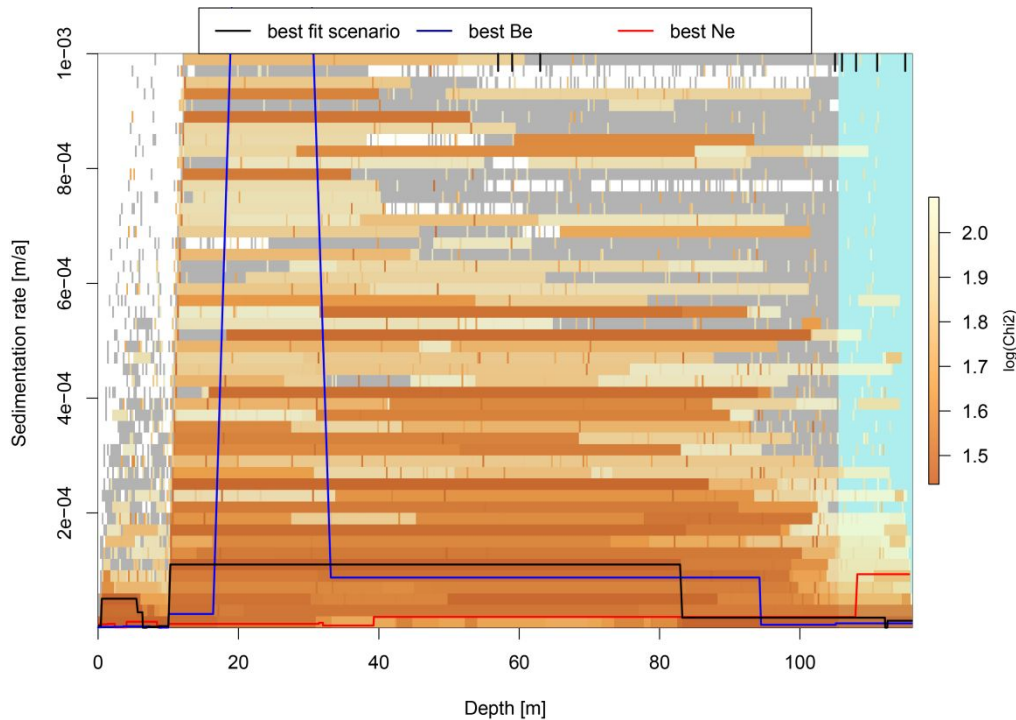


Figure A8. Graph representing the sedimentation rate (m/a) vs. time in Ma (reference inversion) with GR production parameters. The black, blue and red lines correspond to the best fit scenario for both ^{10}Be and ^{21}Ne , ^{10}Be and ^{21}Ne only, respectively.

3.3 Reference inversion, HS production scheme

The denudation rate is still at 500 m/Ma. The next figures correspond to inversion with HS production systematics; the attenuation schemes for both nuclides are taken from the formulation given by Heisinger et al. (2002) with the updated muon interaction parameters described by Balco (2017). It should be noted that this scheme does not use exponential approximations for the muon production at depth but instead propagates the muon fluxes through the Earth's surface, quantifying nuclide production as a function of their spallation reaction cross-section and capture probability.

Figure A9 highlights a limited number of very fit scenarios which result in an age of ~ 13 Ma for the copper layer. But this apparent precision hides a greater variability than that seen with other production schemes (see Figure A9). This may be due to the fact that this production scheme hardly produces ^{10}Be concentrations as low as those observed in our analyses concentrations (Figure A10).

The dispersion of the scenarios can also be seen in the sedimentation rates: the different stages of evolution can be seen on the graph (Figure A11), but they are much less marked than for the other production schemes.

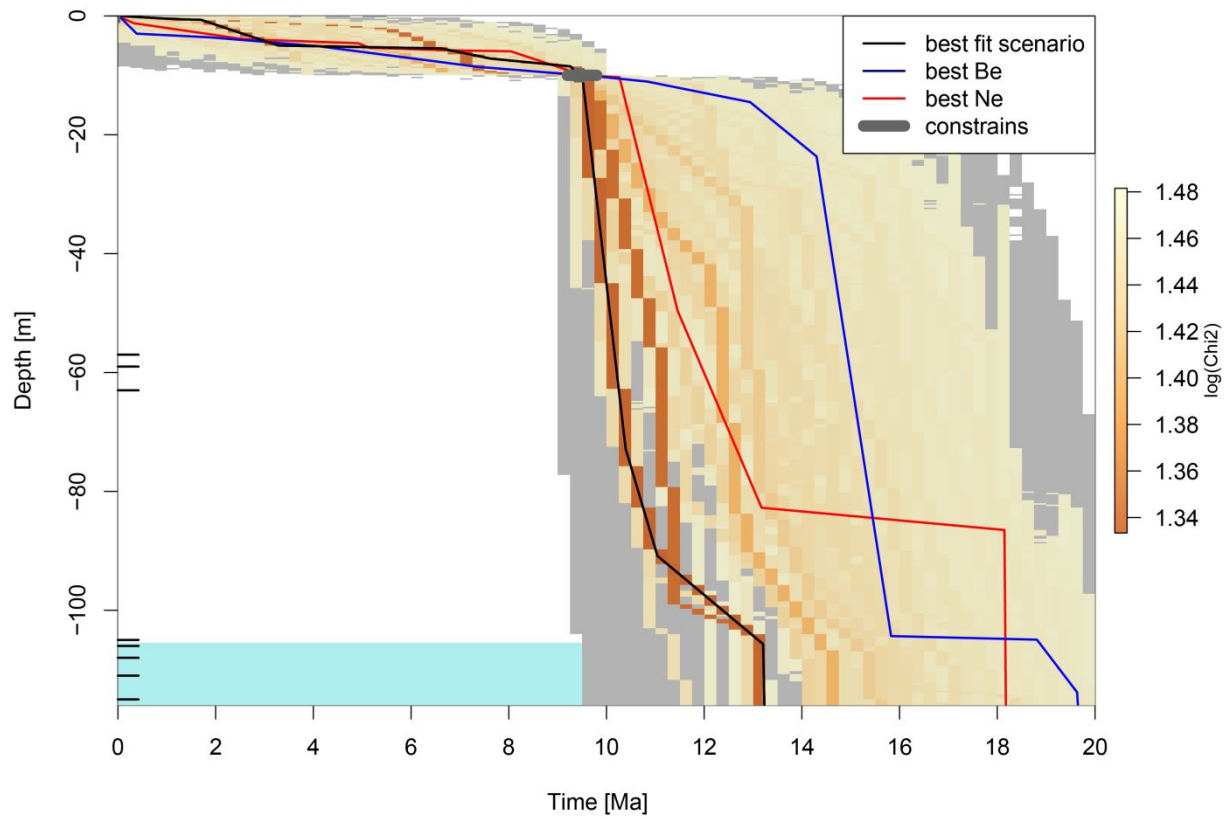


Figure A9. Age of the sediments (Ma) in function of the depth (m) in the Tesoro Mine, using the HS production parameters. The black, blue and red lines correspond to the best fit scenario for both ^{10}Be and ^{21}Ne , ^{10}Be and ^{21}Ne only, respectively.

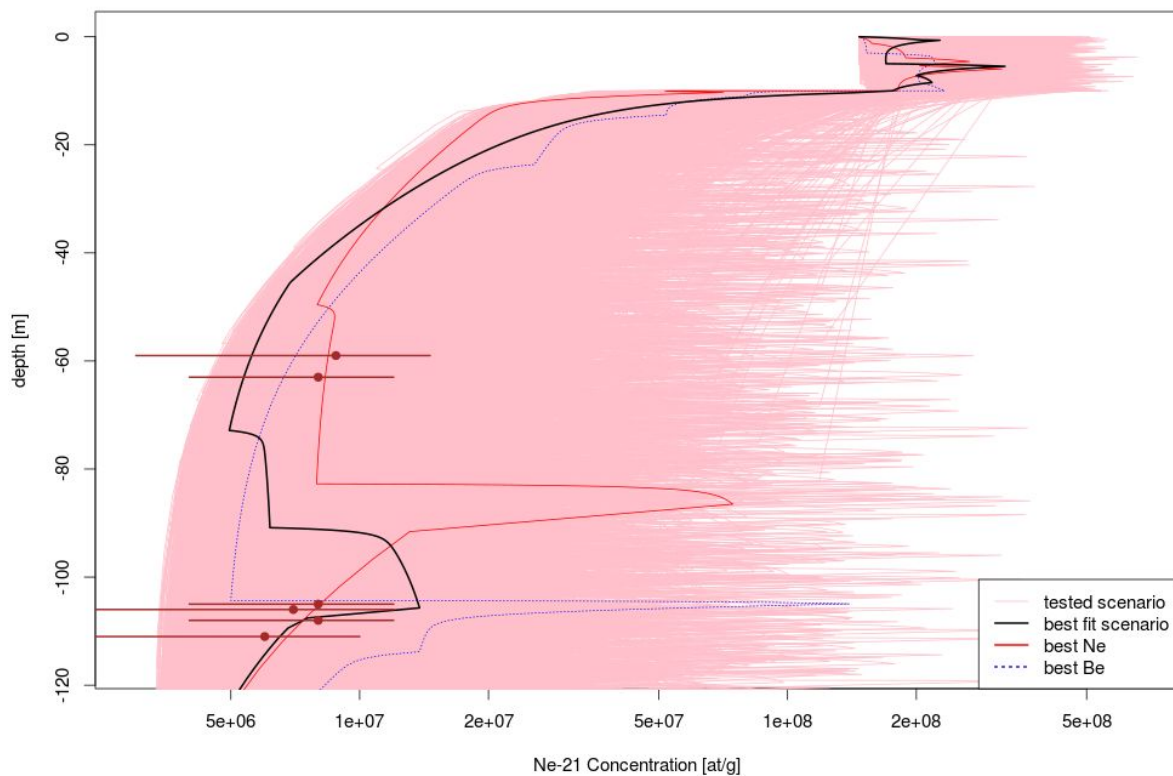
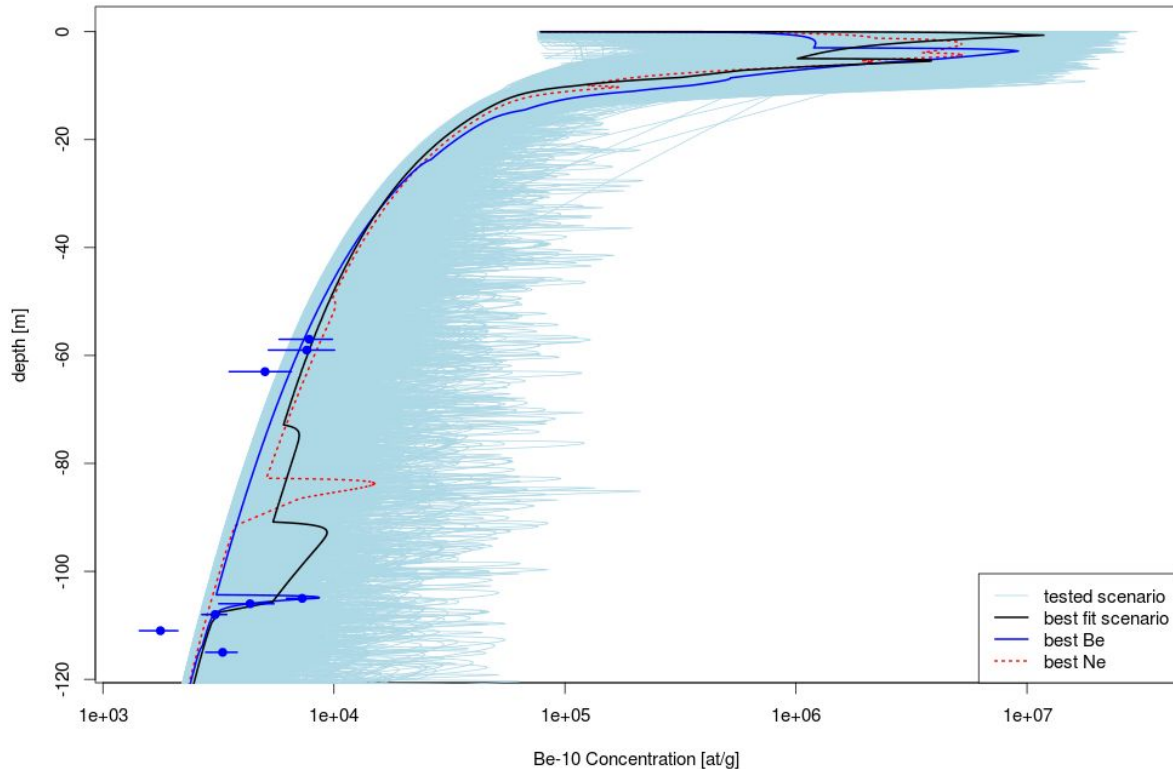


Figure A10. Cosmogenic isotope concentration (reference inversion) in the Tesoro Central open pit using the HS parameters, according to depth; the top figure shows ^{10}Be and the bottom shows ^{21}Ne . For both figures, the light colors correspond to every Monte Carlo scenario tested; the bold lines represent the best χ^2 scenario for ^{10}Be only, ^{21}Ne only and for both nuclides in blue, red and black, respectively. The circles and associated horizontal lines indicate the measured concentrations and their related uncertainties.

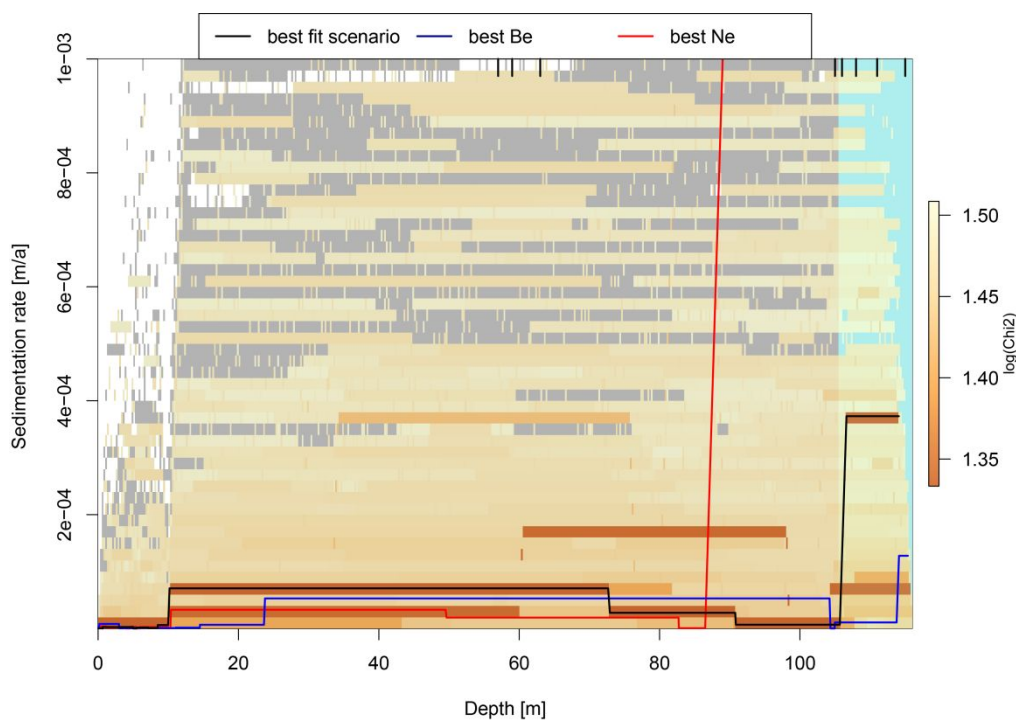


Figure A11. Graph representing the sedimentation rate (m/a) vs. time in Ma (reference inversion) with HS production parameters. The black, blue and red lines correspond to the best fit scenario for both ^{10}Be and ^{21}Ne , ^{10}Be and ^{21}Ne only, respectively.

4 Density in the reference experiment

This section shows experiments based on the El Tesoro reference inversion (density of 2500 kg/m^3) but with variable sedimentary layer densities of 1900, 2100, and 2500 kg/m^3 . If the sediment filling the basin were denser, X^2 would be lower (from ~ 60 for 1900 kg/m^3 to 20 for $2200\text{-}2500 \text{ kg/m}^3$, Figure A12) and the sedimentation ages would shift slightly to younger ages (comparison between Figure A13, Figure A14, Figure A15 and Figure 9). The Granger (GR) model stands out for its ability to fit even at all densities.

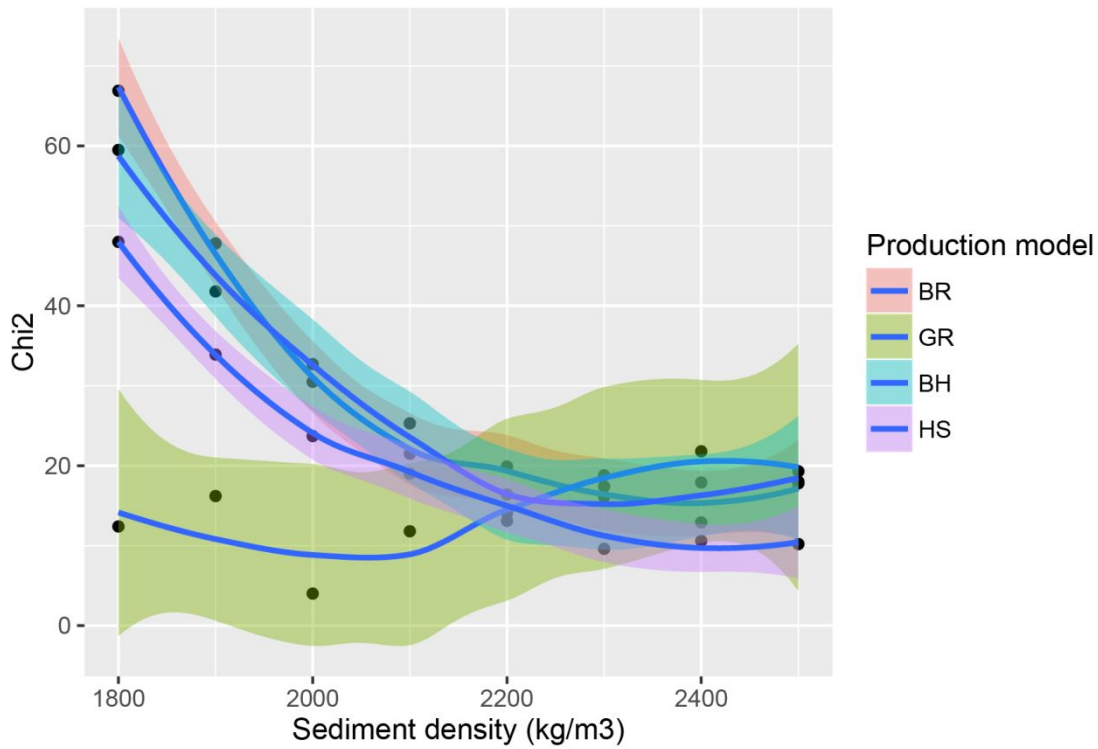


Figure A12. Value of χ^2 in function of sedimentary basin infill density for the various schemes (reference inversion). Except for GR, the best χ^2 values correspond to densities between 2200 and 2500 kg/m³.

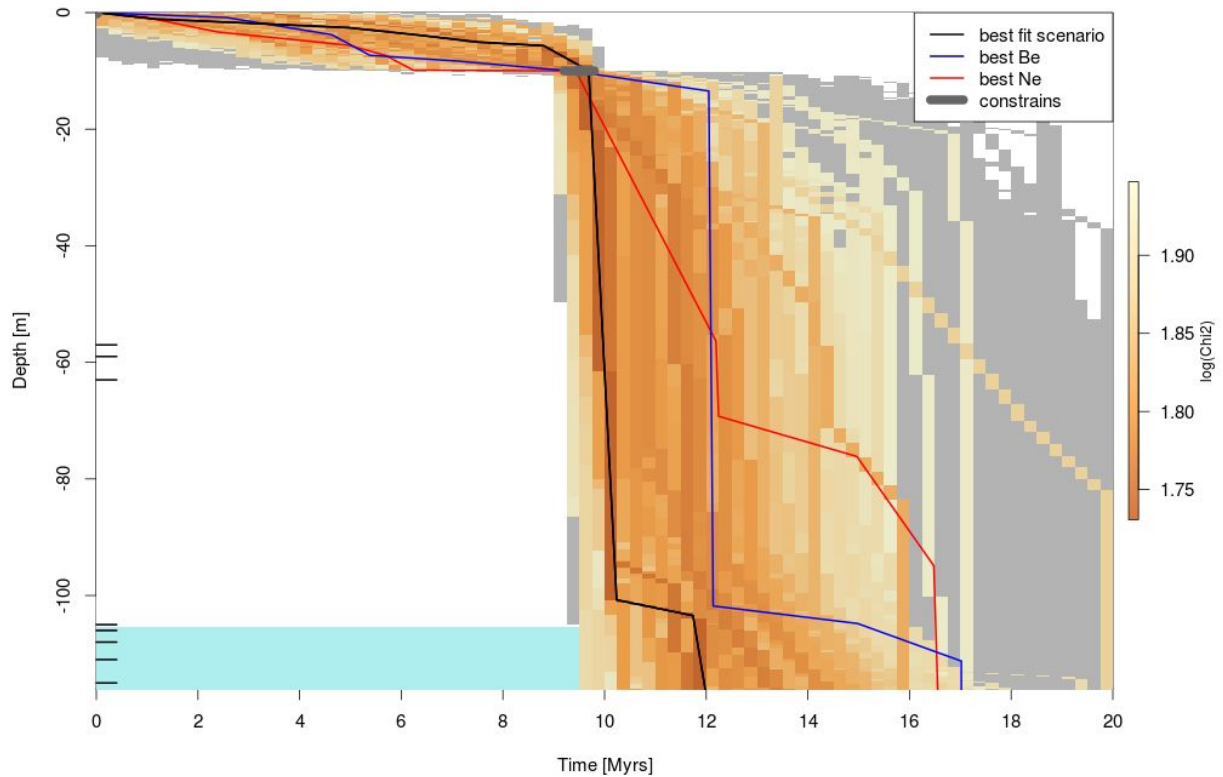


Figure A13. Age of the sediments (Ma) in function of the depth (m) in the Tesoro Mine (reference model for the BR production scheme), with a sediment density of 1900 kg/m³. The black, blue and red lines correspond to the best fit scenario for both ¹⁰Be and ²¹Ne, ¹⁰Be and ²¹Ne only, respectively.

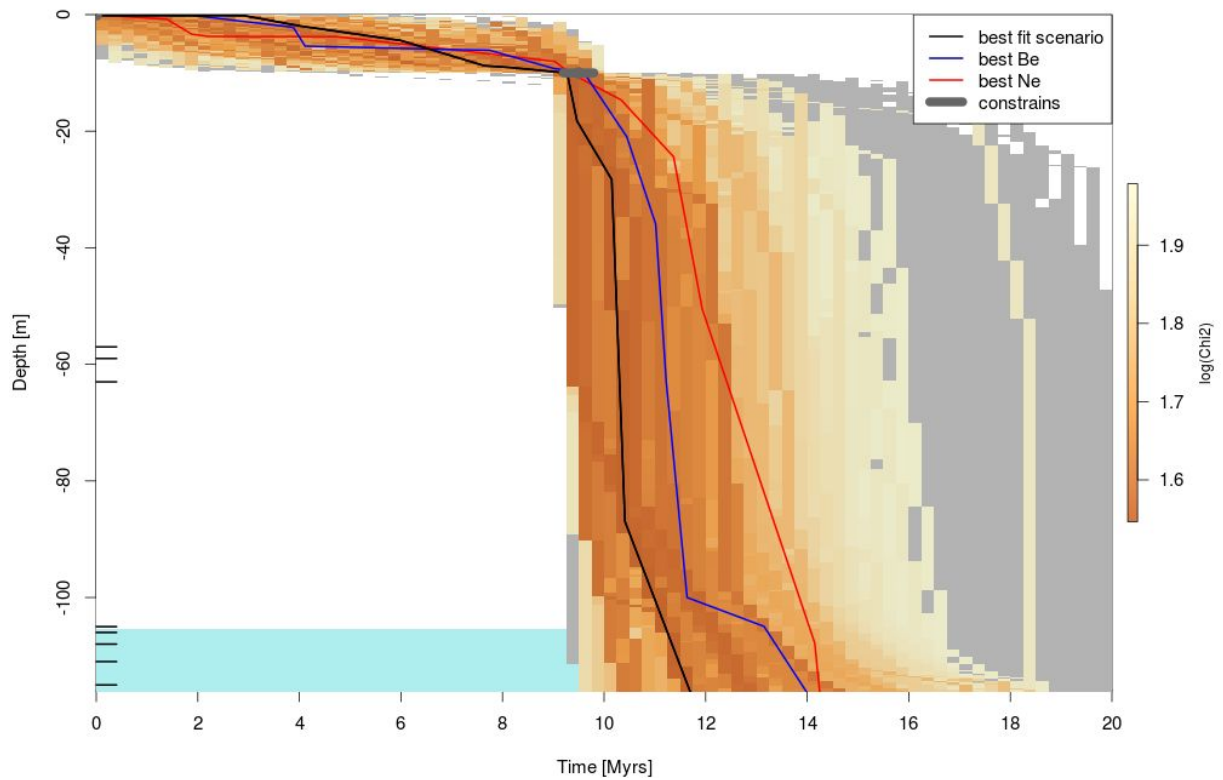


Figure A14. Age of the sediments (Ma) in function of the depth (m) in the Tesoro Mine (reference model for the BR production scheme), with a sediment density of 2100 kg/m^3 . The black, blue and red lines correspond to the best fit scenario for both ^{10}Be and ^{21}Ne , ^{10}Be and ^{21}Ne only, respectively.

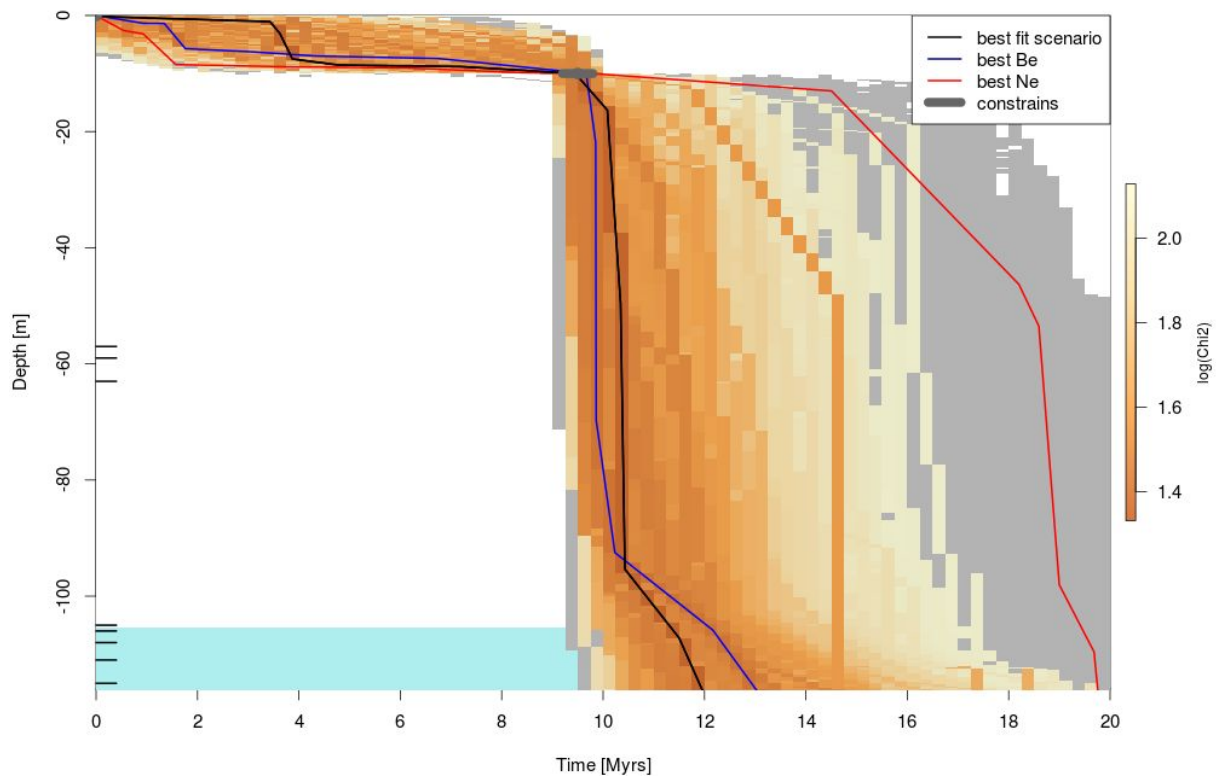


Figure A15. Age of the sediments (Ma) in function of the depth (m) in the Tesoro Mine (reference model for the BR production scheme), with sediment density of 2500 kg/m^3 . The black, blue and red lines correspond to the best fit scenario for both ^{10}Be and ^{21}Ne , ^{10}Be and ^{21}Ne only, respectively.

5 Reference inversion for the El Mirador pit

The El Mirador pit inversion was treated as the reference inversion for El Tesoro (BR production scheme), but with a source erosion rate = 300 m/Ma . We recall that the concentration of ^{21}Ne in the deepest part of the pit could not be measured. The data do not allow the inversions to define a precise history for the period before 10 Ma ago. They favor a relatively continuous sedimentation between 20 and 30 Ma for the bottom (top of the ore body, 70 m below the surface) and 10–20 Ma just below the Artola ignimbrite (Figure A16. Age of the sediments (Ma) in function of the depth (m) in the Mirador Mine, using the BR production parameters. The black, blue and red lines correspond to the best fit scenario for both ^{10}Be and ^{21}Ne , ^{10}Be and ^{21}Ne only, respectively. Figure A16).

The agreement with the data is not satisfactory (Figure A17). The ^{10}Be concentration of MIR-11 (45 m deep) cannot be modeled (it is much too low). The concentration data from MIR-01 (18 m depth) are low but this can be explained by a zero concentration acquired during the exhumation as it comes from the Artola ignimbrite (cf. bipyramidal quartz, Figure 7).

As discussed in the paper, Mirador provides more solid information regarding the period after 10 Ma. In order to better explore this period, we have inverted the three corresponding data only (in descending order MIR-05, MIR-04 and MIR-01, Figure A18). It shows that sedimentation was fastest

between 10 and 8 Ma (up to samples MIR-04 and MIR-05, at a depth of 12-13 m) and was then relatively continuous.

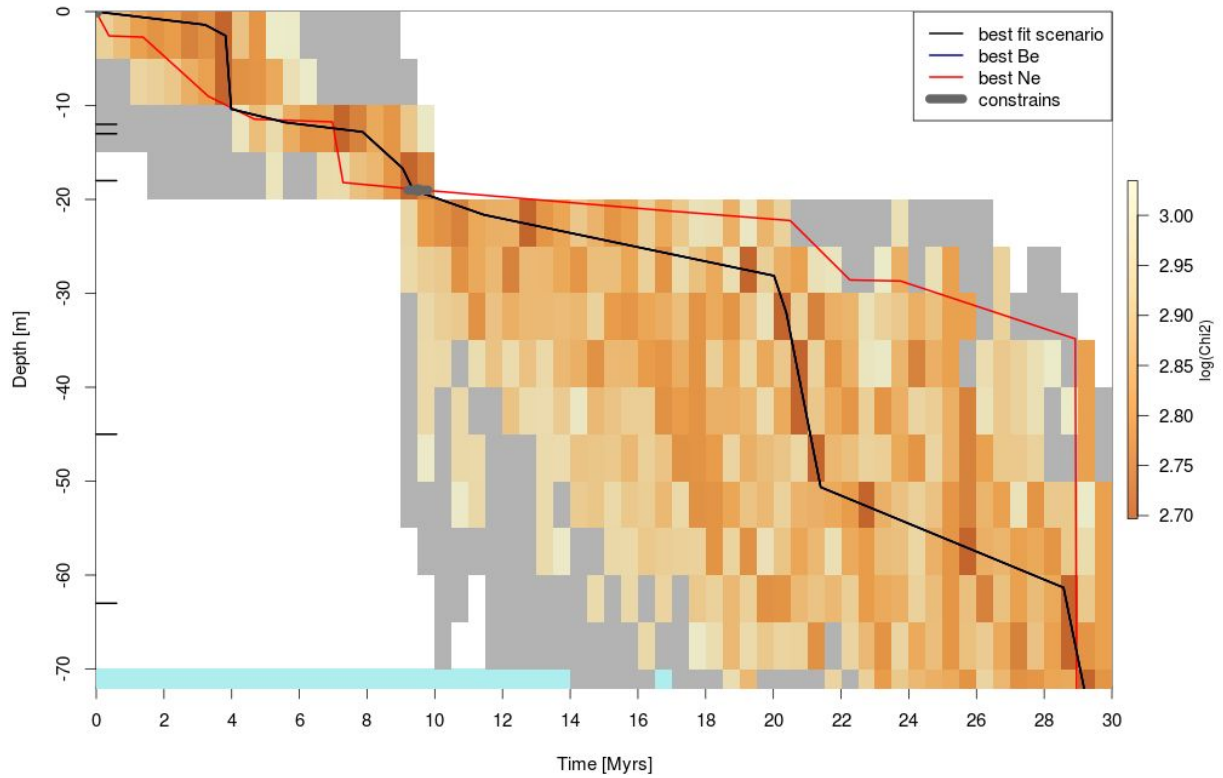


Figure A16. Age of the sediments (Ma) in function of the depth (m) in the Mirador Mine, using the BR production parameters. The black, blue and red lines correspond to the best fit scenario for both ^{10}Be and ^{21}Ne , ^{10}Be and ^{21}Ne only, respectively.

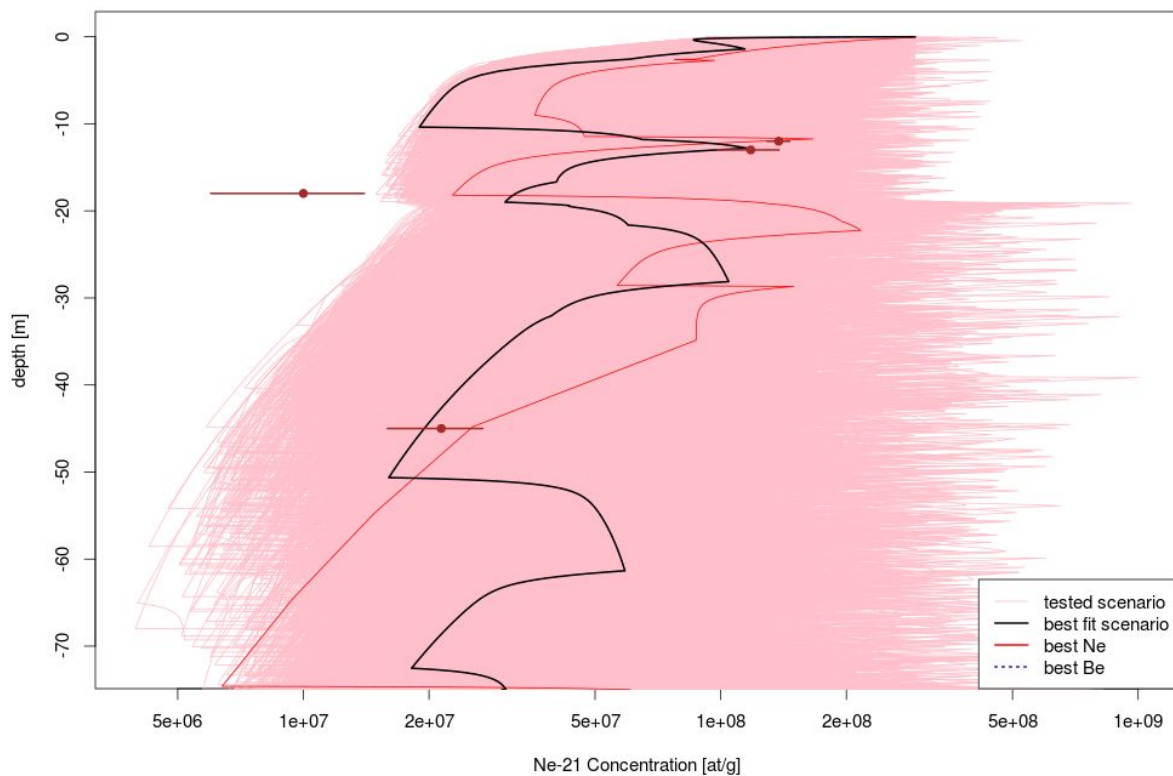
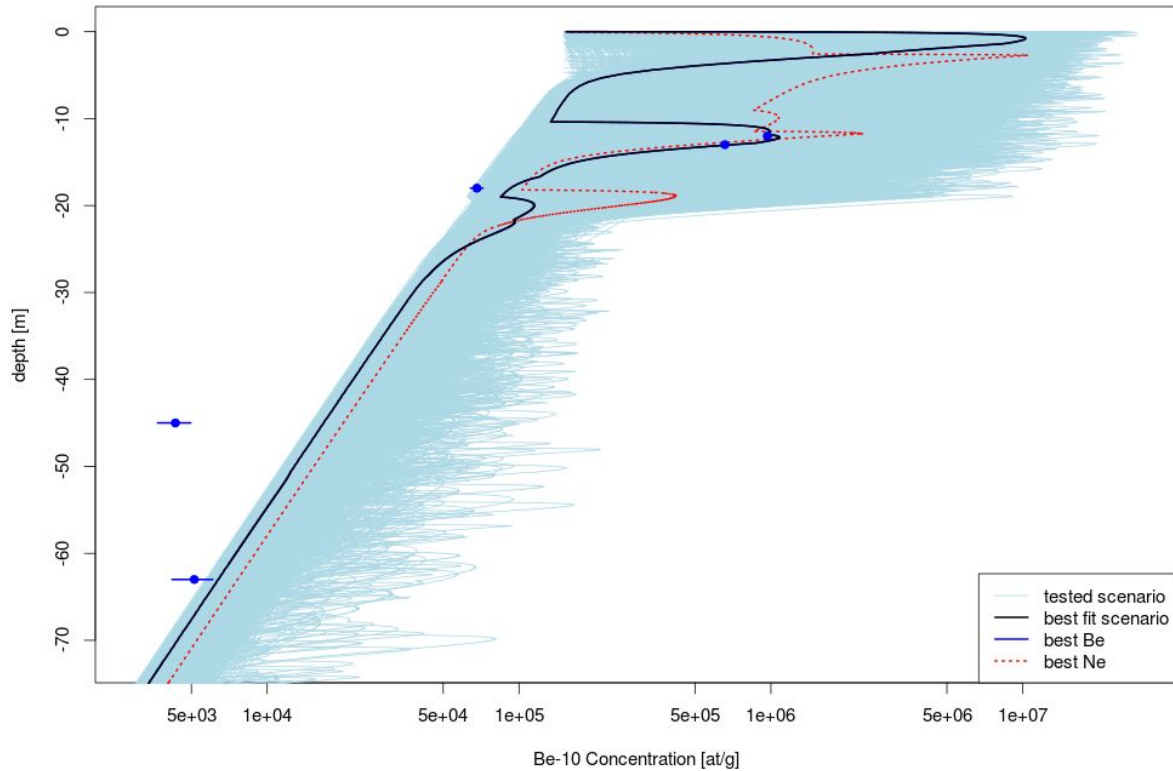


Figure A17. Cosmogenic isotope concentration (reference inversion) in the Mirador open pit using BR according to depth; the top figure shows ^{10}Be and the bottom shows ^{21}Ne . For both figures, the light colors correspond to every Monte Carlo scenario tested; the bold lines represent the best χ^2 scenario for ^{10}Be only, ^{21}Ne only and for both nuclides in blue, red and black, respectively. The circles and associated horizontal lines indicate the measured concentrations and their related uncertainties.

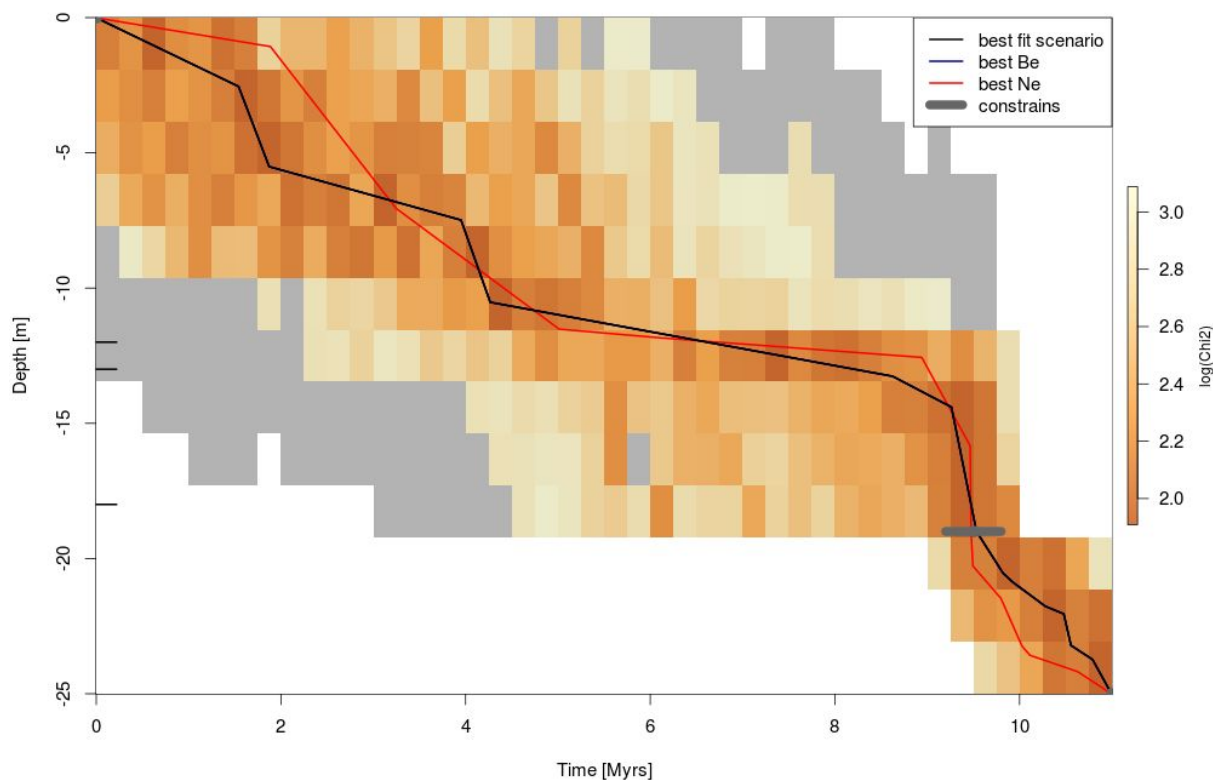


Figure A18. Model on the sediment age (Ma) in function of the depth (m) in the Mirador Mine, using the BR production parameters, and focused on the post-10 Ma period. The black, blue and red lines correspond to the best fit scenario for both ^{10}Be and ^{21}Ne , ^{10}Be and ^{21}Ne only, respectively.

6 Test inversion for Davis et al.'s data (2014)

No significant change in χ^2 is observed for inversions with various initial source erosion rates. For reference, we fixed the source erosion rate at 3 m/Ma. The inversion is based on ^{10}Be and ^{26}Al here. The various inversions processed with varying source erosion rates show that sedimentation at the bottom of the sequence began at ~ 8 Ma ago (Figure A19). The sediments appear to have been quicker around 8 Ma BP compared with the next period up to current times (Figure A20). These conclusions are similar for various source erosion rates and for various production schemes.

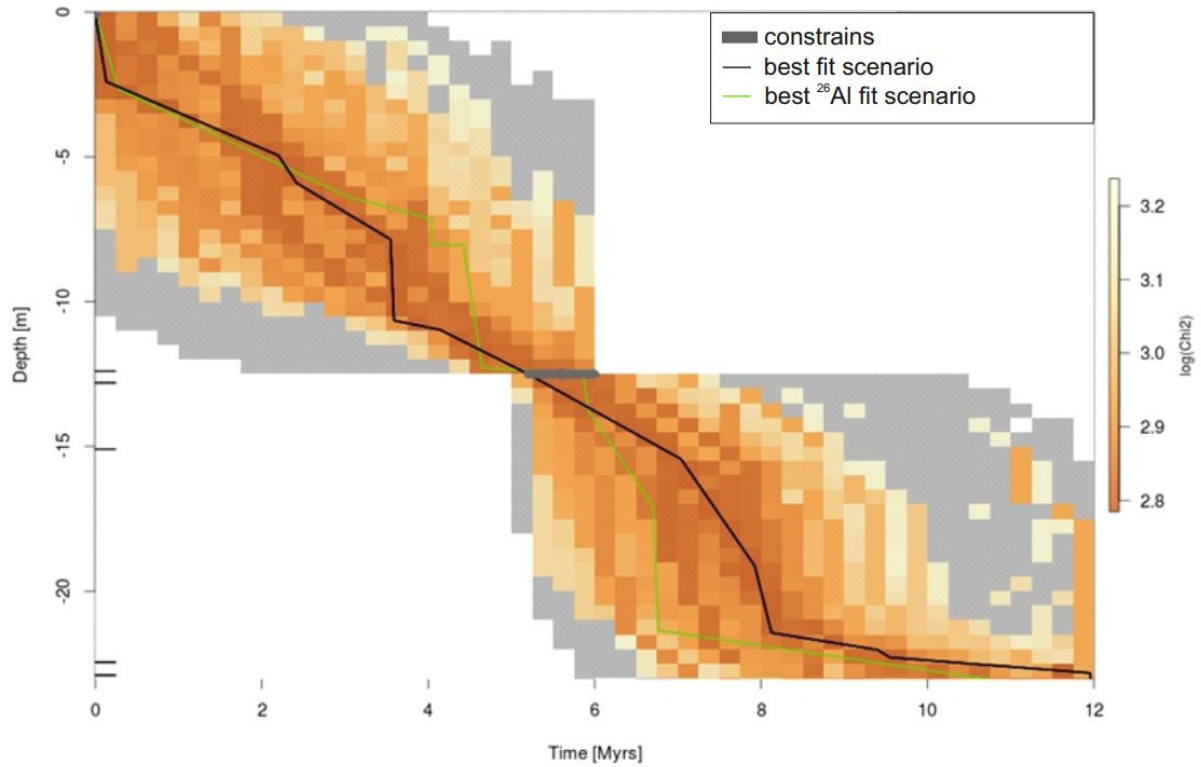


Figure A19. Age of the sediments (Ma) in function of the depth (m) in the dataset provided by Davis et al. (2014) from the Atacama Desert, using the GH production parameters. The black and green lines correspond to the best fit scenario for both ^{10}Be - ^{26}Al and ^{10}Be only, respectively.

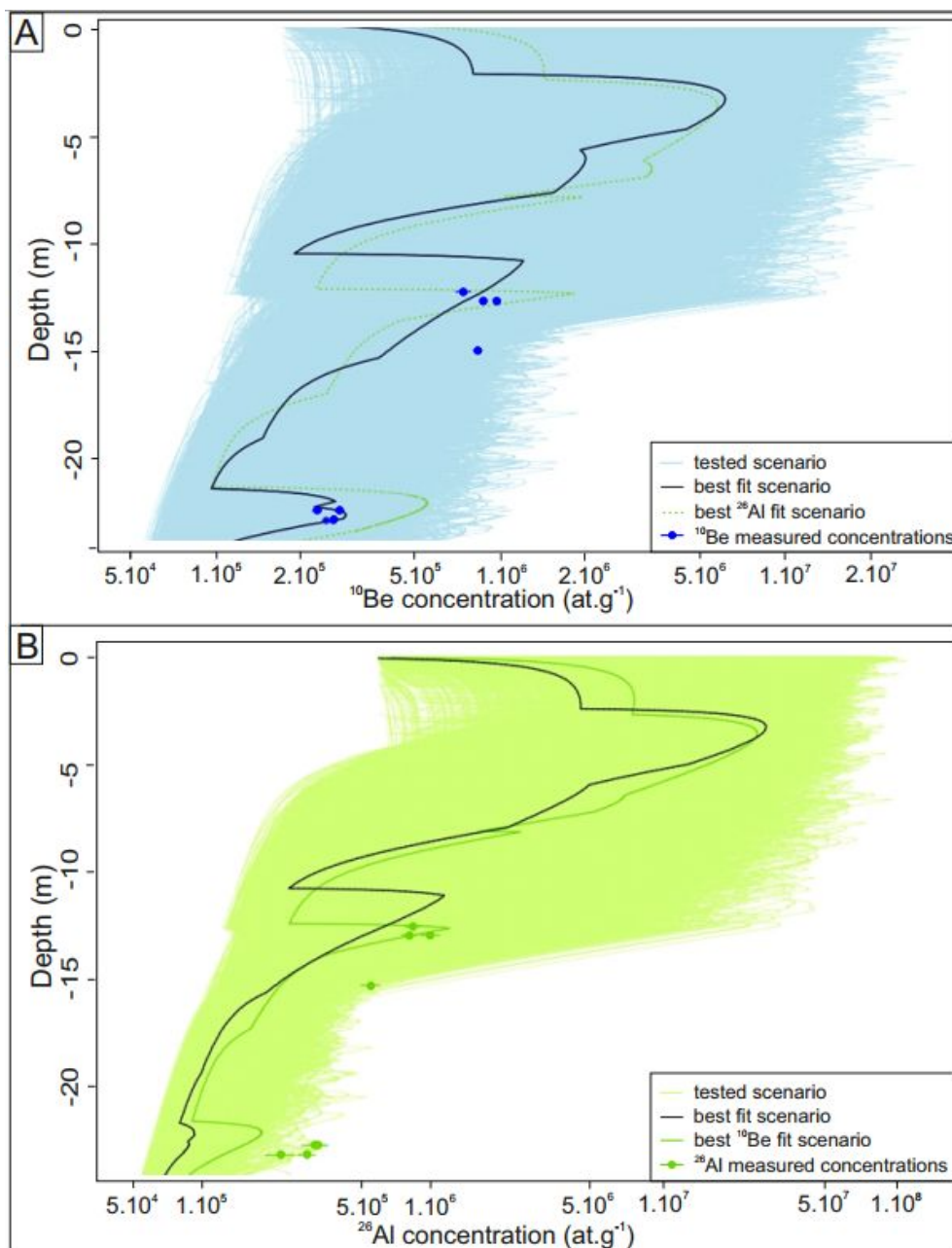


Figure A20. Cosmogenic isotope concentration (reference inversion) for the dataset provided by Davis et al. (2014) using GH parameters, according to depth; the top figure shows ^{10}Be and the bottom shows ^{26}Al . For both figures, the light colors correspond to every Monte Carlo scenario tested; the bold lines represent the best χ^2 scenario for ^{10}Be only, ^{26}Al only and for both nuclides in blue, green and black, respectively. The circles and associated horizontal lines indicate the measured concentrations and their related uncertainties.

7 References

- ARNOLD, M., MERCHEL, S., BOURLÈS, D.L., BRAUCHER, R., BENEDETTI, L., FINKEL, R.C., AUMAÎTRE, G., GOTTDANG, A. & KLEIN, M. 2010. The French accelerator mass spectrometry facility ASTER: Improved performance and developments. *Nuclear Instruments and Methods in Physics Research Section B: Beam Interactions with Materials and Atoms* **268**(11), 1954–1959.

- BALCO, G. 2017. Production rate calculations for cosmic-ray-muon-produced ^{10}Be and ^{26}Al benchmarked against geological calibration data. *Quaternary Geochronology* **39**, 150–173.
- BALCO, G. & SHUSTER, D.L. 2009. Production rate of cosmogenic ^{21}Ne in quartz estimated from ^{10}Be , ^{26}Al , and ^{21}Ne concentrations in slowly eroding Antarctic bedrock surfaces. *Earth and Planetary Science Letters* **281**(1–2), 48–58.
- BRAUCHER, R., MERCHEL, S., BORGOMANO, J. & BOURLÈS, D.L. 2011. Production of cosmogenic radionuclides at great depth: A multi element approach. *Earth and Planetary Science Letters* **309**(1–2), 1–9.
- BRAUCHER, R., GUILLOU, V., BOURLÈS, D.L., ARNOLD, M., AUMAÎTRE, G., KEDDADOUCHE, K. & NOTTOLI, E. 2015. Preparation of ASTER in-house $^{10}\text{Be}/^{9}\text{Be}$ standard solutions. *Nuclear Instruments and Methods in Physics Research Section B: Beam Interactions with Materials and Atoms* **361**, 335–340.
- BROWN, E.T., EDMOND, J.M., RAISBECK, G.M., YIOU, F., KURZ, M.D. & BROOK, E.J. 1991. Examination of surface exposure ages of Antarctic moraines using in situ produced ^{10}Be and ^{26}Al . *Geochimica et Cosmochimica Acta* **55**(8), 2269.
- CHMELEFF, J., VON BLANCKENBURG, F., KOSSERT, K. & JAKOB, D. 2010. Determination of the ^{10}Be half-life by multicollector ICP-MS and liquid scintillation counting. *Nuclear Instruments & Methods In Physics Research Section B-Beam Interactions With Materials And Atoms* **268**(2), 192–199.
- DAVIS, M., MATMON, A., PLACZEK, C.J., MCINTOSH, W., ROOD, D.H. & QUADE, J. 2014. Cosmogenic nuclides in buried sediments from the hyperarid Atacama Desert, Chile. *Quaternary Geochronology* **19**, 117–126.
- DE SILVA, S. 1989. Altiplano-Puna volcanic complex of the central Andes. *Geology* **17**(12), 1102–1106.
- DUNAI, T.J., LOPEZ, G.A.G. & JUEZ-LARRE, J. 2005. Oligocene-Miocene age of aridity in the Atacama Desert revealed by exposure dating of erosion-sensitive landforms. *Geology* **33**(4), 321–324.
- GRANGER, D.E. & MUZIKAR, P.F. 2001. Dating sediment burial with in situ-produced cosmogenic nuclides: theory, techniques, and limitations. *Earth and Planetary Science Letters* **188**(1–2), 269–281.
- HEISINGER, B., LAL, D., JULL, A.J.T., KUBIK, P., IVY-OCHS, S., KNIE, K. & NOLTE, E. 2002. Production of selected cosmogenic radionuclides by muons: 2. Capture of negative muons. *Earth and Planetary Science Letters* **200**(3–4), 357–369.
- HONDA, M., ZHANG, X., PHILLIPS, D., HAMILTON, D., DEERBERG, M. & SCHWIETERS, J.B. 2015. Redetermination of the ^{21}Ne relative abundance of the atmosphere, using a high resolution, multi-collector noble gas mass spectrometer (HELIX-MC Plus). *International Journal of Mass Spectrometry* **387**, 1–7.
- KOBER, F., ALFIMOV, V., IVY-OCHS, S., KUBIK, P.W. & WIELER, R. 2011. The cosmogenic ^{21}Ne production rate in quartz evaluated on a large set of existing ^{21}Ne – ^{10}Be data. *Earth and Planetary Science Letters* **302**(1–2), 163–171.
- KORSCHINEK, G., BERGMAIER, A., FAESTERMANN, T., GERSTMANN, U.C., KNIE, K., RUGEL, G., WALLNER, A., DILLMANN, I., DOLLINGER, G. & VON GOSTOMSKI, C.L. 2010. A new value for the half-life of ^{10}Be by Heavy-Ion Elastic Recoil Detection and liquid scintillation counting. *Nuclear Instruments and*

- Methods in Physics Research Section B: Beam Interactions with Materials and Atoms* **268(2)**, 187–191.
- MARTIN, L.C.P., BLARD, P.-H., BALCO, G., LAVÉ, J., DELUNEL, R., LIFTON, N. & LAURENT, V. 2017. The CREp program and the ICE-D production rate calibration database: A fully parameterizable and updated online tool to compute cosmic-ray exposure ages. *Quaternary Geochronology* **38**, 25–49.
- NIEDERMANN, S. 2002. Cosmic-Ray-Produced Noble Gases in Terrestrial Rocks: Dating Tools for Surface Processes. *Reviews in Mineralogy and Geochemistry* **47(1)**, 731–784.
- NISHIZUMI, K., IMAMURA, M., CAFFEE, M.W., SOUTHON, J.R., FINKEL, R.C. & MCANINCH, J. 2007. Absolute calibration of Be-10 AMS standards. *Nuclear Instruments & Methods In Physics Research Section B-Beam Interactions With Materials And Atoms* **258(2)**, 403–413.
- RIQUELME, R., TAPIA, M., CAMPOS, E., MPODOZIS, C., CARRETIER, S., GONZÁLEZ, R., MUÑOZ, S., FERNÁNDEZ-MORT, A., SANCHEZ, C. & MARQUARDT, C. 2018. Supergene and exotic Cu mineralization occur during periods of landscape stability in the Centinela Mining District, Atacama Desert. *Basin Research* **30(3)**, 395–425.
- SARTÉGOU, A., BOURLÈS, D.L., BLARD, P.-H., BRAUCHER, R., TIBARI, B., ZIMMERMANN, L., LEANNI, L., AUMAÎTRE, G. & KEDDADOUCHE, K. 2018. Deciphering landscape evolution with karstic networks: A Pyrenean case study. *Quaternary Geochronology* **43**, 12–29.
- VERMEESCH, P., BALCO, G., BLARD, P.-H., DUNAI, T.J., KOBER, F., NIEDERMANN, S., SHUSTER, D.L., STRASKY, S., STUART, F.M., WIELER, R. & ZIMMERMANN, L. 2015. Interlaboratory comparison of cosmogenic ²¹Ne in quartz. *Quaternary Geochronology* **26**, 20–28.
- ZIMMERMANN, L., BLARD, P.H., BURNARD, P., MEDYNSKI, S., PIK, R. & PUCHOL, N. 2012. A New Single Vacuum Furnace Design for Cosmogenic ³He Dating. *Geostandards and Geoanalytical Research* **36(2)**, 121–129.